LARGE STRAIN PLASTIC DEFORMATION OF TRADITIONALLY PROCESSED AND ADDITIVELY MANUFACTURED AEROSPACE METALS

Thesis

Submitted to

The School of Engineering of the

UNIVERSITY OF DAYTON

In Partial Fulfillment of the Requirements for

The Degree of

Master of Science in Mechanical Engineering

By

Luke Daniel Hoover

Dayton, Ohio

August 2021

LARGE STRAIN PLASTIC DEFORMATION OF TRADITIONALLY PROCESSED AND ADDITIVELY MANUFACTURED AEROSPACE METALS

Name: Hoover, Luke Daniel

APPROVED BY:

Robert L. Lowe, Ph.D.
Faculty Advisor and Committee Chair
Assistant Professor
Mechanical and Aerospace Engineering

Luke Sheridan, Ph.D.
Committee Member
Aerospace Research Engineer
Air Force Research Laboratory

Dennis J. Buchanan, Ph.D.
Committee Member
Division Head, Structural Materials
University of Dayton Research Institute

Jeremy D. Seidt, Ph.D.
Committee Member
Research Associate Professor
Mechanical and Aerospace Engineering
The Ohio State University

Robert J. Wilkens, Ph.D., P.E.
Associate Dean for Research and Innovation
Professor
School of Engineering

Eddy M. Rojas, Ph.D., M.A., P.E.
Dean, School of Engineering

ABSTRACT

LARGE STRAIN PLASTIC DEFORMATION OF TRADITIONALLY PROCESSED AND ADDITIVELY MANUFACTURED AEROSPACE METALS

Name: Hoover, Luke Daniel
University of Dayton

Advisor: Dr. Robert L. Lowe

To numerically simulate and predict the plastic deformation of aerospace metal alloys during extreme impact events (e.g., turbine engine blade-out and rotor-burst events, and foreign object damage), accurate experimental knowledge of the metal's hardening behavior at large strains is requisite. Tensile tests on round cylindrical specimens are frequently used for this purpose, with the metal's large-strain plasticity ultimately captured by an equivalent true stress vs. equivalent true plastic strain curve. It is now well known that if axial strain is measured using an extensometer, the equivalent true stress-strain curve calculated from this measurement is valid only up to the onset of diffuse necking. That is, once the strain field heterogeneously localizes in the specimen gage (onset of necking), extensometers, which average the strain field over the gage section, are unable to capture the local strain at the site of fracture initiation.

Thus, a number of approaches have been proposed and employed to correct the post-necking hardening response. One commonly-used technique is an iterative approach commonly referred to as finite-element model updating (FEMU). This approach involves inputting a suite of candidate post-necking equivalent true stress-strain curves into finite-element software. The true stress-strain curve that produces the best agreement between simulation and experiment is ultimately adopted. In this document, a novel variation of this iterative approach is presented, aimed at decreasing computational expense and iterative effort with a better first guess that

bounds this fan of prospective true stress-strain curves. In particular, we use local surface true (Hencky) strain data at the fracture location in an approximate analytical formula to generate a first guess curve and upper bound on the candidate true stress-strain fan of curves.

To assess its performance and robustness, the proposed approach is verified using experimental data for a menu of aerospace relevant metal alloys (In-625, In-718, Al-6061, 17-4 PH stainless steel, and Ti-6Al-4V) that span various crystallographic structures and exhibit different plastic (hardening) behaviors. For each of these metals, our approaches substantially decreases the number of candidate curves and meaningfully reduces iterative effort, a trend that holds true across a broad range of crystal structures and corresponding hardening behaviors.

Next, using the above improved iterative post-necking hardening correction, a plastic deformation model was generated for AM Ti-6Al-4V. A series of tensile experiments were completed across varying strain rates and multiple additive build orientations. The true stress-strain data from these mechanical tests help to build a database of material behavior. Parallel finite element simulations (in LS-DYNA) of the tensile experiments were completed and corrected with the novel, iterative post-necking correction method. A tabulated material card was populated with the corrected true stress-strain data from the various tensile tests, which can be widely employed to help constrain a ductile fracture model, or to qualify in-use parts and assemblies through the prediction of deformation and damage accumulation felt under a specific loading condition or impact environment.

To everyone that I've shared a run with over the years

ACKNOWLEDGEMENTS

First and foremost, I'd like to express my appreciation to my family for their continuous love, support, and guidance. Their confidence in me and my ability to achieve my goals is extremely empowering. My parents have led by example, consistently striving to better themselves. Thanks to my older sisters, Jessica and Lauren, for paving the way through our childhood and for your wise thoughts and advice. I think it says a lot about our family that all three of us have extended past our baccalaureate studies to accomplish a graduate degree.

Kathleen Colvin may be the most caring person that I have met thus far. Many thanks are owed for her continued patience and support whilst working through her own degree and athletics career. She had a front row seat to some stressful and busy times, but stayed steadfast in her love. You are truly a gem. I have so much appreciation for all that you did to keep me afloat and sane, even during the pandemic when there were many unknowns. Not to go uncelebrated, I am extremely proud of the hard work Kathleen put in on her way to becoming a registered nurse and beginning her career.

I have the faculty of the Hilliard City School District and the University of Dayton Department of Mechanical and Aerospace Engineering to thank for giving me the necessary fundamentals and opportunities required for my master's coursework and research. Specifically, working in the University of Dayton Behavior of Advanced Materials and Structures (BAMS) Lab under Dr. Robert L. Lowe has provided me with substantial opportunities and a massively meaningful experience. I greatly appreciate the support, teaching, and advice that Bob has graciously offered through over 3 years of undergraduate and graduate research advising.

This work would not be possible without the support of the Applied Mechanics Division at the University of Dayton Research Institute (UDRI). Throughout the project, Steve Fuchs has offered his and his team's time and energy to ensure that this work stayed on track to finish.

Between last-minute specimen completions, to offering imaging analyses, the Applied Mechanics Division and the Additive Manufacturing & Repair Technologies Group were a great resource.

Additionally, the team at the Air Force Research Laboratory's Turbine Engine Fatigue Facility (TEFF) has been crucial in the development of this project with their overall insight and their willingness to let me use their machines for testing. I'd like to specifically thank Dr. Onome Scott-Emuakpor, Dr. Luke Sheridan, Dino Celli, Justin Warner, and Lucas Smith for their collaboration on the experimental and theoretical mechanics employed in this work. Dino worked tirelessly through a global pandemic to assist numerous graduate assistants in completing tests towards publication and presentation. Many thanks are due for his work ethic and passion for helping others.

I certainly had wonderful examples and resources to draw from in this field. I'd like to thank Dr. Jeremy Seidt of the OSU Dynamic Mechanics of Materials Laboratory. The post-necking correction method discussed in this document was his brain-child. I am ever thankful for his contribution, which helped keep me busy with noteworthy research when research grinded to a halt during the COVID-19 pandemic. Thanks also to Jeremiah Hammer (OSU), Dr. Sean Haight (George Mason), the FAA, and the LS-DYNA Aerospace Working Group (AWG) for their work on characterizing metals towards the creation of LS-DYNA material models. Their work helped pave the way for the work completed in this project. Without their contribution to this field, I would not have been able to complete all of this work during a master's program, as their research includes much of the factor knowledge needed to be productive in this research space.

Thanks to the group at the AFRL/RX Metlab. Specifically, I would like to thank Melinda Ostendorf, Marc Doran, and Mike Velez for their help in preparing and imaging specimens. They consciously made room in their schedules to assist, and that was greatly appreciated. Additionally, the Air Force Institute of Technology (AFIT) offered help in characterizing material with their X-Ray Computed Tomography (XCT) machines and gave us a place to run some tests while our lab space was locked down due to COVID-19.

I owe a lot to Chris Negri, who has been by my side over the last 6 years as a friend, a roommate, a teammate, and a coworker. Chris is such a giver and is one of the most selfless people that I know. It has been a pleasure working through these two degrees together, and I am always grateful for the comradery during those late nights work and study sessions.

Thanks also to Brad Hripko, Kevin Lawson, and the other research assistants of the BAMS Lab. These students and peers contributed to research related conversations and offered friendship day in and day out. Thanks to my roommates and friends Garrett Grissim, Jordan Koczenasz, Sarah Richard.

Finally, I would like to extend my gratitude to coaches Jason Ordway and Rich Davis, the University of Dayton Men's and Women's Cross Country and Track and Field programs, and the entire UD athletic administration for initially bringing me to the University of Dayton, and for allowing me to pursue my passion for running as both an athlete and as a coach over the last 6 years.

VITA

Hilliard Davidson High School, Hilliard, OH …….....……...2015

B.S. Mechanical Engineering,

University of Dayton, Dayton, OH ……...…….....2019

Graduate Research Assistant,

Behavior of Advanced Materials and Structures Lab,

Department of Mechanical and Aerospace Engineering,

University of Dayton, Dayton, OH ……...2019-Present

Publications:

R.L. Lowe, **L.D. Hoover**, and C.A. Negri. 2020. Experimental Design for Negative Triaxialities: Ductile Fracture Under Combined Uniaxial Tension and Hydrostatic Pressure. In *Proceedings of the 16th International LS-DYNA Conference*. https://www.dynalook.com/conferences

B. Hripko, **L. Hoover**, P. Darsini, T. Reissman, and R. Lowe. 2019. FDM 3D-Printed Thermoplastic Elastomers: Experiments, Modeling, and Influence of Process Parameters on Properties. In *Proceedings of the ASME 2019 International Mechanical Engineering Congress and Exhibitio*n, Vol. 59377, paper ID: IMECE2019-11615, V02AT02A058.

Presentations:

L.D. Hoover, D.A. Celli, J.D. Seidt, R.L. Lowe, L. Sheridan, A. Gilat, and O. Scott-Emuakpor, “A Novel, Efficient Approach for Determining the Post-Necking True Stress-

Strain Response of Aerospace Metals," 46th AIAA Dayton-Cincinnati Aerospace Sciences Symposium, 2 Mar. 2021 (virtual conference).

L.D. Hoover, D.A. Celli, J.D. Seidt, R.L. Lowe, A. Gilat, L. Sheridan, and O. Scott-Emuakpor, "An Efficient Iterative Approach for Determining the Post-Necking True Stress-Strain Response of Aerospace Metals," ASME 2020 International Mechanical Engineering Congress & Exposition, 18 Nov. 2020 (virtual conference).

L.D. Hoover, J.T. Hammer, J.D. Seidt, R.L. Lowe, A. Gilat, L. Sheridan, and O. Scott-Emuakpor, "An Efficient Iterative Approach for Determining the Post-Necking True Stress-Strain Response of Aerospace Metals," Brother Joseph W. Stander Symposium, University of Dayton, 22 Apr. 2020 (virtual symposium). https://ecommons.udayton.edu/stander

L.D. Hoover, C.A. Negri, J.T. Hammer, J.D. Seidt, R.L. Lowe, A. Gilat, L. Sheridan, and O. Scott-Emuakpor, "An Efficient Iterative Approach for Determining the Post-Necking True Stress-Strain Response of Aerospace Metals," 45th AIAA Dayton-Cincinnati Aerospace Sciences Symposium, Dayton, Ohio, 3 Mar. 2020. ** AIAA DCASS Best Presentation Award Winner **

L.D. Hoover, C.A. Negri, J.T. Hammer, J.D. Seidt, R.L. Lowe, and A. Gilat, "An Efficient Iterative Approach for Determining the Post-Necking True Stress-Strain Response of Aerospace Metals," 15th Annual ASME Dayton Engineering Sciences Symposium, Dayton, Ohio, 29 Oct. 2019.

L. Hoover, B. Hripko, T. Reissman, and R. Lowe, “Additively Manufactured Prosthetic Fingers: Processing, Characterization, and Predictive Modeling of Ultra-Flexible 3D-Printed Materials,” Brother Joseph W. Stander Symposium, University of Dayton, Dayton, Ohio, 24 Apr. 2019.

L. Hoover, B. Hripko, R. Lowe, and T. Reissman, “Mechanical Property Characterization and Finite-Element Modeling of Ultra-Stretchable 3D-Printed Elastomers,” 14th Annual ASME Dayton Engineering Sciences Symposium, Dayton, Ohio, 30 Oct. 2018.

TABLE OF CONTENTS

LIST OF FIGURES

LIST OF TABLES

LIST OF SYMBOLS/ABBREVIATIONS/ACRONYNMS

A, B, C, n, m	Material Parameters for Johnson-Cook Model
A	Area
Al	Aluminum
AM	Additive Manufacturing
A_o	Nominal Area
ASCII	American Standard Code for Information Interchange
ASTM	American Society for Testing and Materials
BCC	Body Centered Cubic
C	Carbon
Co	Cobalt
Cu	Copper
Cr	Chromium
℃	Degrees Celsius
CAD	Computer Aided Design
CDLP	Continuous Digital Light Processing
CPU	Central Processing Unit
D_1, D_2, D_3, D_4, D_5	Damage Parameters for Johnson-Cook Damage Model
DAQ	Data Acquisition
DED	Direct Energy Deposition
DIC	Digital Image Correlation
DLP	Digital Light Processing
DOD	Domestic Object Debris
E_o, K	Material Parameter for Swift Law

$\Delta\underline{\varepsilon}^p$	Plastic Strain Increment
ε_{eng}	Engineering Strain
$\overline{E}_{true}$	Equivalent True Strain
$\overline{E}_{eng}$	Equivalent Engineering Strain
ε^p	Effective Plastic Strain
$\underline{\varepsilon}_f^p$	Plastic Failure Strain
$\dot{\varepsilon}_o$	Reference Strain Rate
$\underline{\dot{\varepsilon}}$	Strain Rate
E_{true}	True Strain
E_1	First Principal Hencky Strain Component
E_2	Second Principal Hencky Strain Component
E_3	Third Principal Hencky Strain Component
EBSD	Electron Backscatter Diffraction
F#	Focal Ratio
°F	Degrees Fahrenheit
f	Force
FAA	Federal Aviation Administration
FCC	Face Centered Cubic
FE	Finite Element
Fe	Iron
FOD	Foreign Object Debris
FEMU	Finite Element Model Updating
FLIR	Forward Looking InfraRed
GOPTEPS	Global OPTimized Equivalent Plastic Strain
GPa	Gigapascal

HCP	Hexagonal Close Packed
JC	Johnson Cook
Δl	Change in length
l_o	Original Length
LPBF	Laser Powder Bed Fusion
LVDT	Linear Variable Differential Transformer
MSE	Mean Squared Error
Mn	Manganese
Mg	Magnesium
mm	millimeter
ms	milliseconds
MTS	Materials Testing Systems
Mo	Molybdenum
MPa	Megapascal
N	Number of Data Points
N	Nitrogen
Nb	Niobium
Ni	Nickel
nm	nanometer
NMSE	Normalized Mean Squared Error
OEMs	Original Equipment Manufacturers
O	Oxygen
PH	Precipitation Hardening
PMAs	Parts Manufacturer Approvals
Ra	Roughness Average
RT	Room Temperature

σ_{eng}	Engineering Stress
$\bar{\sigma}_{true}$	Equivalent True Stress
$\underline{\sigma}$	Effective True Stress
σ^*	Stress Triaxiality
σ_{true}	True Stress
s	seconds
SEM	Scanning Electron Microscope
Si	Silicon
SLA	Stereolithography
T_o	Room Temperature
T	Temperature
Ti	Titanium
μm	Micron
UTS	Ultimate Tensile Stress
V	Vanadium
VE	Virtual Extensometer
VSG	Virtual Strain Gage
XCT	X-Ray Computed Tomography

CHAPTER I

INTRODUCTION

1.1 Background

To predict the plastic deformation of metals and alloys during extreme impact events (e.g., turbine engine blade-out and rotor-burst events, and foreign object damage), an accurate material model that correctly captures how the material responds under various loading conditions must be employed. Trustworthy material data is requisite for the creation of these effective material models. This material data is often generated through certain deformation mode-specific experiments (e.g., uniaxial tension, uniaxial compression, pure shear), which provide insight into the behavior of the material under different stress states leading up to failure, and can be broken down into two regimes. Before yield, deformation is recoverable, the relationship between the material's stress and strain remains linear [1], is easily measured, and can be predicted by the material's modulus of elasticity (ratio of the measured stress and strain) and Poisson's ratio (ratio of transverse and axial strains). After yield, plasticity begins (deformation is irrecoverable), the stress-strain behavior turns nonlinear, and strain hardening ensues, which can be characterized by a hardening exponent. The nonlinear, plastic region is more difficult to model than the linear elastic region prior to yield.

With valid coupon-level post-yield (plastic) experimental data detailing a material's response to loading, a constitutive model can be specifically calibrated for a given material and used to predict component-level inelastic deformation. An accurate material model is beneficial, as it can be used to simulate tests and experiments of in-use products, which can eliminate material waste, reduce time-intensive physical processes, and lessen required machinery and tooling for tests. Widely accepted finite element (FE) programs such as LS-DYNA [2] are used to predict the results of such tests and experiments. The material model is uploaded into the

numerical code along with other conditions matching the environment and set-up of the experiment, and then the code can predict the specific outcome of the input experimental situation.

A common plastic material model is the Johnson-Cook (JC) parameterized model [3], which is capable of capturing the deformation of materials across different strain rates and temperatures:

$$\underline{\sigma} = \left(A + B\left(\underline{\varepsilon_p}\right)^n\right)\left(1 + Cln\ \frac{\dot{\underline{\varepsilon}}}{\dot{\varepsilon_o}}\right)\left(1 - \left(\frac{T - T_r}{T_r - T_m}\right)^m\right) \tag{1}$$

where $\underline{\sigma}$ is the effective true stress, $\underline{\varepsilon_p}$ is the effective plastic strain, $\dot{\underline{\varepsilon}}$ is the strain rate, $\dot{\varepsilon_o}$ is the reference strain rate, T is the temperature of the test environment, T_r is a reference temperature, and T_m is the melting temperature of the test material. Additionally, $A, B, C, n,$ and m are material-specific parameters that constrain and fit the model for a given material and test environment. The parameters are found using an experimental test program that evaluates temperature dependence at a reference strain rate, and strain rate dependence at a reference temperature to isolate each portion of the JC model separately. The model can also predict failure of a material through its ductile fracture model:

$$\underline{\varepsilon}_f^p = \left[D_1 + D_2 e^{-D_3\sigma^*}\right]\left[1 + D_4 \ln\left(\frac{\dot{\underline{\varepsilon}}}{\dot{\varepsilon}_0}\right)\right]\left[1 + D_5\left(\frac{T - T_r}{T_m - T_r}\right)\right] \tag{2}$$

where $\underline{\varepsilon}_f^p$ is the plastic failure strain, σ^* is the stress triaxiality, and D_1, D_2, D_3, D_4, and D_5 are experimentally determined damage parameters found by varying loading condition, strain rate, and temperature respectively. Finally, the JC model tracks progressive damage in each finite element throughout its plastic deformation history via a continuum damage parameter:

$$D = \sum \frac{\Delta\underline{\varepsilon}^p}{\underline{\varepsilon}_f^p} \tag{3}$$

where $\Delta\underline{\varepsilon}^{p}$ is the equivalent plastic strain increment and $\underline{\varepsilon}_{f}^{p}$ is the stress-state-dependent equivalent plastic failure strain. When the damage parameter in an element equals 1, failure occurs and the element is eroded.

Parameterized constitutive models like JC can predict plastic deformation relatively well for certain materials under specific loadings. However, parameterized models often struggle when calibrated (tuning their material parameters) to fit a specific deformation mode, strain rate, and temperature, and are then extrapolated to model other deformation modes, strain rates, and temperatures. In Figure 1, a JC model was created for traditionally manufactured Ti-6Al-4V data at varying strain rates by fitting the model function to a reference strain rate of 1.00E-04 /s using the Global OPTimized Equivalent Plastic Strain (GOPTEPS) method [4]. The values for the tunable parameters are shown in Table 1. Because the data set does not contain tests at different temperatures, a simplified JC model was employed that does not contain the temperature term, and m was not calculated and constrained.

Table 1: Johnson-Cook Parameters For Wrought Ti-6Al-4V

A (MPa)	B (MPa)	C	n
915.77	183.73	0.1649	0.0184

*Note: Data set does not contain temperature dependence

When extrapolated to predict the behavior of other tests at different strain rates, the model struggles, as shown in Figure 1.

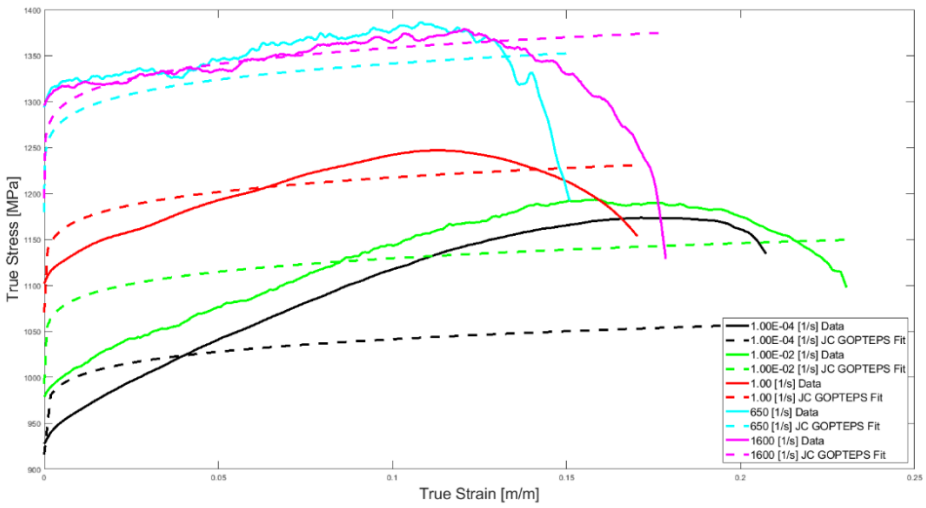

Figure 1: Ti-6Al-4V JC Plasticity Model Predictions at Varying Strain Rates

Because of this difficulty, data-driven or tabulated constitutive models have been shown to better predict material behavior across multiple strain rates, temperatures, and/or loading conditions. Examples of available tabulated LS-DYNA material models that can predict plastic deformation at varying strain rates are MAT_024, MAT_124, MAT_224, MAT_224GYS, and MAT_264. When a plastic model is needed that accounts for strain rate variance, MAT_024 is a viable option. Alternatively, MAT_124 can be used when yield asymmetry is observed in the material data. Finally, MAT_224, MAT_224GYS, and MAT264 offer an opportunity to include a failure model. Tabulated models can typically cover a larger array of test environments, load conditions, etc. than parameterized models. In tabulated plasticity models, FE codes interpolate data from a wide spectrum of experiments that are uploaded into the simulation input file. Once uploaded, the code can pull from each experiment and interpolate when specific conditions arise. Thus, rather than calibrating to one data set and extrapolating parameters, the FE software can use the plethora of test curves to solve for the material response, at a specific location, for each time step of the simulation. With the tabulated models in hand, simulations can predict the results of endless plastically deforming events.

1.2 Motivation/Applications

Correctly modeling the plastic deformation and ductile fracture of metals and alloys is a priority when attempting to predict progressive damage and eventual failure of in-use components and assemblies. Specifically, metals see significant plastic deformation leading up to fracture. Because of this, accurate large-deformation plasticity data is requisite for these types of modeling efforts. FE analysis is widely used as a tool to simulate the environment and loading conditions of materials in a substantial list of fields and applications. For instance, in metal forming processes, metal is worked until permanently deformed into a certain geometry or shape for end use ([5], [6]). Additionally, in the automotive field, crash analyses track the plastic deformation and ductile fracture of automotive metals in extreme impact events ([7], [8]). Figure 2 shows comparative results between a physical and a computational truck crash.

Figure 2: Parallel Simulation (Top) of a Physical Truck Crash (Bottom) [8]

Moreover, large-deformation data is mandatory for predicting aircraft engine failure events such as fan blade-out or rotor-burst, which create extreme impacts between jet engine components and containment casings ([9], [10]). Investigations into the high-rate impact of both foreign object debris (FOD) and domestic object debris (DOD) with the containment case or aircraft are crucial for component design and qualification. An example of a simulation-based fan blade containment study is shown below in Figure 3.

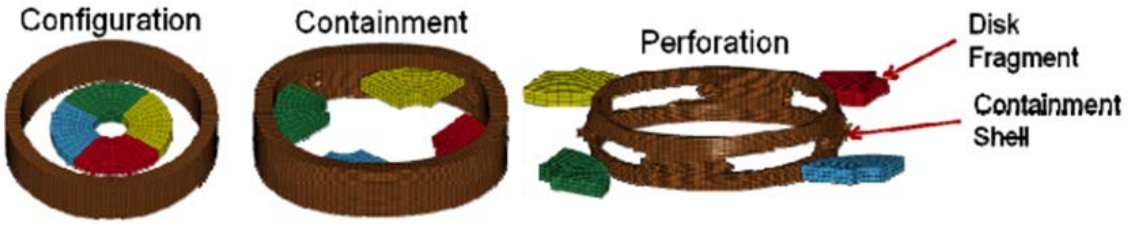

Figure 3: Fan Blade Containment Modeling and Simulation [11]

One recent example of this type of event occurred on April 27, 2018, during Southwest passenger flight 1380 [12]. A fan blade with a low-cycle fatigue crack in a CFM56-7B gas turbine engine catastrophically fractured mid-flight. Although the separated blade was contained by the fan case, the fan cowl structure failed and ejected uncontained debris that struck the wing and fuselage (Figure 4). The uncontained engine debris penetrated the aircraft, causing a depressurization of the cabin and killing one passenger. Understanding how aerospace metals plastically deform and fail in these types of high-energy impact events can provide insight into how containment structure designs can be tailored to prevent damage to the aircraft structure.

Figure 4: Damage Resulting from Southwest Flight 1380 Engine Failure [12]

In aircrafts, components are often subject to multiaxial stresses and large stress amplitudes throughout the duration of a single flight [13]. Because of this, it is of critical importance to understand how aerospace metals will behave and eventually fail. Efforts from groups like the Federal Aviation Administration (FAA) attempt to regulate aircraft design, prevent failure, and ultimately minimize the possibility of impact events from FOD and DOD. Engine parts manufacturer approvals (PMAs) are in place to certify design of parts and assemblies in the jet engine [14]. These approvals are granted based on the results of physical tests and computational predictions of tests. Certifying simply based on predictive simulations would reduce material waste, manufacturing time, and cost of physical testing. Thus, the accurate prediction of these impact events serves as a safeguard against engine failure and unwanted flight risk that could save both aircrafts and lives. With a working, accurate plastic deformation model for aerospace metals, original equipment manufacturers (OEMs) and other aircraft manufacturers are one step closer to certifying parts and assemblies through numerical simulations.

1.3 Literature Review

1.3.1 Additive Manufacturing

Additive manufacturing (AM), or 3D printing, continues to emerge as a functional and effective manufacturing process. It contrasts with subtractive manufacturing, where material is gradually removed until only the final geometry remains. Rather, the additive process incrementally "builds" thin layers of material from the ground up using a computer model of the geometry. Only the material required for the finished part (plus any needed supports) is deposited, which minimizes material waste typical of subtractive manufacturing methods. Additionally, additive methods can often complete finely detailed products to close tolerance, which cuts out the need for various post-build machining processes and the requisite tooling. Because of these and other advantages, additive manufacturing is attracting significant interest for end-use parts in various fields such as automotive, biomedical, and aerospace [15].

Various types of additive processes create components for a specific class or classes of materials (polymers, ceramics, and/or metals). To name a few, there are laser-based, extrusion, material jetting, adhesive, and electron beam processes. These technologies all fall under the umbrella of rapid prototyping and combine to create a rapidly growing market, which cleared $5 billion in 2015 [16]. The number of rapid prototyping systems sold between 1995 and 2010 are shown in Figure 5 below.

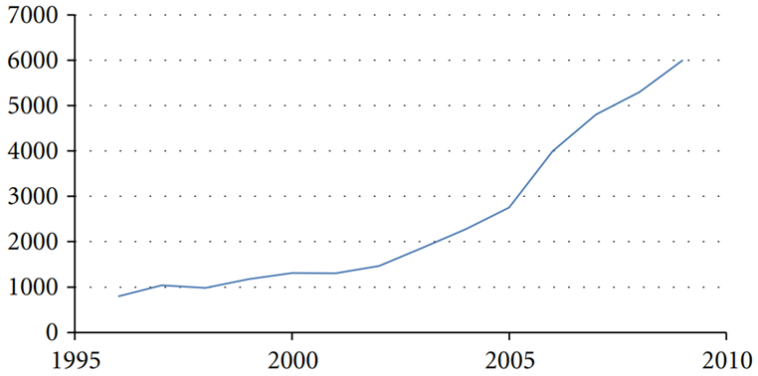

Figure 5: Growth of Rapid Prototyping [17]

Vat polymerization (one example of a laser-based process) uses ultraviolet light to cure a part layer-by-layer inside a vat of photo-curable resin. Using a computer model of the geometry, mirrors deflect a flashing light with a 2D planar image of the component at each vertical step. Specific types of machines, such as stereolithography (SLA), digital light processing (DLP), and continuous digital light processing (CDLP), are often desktop systems, and the resulting geometries often make good prototypes or scaled models, as they can be produced in a very short time. Fused deposition modeling (FDM), or material extrusion, pulls plastic filament material through a heated nozzle. Each layer solidifies after it is deposited, bonding to adjacent layers and ultimately creating a solid finished part. Other popular machines use similar technology to build parts out of plastics, polymers, and occasionally ceramics. Material jetting, similar to a household inkjet printer, lays drops of molten material that ultimately solidify into a finished part. Alternatively, binder jetting inserts a liquid inside of a gelatinous support structure. This process allows complex and fragile parts to be build.

Different from the common plastic/polymer material additive methods, metal additive manufacturing requires a different type of process. In this case, a directed heat source (laser, electron beam, etc.) melts very fine powdered metal or wire feed. As each molten layer of metal continues to cool, a finished part is built in a vertical manner. Two of the main types of metal

additive manufacturing are laser powder bed fusion (LPBF) and direct energy deposition (DED). In the former, a bed of powder is recoated after each layer of sintering. In these machines, the laser targets specific locations of the powder bed to melt into a formed product. With DED machines, powder or wire feedstock is fed through the heat source. The resulting molten metal is deposited onto the previous layer, cools, and solidifies. This process repeats until the target geometry is achieved.

1.3.2 Laser Powder Bed Fusion of Metals

The LBPF process, illustrated in Figure 6, involves locally melting and solidifying metal powder in small vertical layers to form a three-dimensional geometry. Common metals used in LPBF AM are Ti-6Al-4V, 316L stainless steel, 17-4 PH stainless steel, 18Ni300 maraging steel, AlSi10Mg, cobalt-chrome-molybdenum alloys, Inconel 625, and Inconel 718 [18]. These alloys are used across a wide array of fields and applications including, but not limited to, medical, automotive, aerospace, power, and marine products.

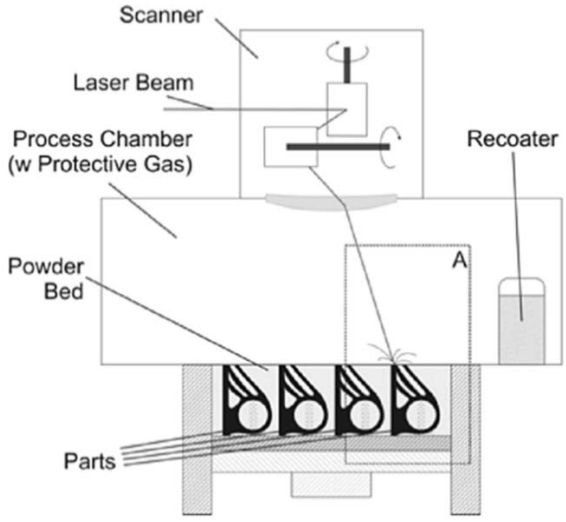

Figure 6: Schematic Illustrating the Laser Powder Bed Fusion AM Process [19]

Additionally, AM metals have different microstructures and material properties depending on the build parameters used in the additive manufacturing process. In LPBF, scan speed, spot diameter, recoat time, step size, hatch size, and laser power are all chosen appropriately to optimize the resultant components [18]. In addition to different microstructures, LPBF metal AM can introduce porosity and keyholing (Figure 7) as well as residual stresses, dependent on the build geometry and the parameters used in the build process. Pores are thought to appear when there is an abundance of powder denudation around the melt pool and large amounts of surface roughness across layers [20]. Various studies ([21], [22], [23]) aim to find best practices, and process parameters that decrease porosity and surface defects and optimize material properties.

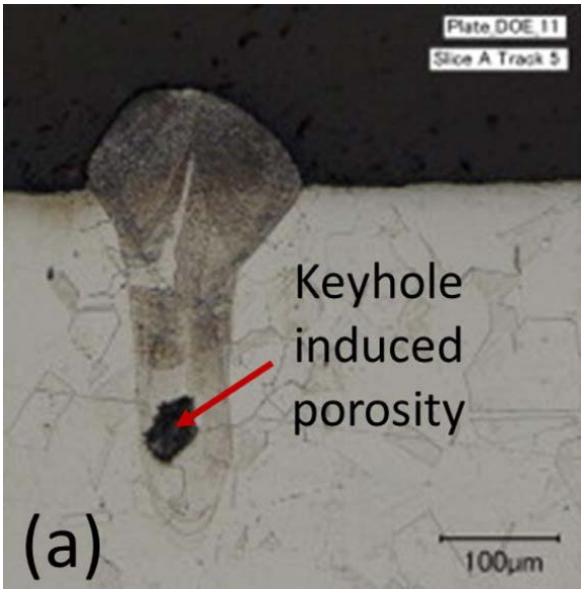

Figure 7: Keyhole Porosity in 316L Stainless Steel [24]

1.3.3 Plastic Deformation of AM Ti-6Al-4V: Experiments and Modeling

Ti-6Al-4V is a commonly used titanium alloy and a favored material due to its high strength-to-density ratio and its ability to withstand high-temperature environments. Work is

currently being completed to better understand both how additively manufactured Ti-6Al-4V microstructure and material properties change depending on the build parameters, and how AM Ti-6Al-4V behaves across varying loading conditions (stress state, strain rate, and temperature). With its use across noteworthy applications like the medical field, automotive manufacturing, aerospace innovation, marine, etc., an understanding of how the material behaves under small and large deformations is a priority for its effective implementation.

The manufacturing of AM Ti-6Al-4V through powder bed fusion is governed by American Society for Testing Materials (ASTM) Standard F2924 [25]. Beese et al. [26] and Vilaro et al. [27] both detail the build strategy evaluated in their AM Ti-6Al-4V test series. Because each build parameter set yields a slightly different material/microstructure, it is imperative to carefully and thoroughly record build details to ensure repeatability. To name a few, values such as laser power, scan velocity, layer height, and spot size can all influence the resulting material's microstructure and material properties.

At room temperature, Ti-6Al-4V exists as a single-phase (alpha) solid with a hexagonal close-packed (HCP) crystal structure [28]. At elevated temperatures (reached during LPBF AM), Ti-6Al-4V undergoes a phase transformation from a hexagonal close-packed alpha phase to a body-centered cubic (BCC) beta phase [29]. When cooling, the resultant material reflects a mixed alpha-beta grain structure [29], as shown in the representative micrograph (Figure 8).

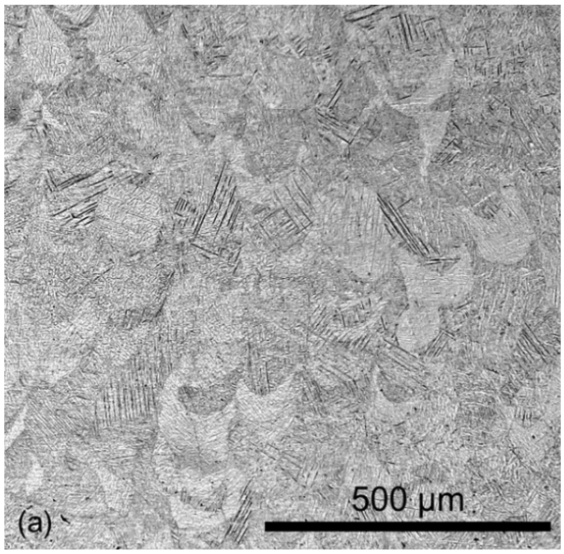

Figure 8: Alpha-Beta Grain Structure in AM Ti-6Al-4V [30]

As shown in Figure 8 and discussed in Ref. [26], LPBF AM Ti-6Al-4V displays a basket-weave microstructure of alpha laths inside of the columnar beta grain structure, which grow vertically through each layer.

Because LPBF AM Ti-6Al-4V differs from traditionally processed Ti-6Al-4V, new models must be created to capture and predict its novel mechanical behavior. To properly characterize this behavior, mechanical test data across varying loading conditions (stress states, strain rates, and temperatures) is requisite. In addition to the build parameters, anisotropy can play a significant role in shaping the material properties. Because of the columnar beta grains aligned with the (vertical) build direction, material properties are different among three orthogonal directions [30]. For instance, Figure 9 documents how the material properties of LPBF TI-6Al-4V can vary based on build direction (longitudinal direction vs. transverse direction).

	As-Fabricated			
	LD	TD	As Cast	Wrought
σ_u (MPa)	1206 ± 8	1166 ± 25	980	995
$\sigma_{0.2\ \text{pct}}$ (MPa)	1137 ± 20	962 ± 47	865	930
ε (pct)	7.6 ± 2	1.7 ± 0.3	13.5	14
E (GPa)	105 ± 5	102 ± 7	/	/

Figure 9: Anisotropic Material Properties of LPBF Ti-6Al-4V [27]

The authors in Ref. [30] detail their plastic modeling efforts for LPBF Ti-6Al-4V, which employs a Hill 1948 anisotropic yield criterion, associated flow rule, and an isotropic hardening law in their attempt to capture the behavior of the material. Further, Gorji et al. [29] have worked to create a plasticity model by assigning various hardening curves to each grain depending on its characteristics. Their experiments on singular beta grains show variation in stress and fracture strain arguing for grain-specific modeling.

1.4 Research Opportunities and Thesis Goals/Scope

As discussed in Section 1.3, there is a need for trustworthy experimental data that characterizes the large-strain plasticity of aerospace metals – specifically LPBF AM Ti-6Al-4V – across varying stress states, strain rates, temperatures, and build orientations. This data can provide insight on how these metals plastically deform and undergo ductile fracture, as well as inform predictive computational models that aim to qualify load-bearing AM parts and structures. Toward this end, an experimental program is performed in Chapter 3 of this thesis that quantifies the plastic deformation of LPBF AM Ti-6Al-4V over a range of strain rates and build orientations not yet investigated in the literature. The significance of strain rate and build orientation on mechanical properties and post-yield hardening behavior are assessed. Equivalent true stress-strain hardening behavior for LPBF AM Ti-6Al-4V is determined using an efficient, novel post-necking correction method developed and validated in Chapter 2 of this thesis. The resulting

coupon-level mechanical test data for LPBF AM Ti-6Al-4V can be used by the automotive, aerospace, and/or AM community to calibrate tabulated or parameterized constitutive models for use in predictive computational models of component/structural-level inelastic deformation.

CHAPTER II

A NOVEL AND EFFICIENT POST-NECKING CORRECTION METHOD

2.1 Background

2.1.1 Motivation

To properly understand how aerospace metals behave when subjected to large plastic deformations (e.g., during high-energy impacts such as gas turbine engine blade-off or rotor-burst events), mechanical characterization at large strains is mandatory. Of specific interest is the true stress-strain (or, more precisely, equivalent true stress-strain) response, which is used to calibrate large-strain elasto-plastic constitutive models for use in finite element analyses.

Tensile testing is just one of the many experiments used to capture stress-strain data describing a metal's mechanical response under loading. Tensile testing involves a characteristic geometry – typically a thin, flat (rectangular) or axisymmetric (round) specimen with a reduced (gage) section – that is gripped on its shoulder tabs or shanks (wide sections) and pulled apart uniaxially along its length. Loading the tensile specimen in only one direction creates a nearly one-dimensional (uniaxial) state of stress in the gage section prior to necking. Measuring the amount of force needed to pull the metal to fracture helps quantify its resistance to elastic deformation (Young's modulus), the onset of plastic deformation (yield strength), and its load-bearing capacity (ultimate strength).

Various instruments and tools – including strain gages, extensometers, and, more recently, digital image correlation – have been used to measure strain, or the local change in geometry, experienced in the specimen gage at the site of fracture initiation during tensile testing. Extensometers measure the length change Δl during testing between two points in the gage section initially separated by a distance l_0. The instantaneous length change Δl is normalized by the characteristic length l_0 to provide the axial engineering strain $\varepsilon_{eng} = \Delta l / l_0$. Implicit in this length-averaged measurement of engineering strain is that the deformation in the gage section

(and, specifically, within the extensometer window) is homogeneous, which is only true prior to strain localization and necking. Strain gages, on the other hand, provide a local measurement of engineering strain. However, since strain gages are placed on the physical specimen prior to testing, it is unlikely that this placement will coincide with the fracture location.

In recent years, optical measurement methods such as stereo digital image correlation (DIC) have been developed. This technique uses two cameras to capture the motion of a randomly applied, high-contrast speckle pattern applied to the specimen gage. Specialized software is then used to correlate the camera images and generate a full-field contour map of the surface strains. Virtual extensometers and virtual strain gages are placed using the DIC software, similar to placing the physical measurement tools on the specimen. However, whereas physical extensometers and strain gages must be placed prior to testing, DIC virtual extensometers and strain gages are placed after the test takes place, using the frame-by-frame images as a guide to identify the fracture location.

During tensile testing of a metal, the strain field in the gage section evolves from a nearly homogeneous profile prior to necking to a heterogeneous profile after the onset of necking. During necking, the strain field localizes about the eventual fracture point, accompanied by a significant reduction in cross-sectional area. After necking, the length-averaged extensometer measurement is no longer reflective of the local state of strain at the fracture location. Further, the customary analytical relationships used to convert between engineering stress/strain and true stress/strain in uniaxial tension,

$$\sigma_{true} = \sigma_{eng}\left(1 + \varepsilon_{eng}\right), \qquad E_{true} = \ln\left(1 + \varepsilon_{eng}\right)$$

break down after necking, when the state of stress is no longer homogeneous and uniaxial. Transverse stress components are no longer insignificant, and their magnitudes vary from the center of the specimen (where they are maximum) to the traction-free lateral boundary (where they vanish). This issue is somewhat mitigated with the use of a DIC strain gage, which can capture the true strain at the fracture point throughout the deformation history. However, the true

stress after necking is still unknown. Therefore, post-necking correction methods have been developed to deduce the full true stress-strain response.

2.1.2 Post-Necking Methods Literature Review

Numerous methods have been developed to correct post-necking equivalent true stress-strain data obtained from tensile tests of metals. Perhaps the oldest technique, Bridgeman's correction [31], uses the change in necking curvature radius to adjust the stress throughout the post-necking regime. More recent Bridgman-type correction methods use similar approaches ([32], [33]). A key difficulty with the Bridgman correction is accurately measuring the change in necking curvature radius during testing. Imaging the small portion of the specimen gage undergoing necking during a sometimes very short tensile test can be challenging. Additionally, the method requires a certain level of computational complexity to calculate the adjusted stress values.

Like Bridgman's method, the virtual fields method ([34],[35]) can generate a post-necking correction result without the need for finite element analysis. This can drastically cut down on the amount of time needed to obtain the correct post-necking stress-strain curve. Different from Bridgman's method, the virtual fields method uses imaging to view deformation even on non-standard stress states. [35]. An update at each time increment ensures the stress remains on the yield surface. A pitfall to this method is the amount of mathematics and computation needed to set it up. A balance is needed between time consumption, complexity, and accuracy when using a post-necking correction method.

Perhaps the most popular method among OEMs is an iterative approach employing finite element analysis in an experimental-numerical iterative approach ([39], [40], [41]). In this approach ([36], [37]), various post-necking curves are created for tensile test simulations, where parameters are optimized, or error between the simulation and test is minimized, through the use of an objective function. Each simulation is checked against the original test. Upon matching, the

respective post-necking input curve represents the actual material behavior from the test. This, however, can be computationally expensive.

2.1.3 Novel Research Contribution

In this chapter, a novel and efficient post-necking correction method is proposed and benchmarked. Using the equivalent true strain history obtained from a DIC virtual strain gage placed at the tensile specimen fracture location, an approximate first-order analytical approach is suggested for calculating the corresponding equivalent true stress. The utility and robustness of this novel and straightforward true stress calculation is demonstrated in two contexts. First, it is integrated into an iterative finite element model updating (FEMU) scheme, where our calculated equivalent true stress-strain curve is employed as an upper bound and first guess in the iterative updating scheme. This upper bound constrains the "fan" of prospective post-necking true stress-strain curves (with varying strain hardening exponents using an assumed Swift hardening law [38]). This constrained "fan" coupled with an improved first guess lead to fewer overall simulations to achieve acceptable convergence between simulation and experiment. Second, our new true stress calculation is used to generate a simple post-necking hardening law, using linear interpolation between known true stress-strain states at necking and fracture. Both approaches are benchmarked using experimental data from a suite of metals with different crystal structures and hardening behavior: Inconel 625, Inconel 718, 17-4 precipitation hardening (PH) stainless steel, and Ti-6Al-4V titanium alloy.

2.2 Experiments

2.2.1 Materials and Specimen Preparation

To evaluate the effectiveness of the proposed post-necking correction method, a set of aerospace-relevant metals with different crystal structures and hardening behavior were tested:

Inconel 625, Inconel 718, 17-4 PH stainless steel, and Ti-6Al-4V titanium alloy. Available vendor-reported chemical compositions are reported in Table 2 and Table 3.

Table 2: Vendor-reported chemical composition of 0.5-inch-diameter Inconel 718 bar (in wt. %)

Ni	Fe	Cr	Nb	Mo	Ti	Al	Co	Mn	Si	Cu	C	Mg
52.59	18.60	18.41	5.15	2.87	0.91	0.57	0.43	0.09	0.08	0.05	0.04	0.01

Table 3: Vendor-reported chemical composition of 0.5-inch-diameter Ti-6Al-4V bar (in wt. %)

Ti	Al	V	Fe	O	C	N
89.12	6.40	4.05	0.19	0.18	0.03	0.03

All as-received stock was in the form of 0.5-inch-diameter round bar. Prior to receipt, the Inconel 718 bar was rolled, solution annealed at 1751 °F for one hour, then quenched in water. Subsequent heat treatment involved artificially aging at 1325 °F for eight hours, 1150 °F for ten hours, and then quenching in nitrogen. The 17-4 PH bar was rolled, solution annealed at 1900 °F for one hour, then rapidly cooled. Subsequent heat treatment involved artificially aging at 900 °F for one hour, then air cooling. The Ti-6Al-4V bar was rolled, heated to 1300 °F for two hours, then air cooled.

ASTM E606 [42] axisymmetric cylindrical tensile specimens (Figure 10) were machined on a lathe from the 0.5-inch-diameter round bar stock.

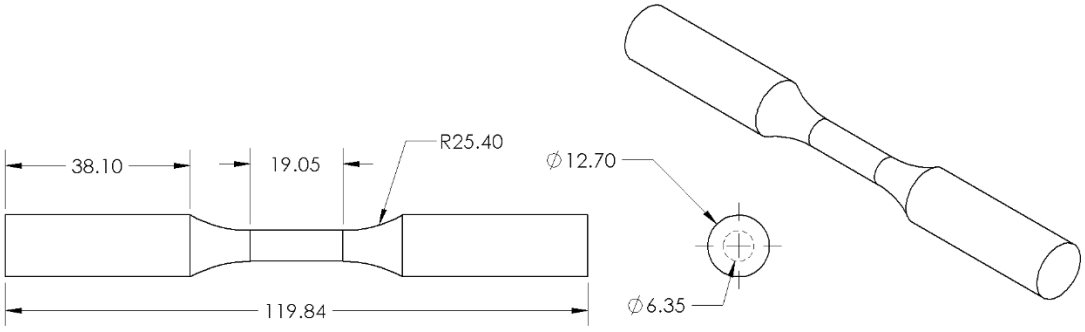

Figure 10: Nominal Post-Necking Correction (ASTM E606) Specimen

After machining, a low-stress grind was performed to relieve residual stresses imparted by machining. Each specimen's surface was polished with a handheld polisher and molybdenum disulfide lubricant (MOYKOTE, DuPont, Wilmington, DE). A target surface roughness of 8 roughness average (Ra) was confirmed with a portable profilometer. Each specimen's gage dimensions were then measured using a non-contact optical 3D measurement system (VR-3000, KEYENCE, Itasca, IL). Prior to optical measurement, the specimen gage sections were lightly sprayed with non-aqueous wet developer aerosol (SKD-S2, Magnaflux, Glenview, IL) to reduce the effects of polished metal reflecting light, leading to an unwanted reduction in scanning accuracy. It is imperative that the modeled specimen have the same gage dimensions as its respective as-machined physical specimen for each simulation to match its respective physical tensile test.

All specimens were cleaned with acetone and/or isopropyl alcohol to remove dirt, dust, and other debris. In preparation for digital image correlation (DIC), a high-contrast speckle pattern was applied to each test specimen using an airbrush. White paint was uniformly applied to completely cover the specimen's gage section. After, but before drying, black paint was sprayed from farther back to apply a speckle on top of the white background. All specimens were tested

within a few hours of speckling to avoid paint cracking. Additionally, care was taken during mechanical testing to avoid scratching or rubbing off the paint.

2.2.2 Mechanical Test Setup

Quasi-static tensile testing was performed using a custom-built Materials Test Systems (MTS) 858 tabletop servo-hydraulic load frame. All tests were conducted under displacement control with a constant actuator speed of 1E-03 in/s, which translates to a nominal strain rate of 1.33 E-03 1/s. Two MTS 647 hydraulic wedge grips were used to secure about three-quarters of each specimen's shoulder tabs. During testing, an MTS load cell measured the force, which was recorded using an MTS FlexTest60 Controller. A clip-on extensometer with an initial separation of 0.577 inch. (14.6558 mm) was placed about the center of the specimen to verify the DIC-based strain measurement. Five specimens of each metal were tested. A picture of a representative gripped, speckled specimen and clip-on extensometer is shown in Figure 11.

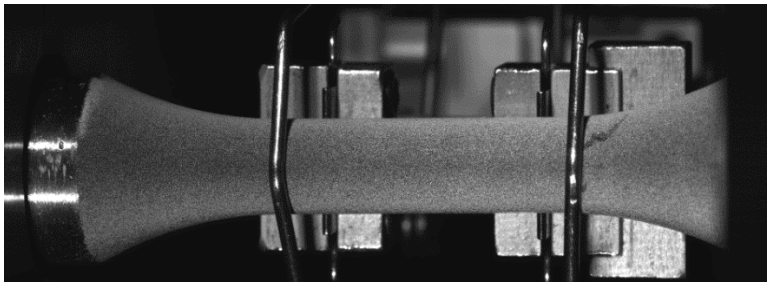

Figure 11: Representative Mechanical Test Setup

2.2.3 Digital Image Correlation Setup

Because our method relies on true strain data at the fracture location throughout the specimen's plastic deformation history, digital image correlation (DIC) was employed for strain measurement. A high-contrast speckle pattern was applied to all specimens (Sec. 2.2.1). A stereo camera setup with two high-performance monochrome cameras (FLIR Grasshopper 3 GS3-U3-

89S6M-C, 4096 x 2160 resolution) with Schneider XNP Xenoplan compact 50-mm lenses were leveraged to capture sequential images of the motion of the speckle pattern. DIC data was recorded using acquisition software (VicSnap, Correlated Solutions, Irmo, SC) and synchronized with the MTS FlexTest60 force signal. Three-dimensional digital image correlation software (VIC-3D v.7, Correlated Solutions, Irmo, SC) was used to compute the deformation and strain in the gage section from the series of time-stamped images.

A Gaussian low-pass logarithmic filter was applied to the data when correlating, which averages the strain values at each pixel to reduce noise and present a clear and uniform strain measurement. Data was captured at a frame rate of 200 ms with an F# of 8.3. A virtual extensometer (VE) and virtual strain gage (VSG) were placed on the specimen to calculate the strain in the area of interest (Figure 12).

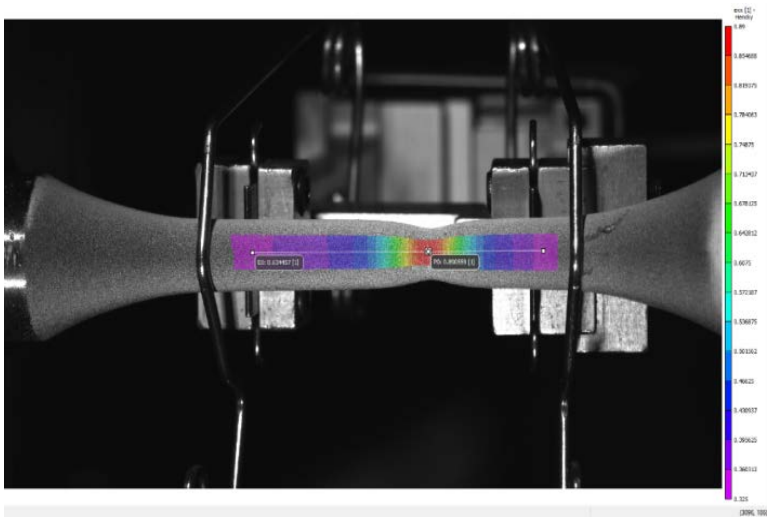

Figure 12: DIC Virtual Extensometer and Virtual Strain Gage

The virtual extensometer was placed coinciding with the 0.577 inch (14.6558 mm) physical extensometer. The virtual strain gage was placed as a 14x14 pixel square region as close as possible to the eventual fracture location. Detailed information on the DIC parameters used in each test can be found in Table 4.

Table 4: Digital Image Correlation Details

Test #	Subset	Step	Filter Size	Pixel/mm	VSG Size (pixels)	VSG Size (mm)	VE Length (mm)
In625 Test 1	41	10	7	0.015625	14	0.21875	14.6558
In625 Test 2	39	9	7	0.015625	14	0.21875	14.6558
In625 Test 3	43	10	7	0.015625	14	0.21875	14.6558
In625 Test 4	41	10	7	0.015625	14	0.21875	14.6558
In625 Test 5			7		14		14.6558
In718 Test 1	39	9	7		14		14.6558
In718 Test 2	39	9	7		14		14.6558
In718 Test 3	41	10	7		14		14.6558
In718 Test 4	41	10	7		14		14.6558
In718 Test 5	39	9	7		14		14.6558
Ti64 Test 1	37	9	7		14		14.6558
Ti64 Test 2	35	8	7		14		14.6558
Ti64 Test 3	33	8	7		14		14.6558
Ti64 Test 4	37	9	7		14		14.6558
Ti64 Test 5	35	8	7		14		14.6558
SS 17-4 PH Test 1	37	9	7		14		14.6558
SS 17-4 PH Test 2	37	9	7		14		14.6558
SS 17-4 PH Test 3	37	9	7		14		14.6558
SS 17-4 PH Test 4	37	9	7		14		14.6558
SS 17-4 PH Test 5	35	8	7		14		14.6558

2.3 Post-Necking Correction Methodology

2.3.1 Novel Approach for Calculating Post-Necking True Stress

This method leverages the DIC virtual strain gage (Sec. 2.2.3), which provides an accurate record of the Hencky (logarithmic or true) strain at the specimen fracture location throughout its deformation history. Specifically, from the virtual strain gage, the maximum (longitudinal) and minimum (transverse) principal Hencky surface strains, E_1 and E_2, are obtained. The usual assumption of isochoric (volume-preserving) plastic deformations and small elastic strains imposes the constraint that the trace of the Hencky strain tensor vanishes, so that the third principal Hencky strain, E_3, can be found:

$$E_3 = -(E_1 + E_2) \tag{4}$$

With all three DIC principal Hencky strain histories at the fracture location in hand, the equivalent true plastic strain, $\bar{E}_{true}$, can be determined as follows:

$$\bar{E}_{true} = \sqrt{\frac{2}{3}(E_1^2 + E_2^2 + E_3^2)} \tag{5}$$

To find the equivalent true stress, an approximate first-order analytical approach is employed. Inspired by the customary relationships used to convert between the axial components of engineering stress/strain and true stress/strain in uniaxial tension prior to necking,

$$\sigma_{true} = \sigma_{eng}\big(1 + E_{eng}\big), \qquad E_{true} = \ln\big(1 + E_{eng}\big), \tag{6}$$

an analogous version of Eq. $(6)_2$, generalized to equivalent strains, is used to convert the post-necking DIC equivalent true strain $\bar{E}_{true}$ to an equivalent engineering strain $\bar{E}_{eng}$:

$$\bar{E}_{eng} = e^{\bar{E}_{true}} - 1 \tag{7}$$

The equivalent true stress, $\bar{\sigma}_{true}$, is obtained by through a generalization of Eq. (6) to equivalent stress and strain measures:

$$\bar{\sigma}_{true} = \sigma_{eng}(1 + \bar{E}_{eng}) \tag{8}$$

Note that $\sigma_{eng} = f/A_0$ is not an equivalent stress measure, but rather the axial component of the engineering stress, with f the axial force recorded by the load cell and A_0 the cross-sectional area of the gage of the undeformed specimen. Equations (5) and (8) together provide an approximate post-necking equivalent true stress-strain ($\bar{\sigma}_{true}$ vs. $\bar{E}_{true}$) curve, with Eq. (5) generated directly from experimental data and Eq. (8) derived using a first-order analytical approach.

2.3.2 Identifying the Onset of Necking

Three independent methods [43] are used to identify the onset of necking in the tensile test data for Inconel 625, Inconel 718, 17-4 PH stainless steel, and Ti-6Al-4V titanium alloy:

1. Identify the maximum of the engineering stress-strain curve (engineering strain measured by DIC virtual extensometer).
2. Identify deviation between true stress-strain curves obtained via (a) the DIC virtual extensometer (true stress calculated using Eq. (6)) and (b) the DIC virtual strain gage (true stress calculated using Eq. (8)).
3. Identify the intersection of the true stress-strain curve obtained via the DIC virtual strain gage (true stress calculated using Eq. (8)) with its slope.

Representative necking locations for the four metals under investigation are shown in Figure 13. A key takeaway is that necking occurs early in the plastic deformation history (i.e., shortly after yield) for 17-4 PH stainless steel (a BCC metal) and Ti-6Al-4V (a HCP metal), and later in the plastic deformation history of Inconel 625 and 718 (both FCC metals). Another key takeaway is that the three independent necking identification methods generally converge to an acceptably similar necking location (within 10% strain) across the spectrum metals. In this thesis, we hereafter employ method #3.

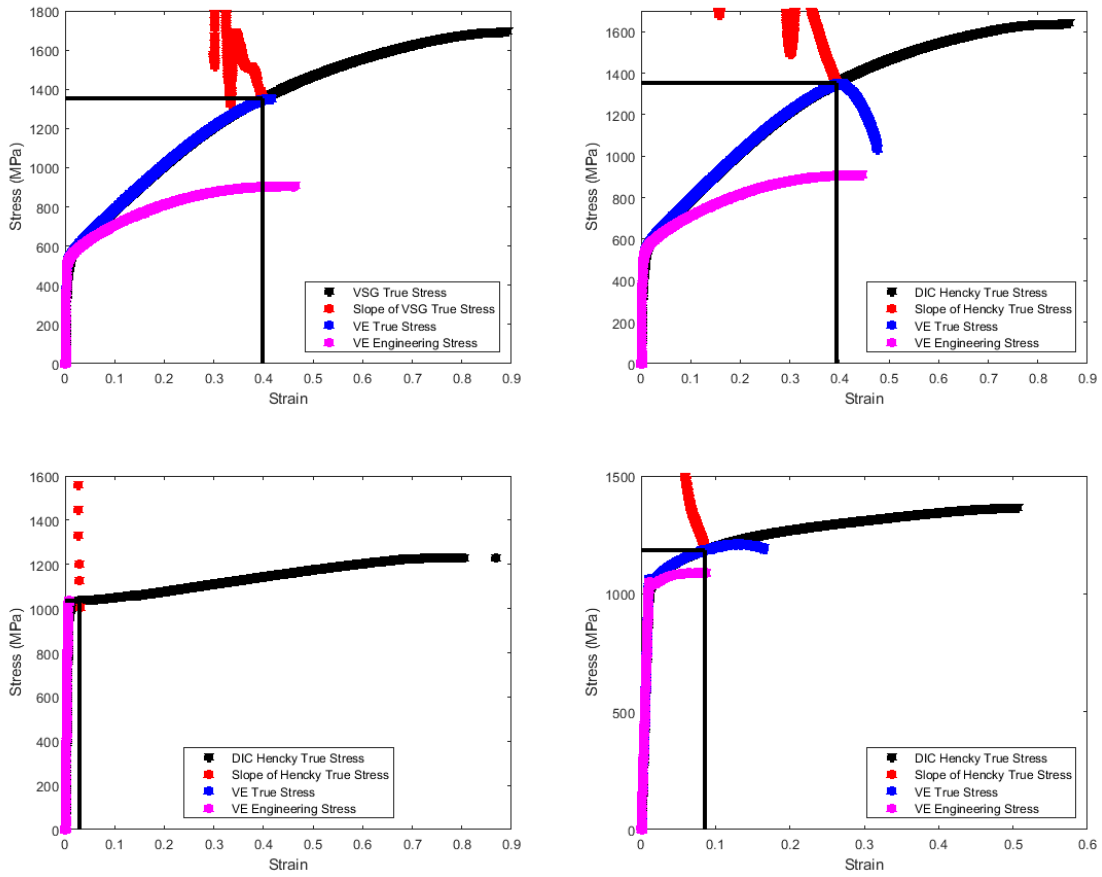

Figure 13: Necking Location for Inconel 625 Test #1 (Top Left), Inconel 718 Test #1 (Top Right), 17-4 PH Stainless Steel Test #5 (Bottom Left), and Ti-6Al-4V Test #2 (Bottom Right)

Depending on the sampling rate, the test data may be populated with an excessive amount of data points. The inherent noise can make it hard to identify actual behavior on a local scale. Because of this, data smoothing can be completed to maintain data integrity while diminishing local minima and maxima that come from high sampling rates. The equivalent true stress-strain curve with our post-necking correction (Figure 13, black markers) was smoothed using the `movmean` function in MATLAB (MathWorks, v. R2020b, Natick, MA). The `movmean` function executes a moving average over a user-specified number of data points, which varied between 20 and 80 points, to the left and to the right of each data point depending on the sampling rate of the

experiment. Figure 14 illustrates how the moving average removes local noise in the raw data without compromising its integrity.

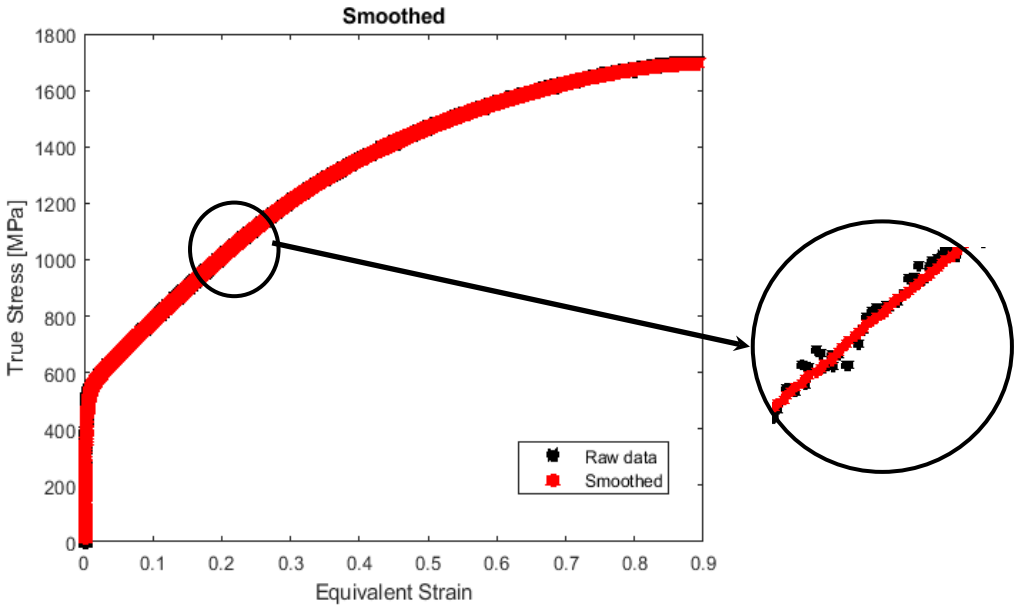

Figure 14: Data Smoothing of Representative Inconel 625 True Stress-Strain Curve

A moving average was also used on the slope of the true stress-strain curve (Figure 13, red markers), which ensured that the curves intersected appropriately, correctly identifying the necking point.

2.3.3 Integration of our Approach in an Iterative FEMU Scheme

Finite element model updating (FEMU) is an iterative approach used to correct post-necking true stress-strain response. This approach involves inputting a suite of trial post-necking equivalent true stress-strain curves into finite-element software. For each candidate curve, a finite-element simulation matching the exact conditions of the physical test is run. The true stress-strain curve that produces the best agreement between simulation and experiment – ascertained, for instance, by minimizing a cost function (per a specified convergence criterion or termination

threshold) reflecting error between force-displacement and surface principal strains – is ultimately adopted.

In this work, we generate a "fan" of trial post-necking equivalent true stress-strain curves (Figure 15), similar to Haight et al. [43]. This fan was created using a logarithmically spaced vector of varying hardening exponents, and typically contained 5 or 6 prospective curves. The post-necking equivalent true stress-strain ($\bar{\sigma}_{true}$ vs. $\bar{E}_{true}$) curve calculated using our novel approach in Sec. 2.3.1 provides an upper bound on the "fan," thereby limiting candidate curve space.

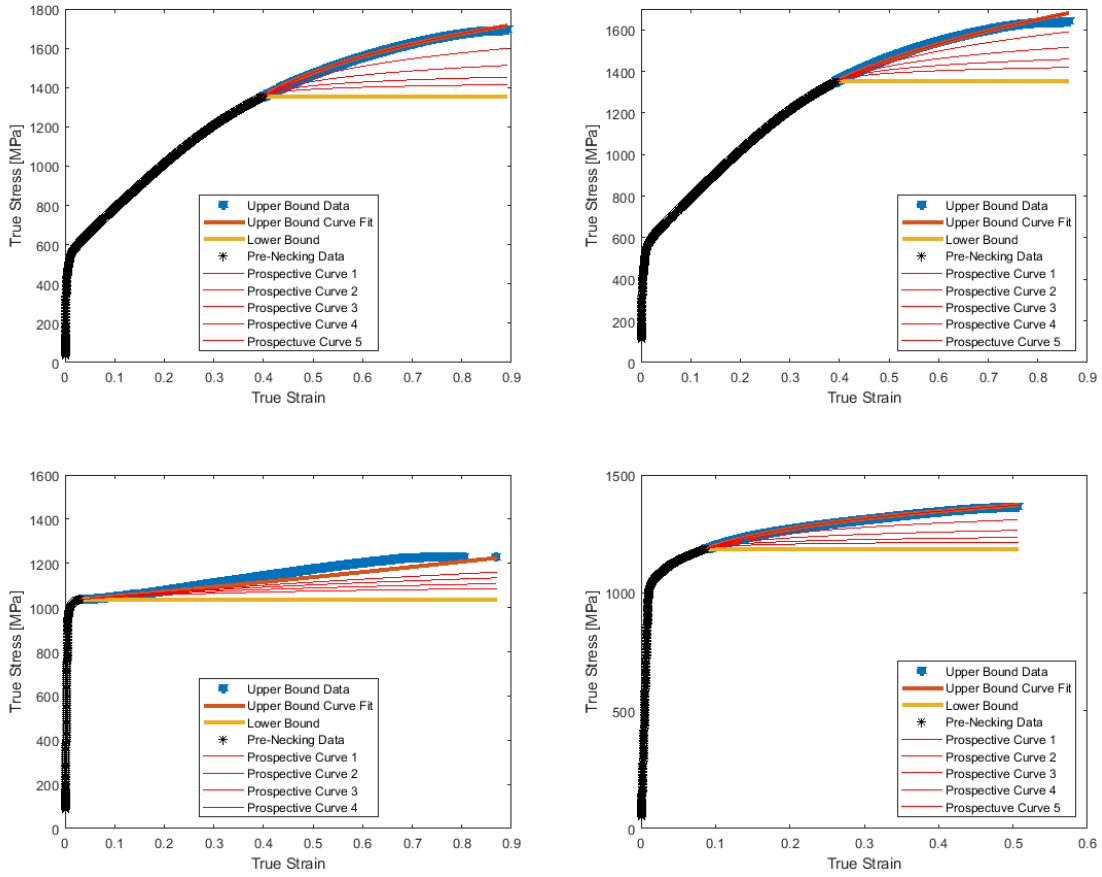

Figure 15: "Fan" of Trial Post-Necking Equivalent True Stress-Strain Curves for Inconel 625 Test #1 (Top Left), Inconel 718 Test #1 (Top Right), 17-4 PH Stainless Steel Test #5 (Bottom Left), and Ti-6Al-4V Test #2 (Bottom Right).

Our post-necking $\bar{\sigma}_{true}$ vs. $\bar{E}_{true}$ curve is regarded as an upper bound because it generally predicts stiffer behavior than observed and measured in the corresponding test. Our post-necking $\bar{\sigma}_{true}$ vs. $\bar{E}_{true}$ curve also serves as the first guess in the iterative FEMU process. The lower bound on the "fan" is perfect plasticity. In between, additional trial curves (with a smaller strain hardening exponent) are generally needed to converge to the exact material behavior. To generate this "fan" of prospective curves, continuous extrapolation is performed post-necking according to the Swift hardening law [38]:

$$\bar{\sigma}_{true} = K(E_0 - \bar{E}_{true})^n \tag{9}$$

where K, E_0, and n are adjustable material parameters. The hardening exponent, n, is altered to provide various trial curves evenly spaced out inside of the fan, while K and E_0 are constrained to maintain continuity of the curve at the necking point with the extrapolated trial curve. Of the five tests conducted on each metal, one representative test is chosen for further processing; the other four will serve as validation experiments. Eq. (9) is curve fit to our post-necking $\bar{\sigma}_{true}$ vs. $\bar{E}_{true}$ data. The curve fit yields values for K and E_0 (which are used for subsequent trial curves in the "fan") as well as a hardening exponent, n, for the upper bound (first guess) equivalent true stress-strain curve. The lower bound of this "fan" is perfect plasticity with a hardening exponent $n = 0$. The trial true stress-strain curves in Figure 15 are subsequently used as prospective input curves for a parallel finite element simulation of the corresponding physical tensile test (Sec. 2.4). The curve that best matches the material response (force vs. displacement and principal Hencky surface strains) observed in the tensile test generally falls somewhere between the upper and lower bound curves.

2.3.4 Linear Post-Necking Hardening: Interpolation Between Necking and Fracture

In this section, a non-iterative post-necking correction is proposed. This method is predicated on linear interpolation between necking and fracture, where the equivalent true stress and strain at

both locations are calculated using the approach described in Sec. 2.3.1. Using this methodology, linear post-necking curves for Inconel 625, Inconel 718, 17-4 PH stainless steel, and Ti-6Al-4V are created and illustrated in Figure 16 through Figure 19. This process is done for one representative test on each metal, with the other four tests serving as validation experiments. In all cases, the linear post-necking curves lie within the "fan" of prospective curves generated in Sec. 2.3.3, though there is no iteration required in this method. The equivalent true stress-strain curves in Figure 16 through Figure 19 serve as input for a parallel finite element simulation of the corresponding physical tensile test (Sec. 2.4).

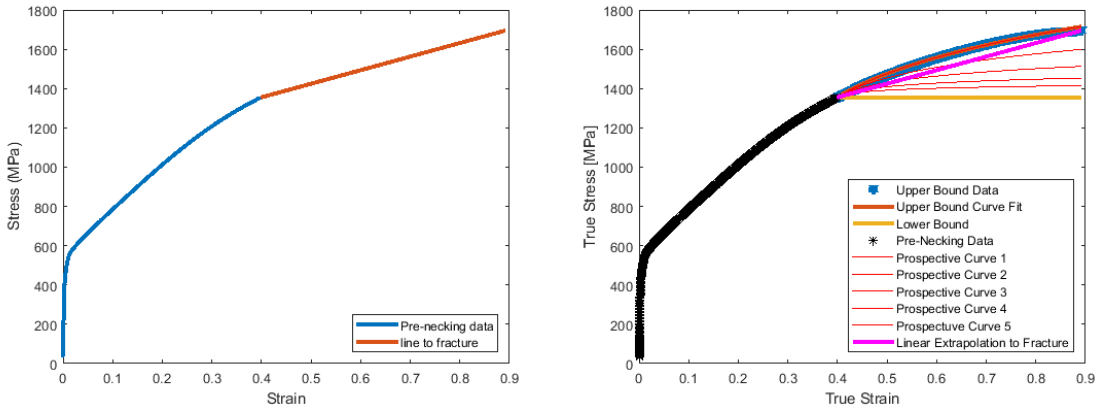

Figure 16: Left: Inconel 625 Linear Post-Necking Hardening Curve (Brown) via Linear Interpolation Between Necking and Fracture (Test #1). Right: Comparison of Post-Necking Curves (Test #1).

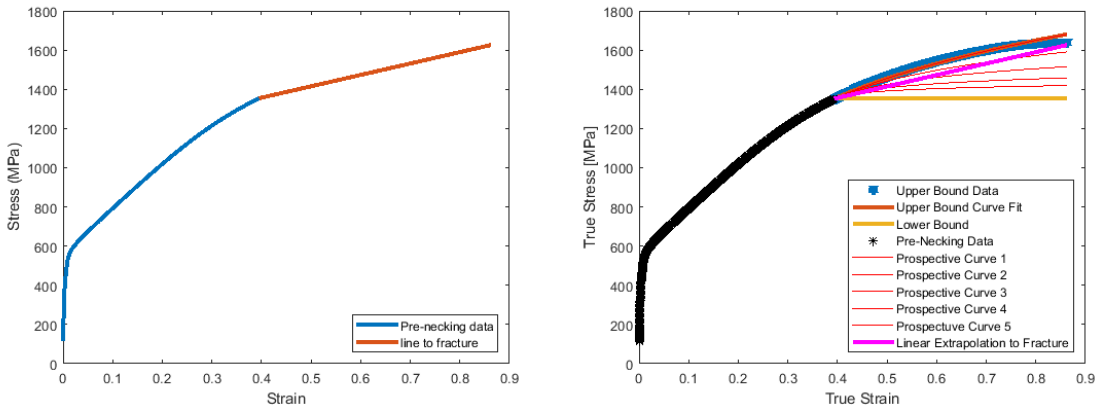

Figure 17: Left: Inconel 718 Linear Post-Necking Hardening Curve (Brown) via Linear Interpolation Between Necking and Fracture (Test #1). Right: Comparison of Post-Necking Curves (Test #1).

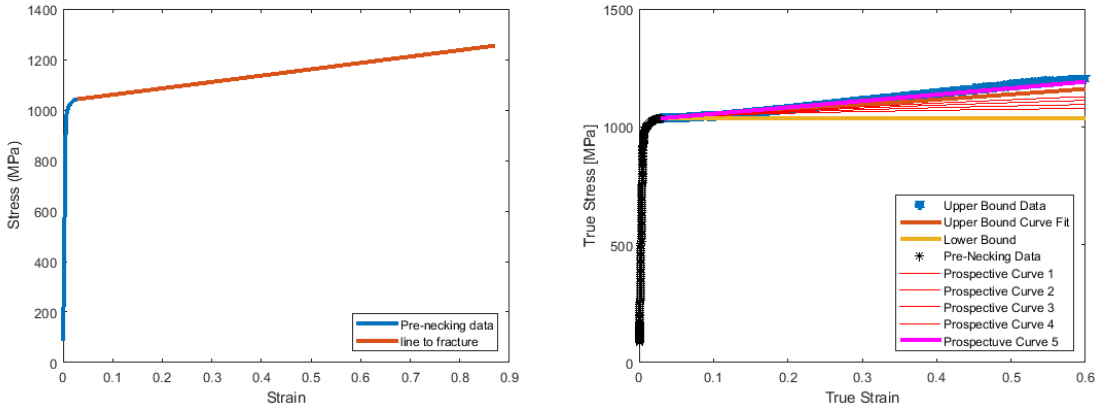

Figure 18: Left: 17-4 PH Stainless Steel Linear Post-Necking Hardening Curve (Brown) via Linear Interpolation Between Necking and Fracture (Test #5). Right: Comparison of Post-Necking Curves (Test #5).

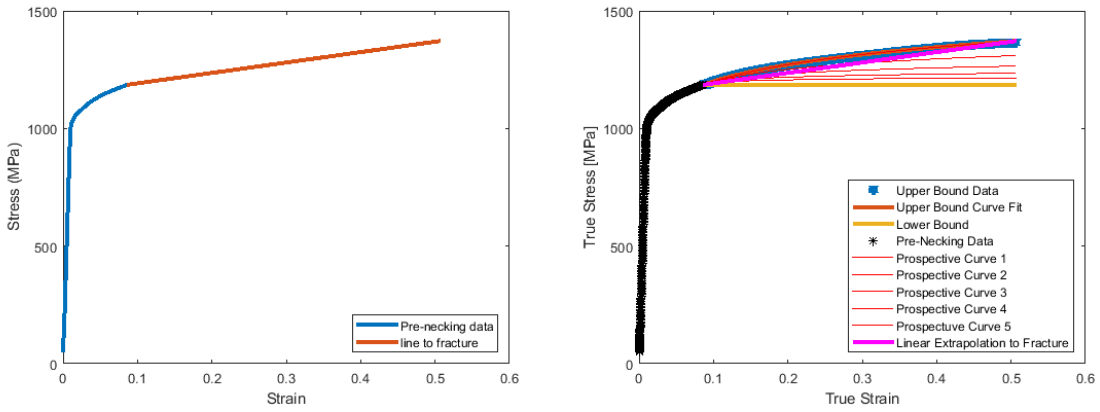

Figure 19: Left: Ti-6Al-4V Linear Post-Necking Hardening Curve (Brown) via Linear Interpolation Between Necking and Fracture (Test #2). Right: Comparison of Post-Necking Curves (Test #2).

2.4 Finite Element Simulations

2.4.1 3D Solid Modeling and Meshing

SolidWorks (DASSAULT SYSTEMES, 2019-2020 Student Edition, Waltham MA) computer-aided design (CAD) software was used to create a 3D solid model of each specimen in the test series. It is important to model each test specimen to its exact dimensions (not the nominal dimensions in Figure 10 to best match the simulation to its respective test. Each 3D solid model was then imported into HyperMesh (HyperWorks, v. 2019.1, Altair, Troy, MI) for finite element meshing (Figure 20).

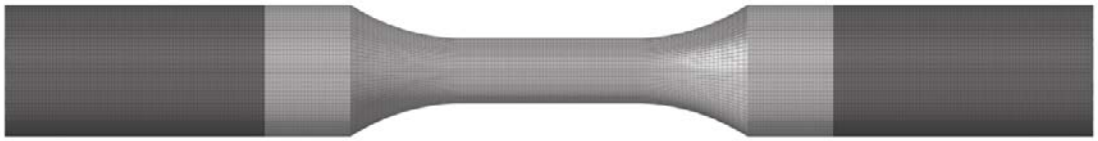

Figure 20: Representative Meshed Specimen

A characteristic element size of 0.21875 mm was selected to match the virtual strain gage size used for digital image correlation measurements (Table 4). Each specimen contained about 600,000 elements. The typical element density in the specimen gage was about 34 elements across its diameter.

2.4.2 Finite Element Modeling and Simulation Details

Numerical simulations were performed using an explicit solver in the commercial finite-element code LS-DYNA® (version R10.1.0, Ansys/LST, Livermore, CA). Three-dimensional, constant-stress, 8-node, solid hex elements (ELFORM = 1) were used in the simulations. To account for the tendency of under-integrated elements to hourglass, stiffness-based hourglass control (IHQ = 6) was employed with an hourglass coefficient QH = 0.1. Hourglass energies imposed by the hourglass control algorithm were found to be acceptably low in all simulations.

The specimen grip sections (denoted by dark gray shading in Figure 20) were assumed to constitute approximately 75% of the shoulders, consistent with the experiments. One of the grip sections was held fixed (with all translational and rotational degrees of freedom constrained), while the other was prescribed an “artificial” constant velocity of 1 m/s. This “artificial” actuation speed is sufficiently high to meaningfully reduce the computational cost of explicitly simulating a quasi-static test, but sufficiently low to not introduce inertial effects, often observed as transient oscillations in material response (e.g., force vs. displacement) near simulation startup. Checking that the kinetic energy is an insignificant ratio of the internal energy also ensures minimized dynamic effects. A rigid material model (*MAT_020) was assigned to both grip sections. The motion of the rigid gripped sections of the specimen was restricted using a center of mass constraint (CMO = 1) in *MAT_20. For the fixed grip section, the following constraint parameters were set to CON1 = CON2 = 7 to constrain all translational and rotational degrees of freedom. The gripped section driven by the uniaxial actuator was constrained using CON1 = 5, CON2 = 7 so that only axial translation was permitted. The ungripped section of the specimen

(denoted by light gray shading in Figure 20) was modeled using the *MAT_024 material card. This elasto-plastic constitutive model requests as input density (Table 5), linear elastic material parameters (modulus of elasticity and Poisson's ratio (Table 5)), as well as post-yield equivalent true stress-strain curve. Running in shared-memory parallel on eight CPUs, the simulations took anywhere from 12-24 hours, depending mostly on the ductility of the metal. Because the same velocity was used across all metals, a larger ductility (failure strain) required a longer simulation termination time, which directly relates to computational expense.

Table 5: Elastic Material Properties for MAT_024 Input

Metal	Density (tonne/mm^3)	Elastic Modulus (GPa)	Poisson's ratio
In625	8.44e-09	244	0.278
In718	8.19e-09	105	0.284
17-4 PH SS	7.78e-09	151	0.272
Ti-6Al-4V	4.43e-09	104	0.342

2.5 Results

Material properties (mean ± one standard deviation) for each of the four metal alloys are reported in Table 6. The elastic modulus was obtained through a linear regression of the pre-yield, linear elastic portion of the stress-strain curve. The yield point was taken to coincide with the proportional limit, i.e., the transition from linear to nonlinear true stress-strain response. The ultimate tensile strength (UTS) was obtained as the absolute maximum of the post-yield true stress-strain curve. The failure strain is the true strain reported by the DIC VSG at specimen fracture, defined here as initial material separation in the specimen gage section.

Table 6: Material Properties (Mean +/- Standard Deviation)

Metal	Elastic Modulus (GPa)	Yield Strength (MPa)	UTS (MPa)	Failure Strain
In625	100.4 ± 34.57	451.7 ± 63.78	1699 ± 6.210	0.8861 ± 0.0112
In718	158.4 ± 17.66	425.4 ± 16.42	1637 ± 7.940	0.8843 ± 0.0375
Ti64	105.8 ± 50.13	1004 ± 13.65	1389 ± 32.35	0.5136 ± 0.0134
SS 17-4 PH	194.7 ± 118.7	1009 ± 15.68	1248 ± 5.940	0.8563 ± 0.0475

To assess agreement between simulation and experiment, the error in measured quantities – namely axial force vs. axial displacement and principal Hencky surface strains (maximum E1 and minimum E2) vs. displacement – was quantified. Displacement in each test was calculated from the virtual extensometer, and force was obtained from the load cell. Displacement in each simulation was calculated by tracking the axial elongation of two nodes whose initial separation correlates with the virtual extensometer length; force was obtained on a cross-sectional plane placed on the anticipated fracture plane (i.e., the cross-sectional plane containing the most highly strained elements). Principal Hencky surface strain histories in the tests were measured using a DIC virtual strain gage placed at the failure location. Principal surface strain histories in the simulations were obtained from a representative surface element on the anticipated fracture plane. Because the simulation is symmetric, any element on either side of the anticipated fracture plane will report the same surface strain values.

The error between simulation and experiment was quantified for each metric (force vs. displacement and principal surface strains vs. displacement) using the normalized mean squared error:

$$NMSE = \frac{MSE}{\sum_{i=1}^{N} Test_i^2} \tag{10}$$

with the mean squared error given by:

$$MSE = \frac{1}{N}\sum_{i=1}^{N}(Test_i - Simulation_i)^2 \tag{11}$$

In Eqs. (10) and (11), N is the total number of data points, $Test_i$ is the experimental value for force or principal strain at the i-th (displacement) data point, and $Simulation_i$ is the simulation value for force or principal strain at the i-th (displacement) data point. The error was normalized against the test values for easier comparison of the magnitude of error.

2.5.1 Inconel 625

2.5.1.1 Iterative Approach

The "fan" of trial post-necking equivalent true stress-strain curves for Inconel 625 Test #1 (Figure 15) was used as the basis for an iterative FEMU approach (Sec. 2.3.3). In the implementation, a cost function (with a specified convergence criterion or termination threshold) exploring the full (continuous) parameter range of the post-necking hardening exponent n (between perfect plasticity and upper bound) was not employed. Rather, the (discrete) trial curve from Figure 15 that produces the lowest normalized mean squared error between test and experiment was adopted as the "optimal" equivalent true stress-strain curve.

The first guess (upper bound with a post-necking hardening exponent $n = 0.1547$) simulation agrees well with the experiment until larger strains (Figure 21), where the force vs. displacement and principal strain vs. displacement results diverge.

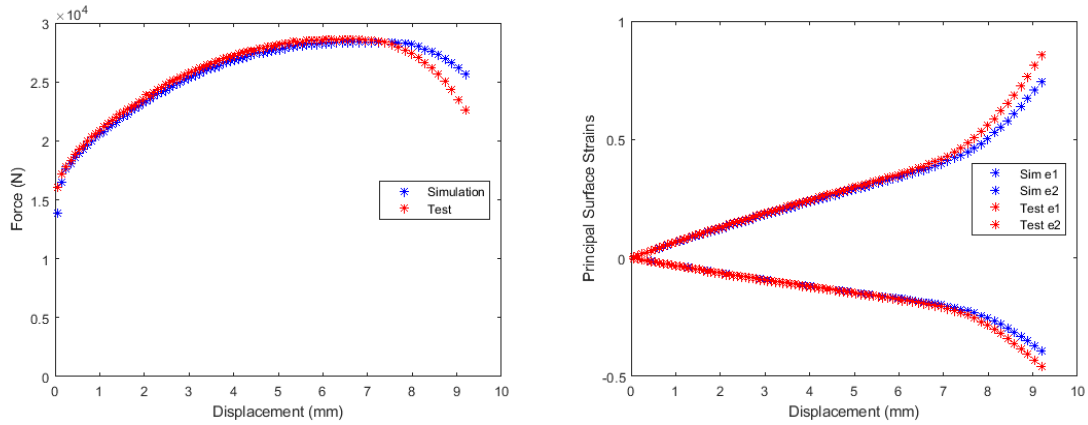

Figure 21: Inconel 625 FEMU First Guess (Test #1)

In particular, the simulation over-predicts the amount of force needed to displace the material, indicating that the first guess is too stiff. Thus, a second guess (first interior curve in Figure 15 with a lower post-necking hardening exponent $n = 0.0801$) was taken from the "fan" of prospective curves. The second guess results in excellent agreement between simulation and experiment (Figure 22), with a reduction in normalized mean square error for all comparison metrics (Table 7). Use of a third guess (not shown) does not improve error metrics. Therefore, the equivalent true stress-strain curve corresponding to Test #1, Guess #2 was selected as our "optimal" candidate.

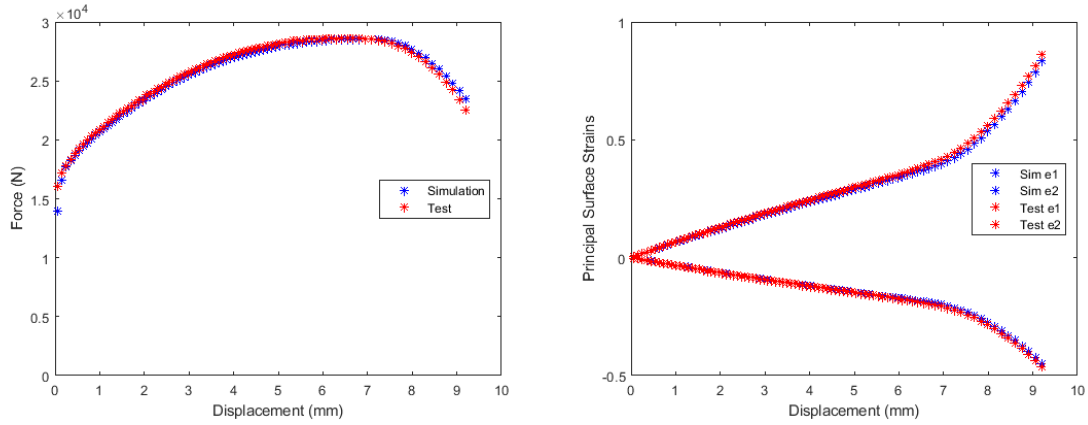

Figure 22: Inconel 625 FEMU Second Guess (Test #1)

Table 7: Inconel 625 Test #1 Normalized Mean Square Error Comparison

Test	Force	e1	e2
In625 Test #1 1st Guess	1.05e-07	1.40e-06	1.86e-06
In625 Test #1 2nd Guess	2.25e-08	2.27e-07	1.61e-07

Next, for validation purposes, the true stress-strain behavior from Test #1, Guess #2 was used to simulate the remaining four experiments in the Inconel 625 tensile test series. Excellent agreement is observed between simulation and experiment in Test #2 (Figure 23), Test #4 (Figure 25) and Test #5 (Figure 26), corroborated by the error metrics in Table 8. In Test #3 (Figure 24), where the agreement is only acceptable, the discrepancy is attributed to premature failure outside of the specimen gage section.

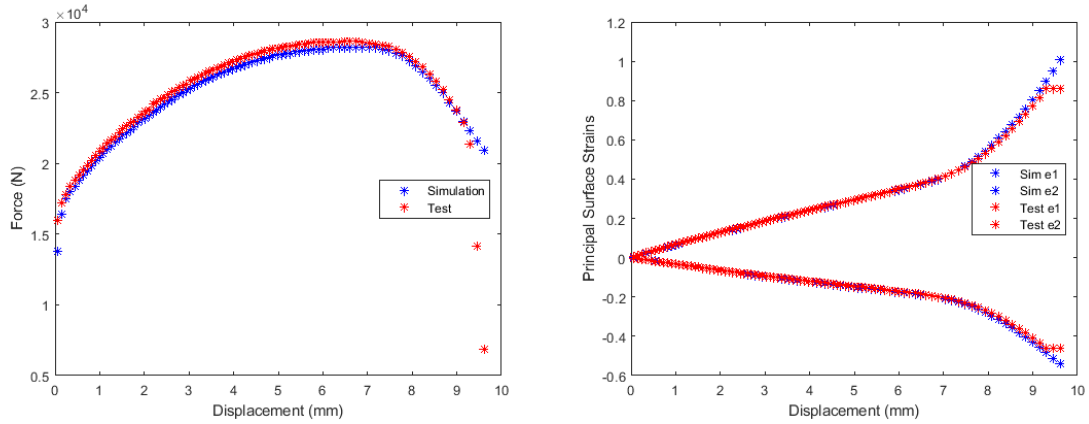

Figure 23: Inconel 625 FEMU Validation (Test #2)

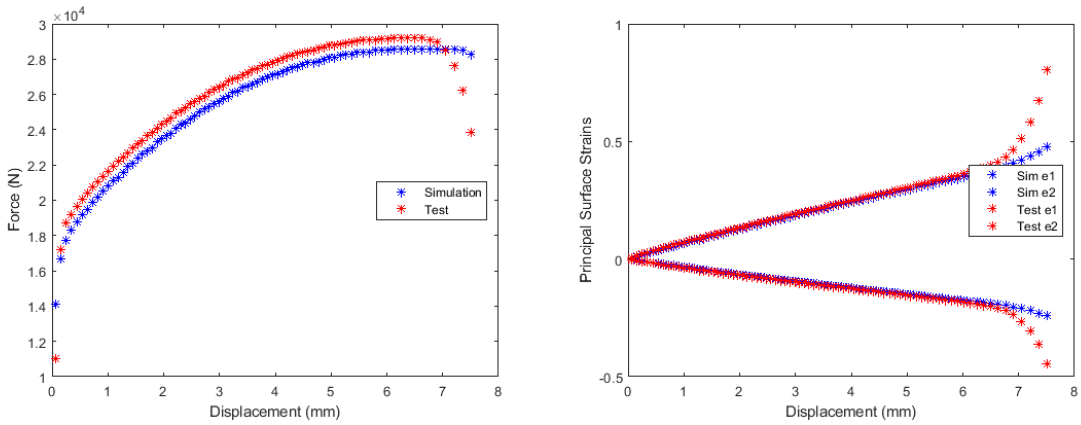

Figure 24: Inconel 625 FEMU Validation (Test #3)

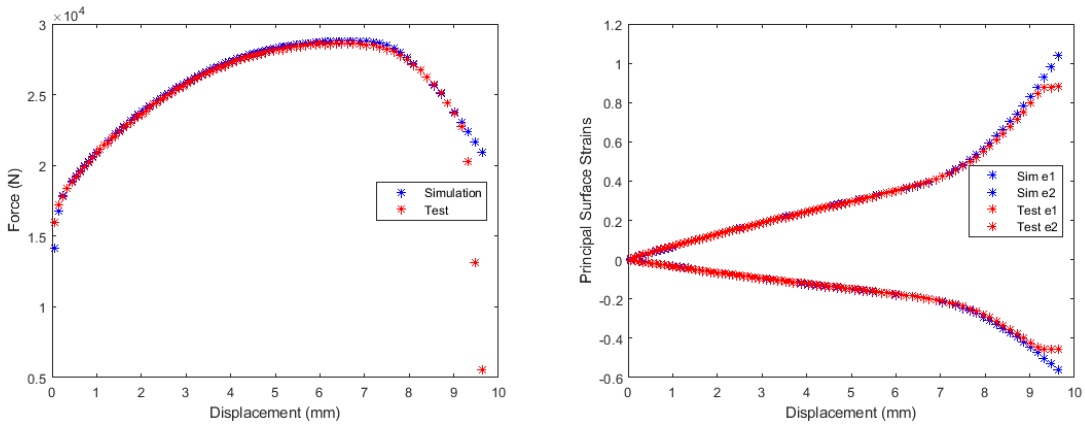

Figure 25: Inconel 625 FEMU Validation (Test #4)

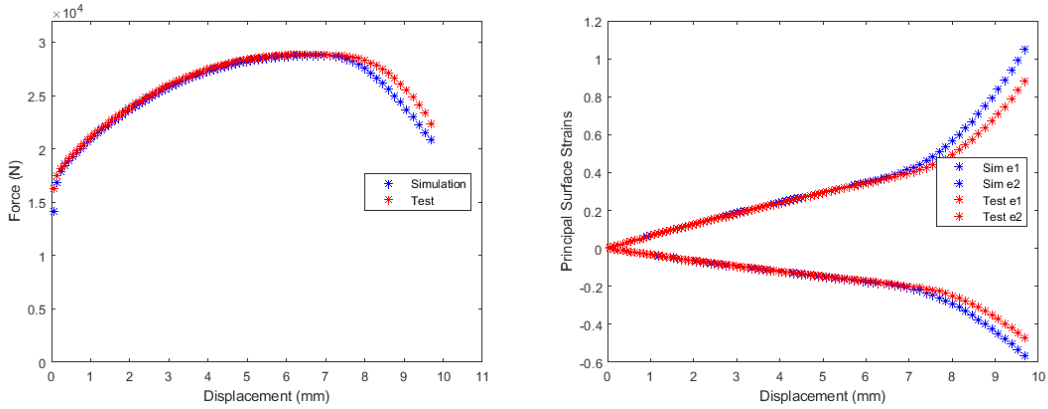

Figure 26: Inconel 625 FEMU Validation (Test #5)

Table 8: Inconel 625 FEMU Validation Normalized Mean Square Error Comparison

Test	Force	e1	e2
In625 Test #2	4.90e-08	1.13e-07	3.09e-07
In625 Test #3	2.52e-07	7.98e-06	1.18e-05
In625 Test #4	1.15e-08	1.33e-07	2.97e-07
In625 Test #5	7.21e-08	3.27e-06	4.48e-06

2.5.1.2 Linear Interpolation

The non-iterative post-necking correction based on linear interpolation between necking and fracture described in Sec. 2.3.4 is employed for Inconel 625 Test #1 (Figure 27). Agreement between simulations and experiment for Test #1 (Figure 27) is excellent. Following, the Test #1 input curve was used in the simulations of Inconel 625 Tests #2-#5. As a result, a normalized mean square error comparison (cf. Table 7, Table 8, and Table 9) shows that linear interpolation is roughly on the same magnitude as our FEMU approach in predicting principal surface strains, but slightly underperforms at predicting force. This agreement is particularly impressive given the simplicity of generating a linear hardening curve between necking and fracture, and that no iteration is required among trial curves (or, more generally, post-necking hardening exponents n) to converge to the "optimal" material response.

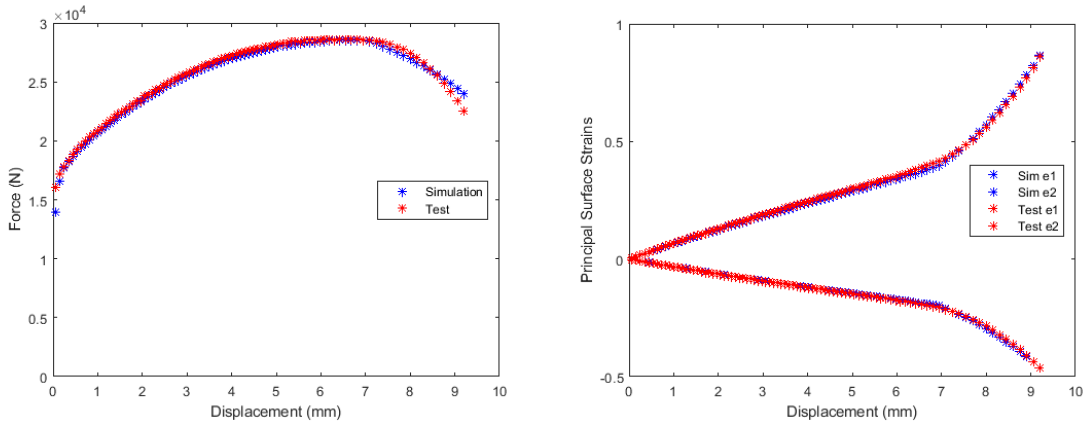

Figure 27: Inconel 625 Linear Interpolation (Test #1)

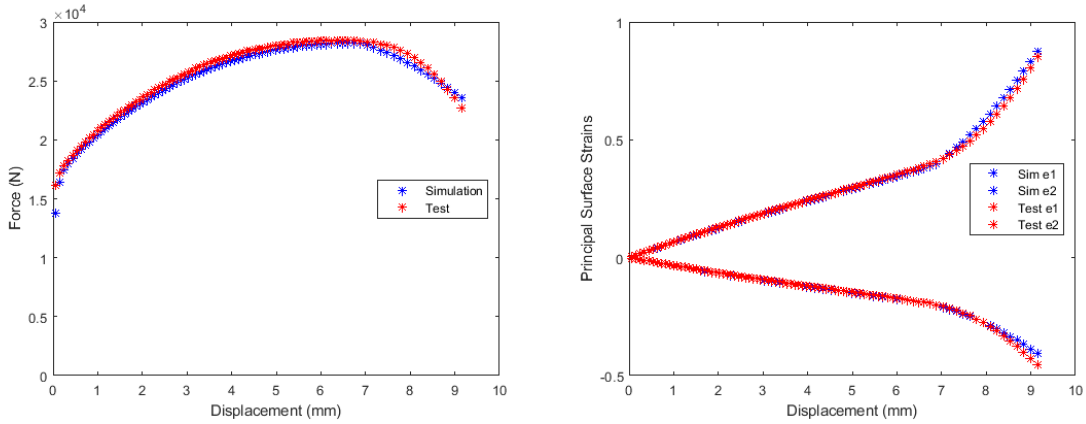

Figure 28: Inconel 625 Linear Interpolation (Test #2)

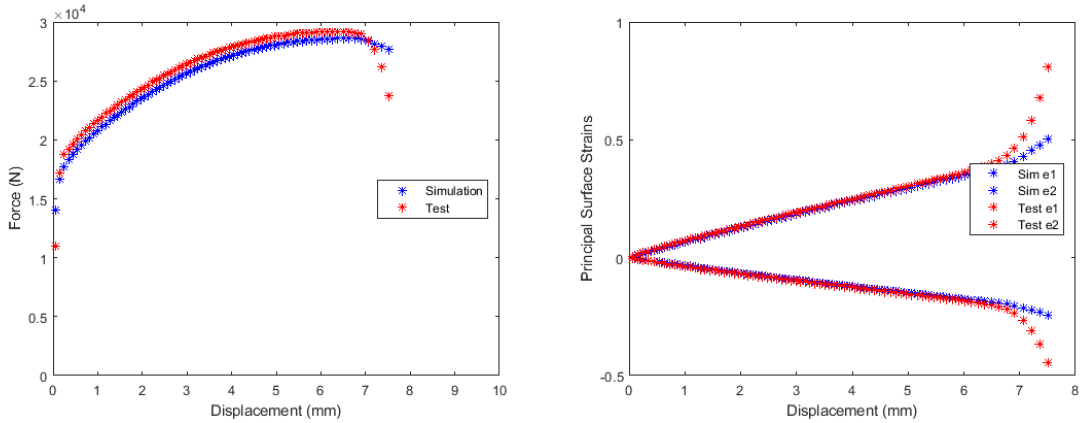

Figure 29: Inconel 625 Linear Interpolation (Test #3)

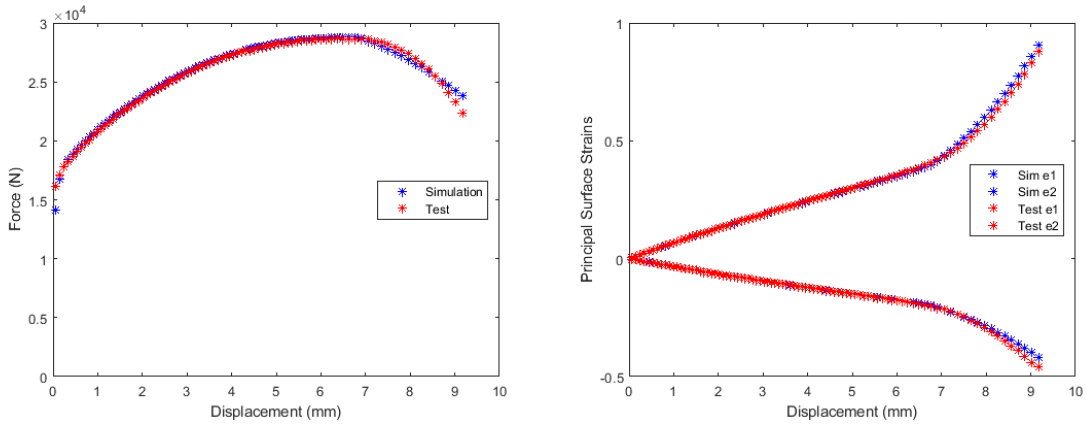

Figure 30: Inconel 625 Linear Interpolation (Test #4)

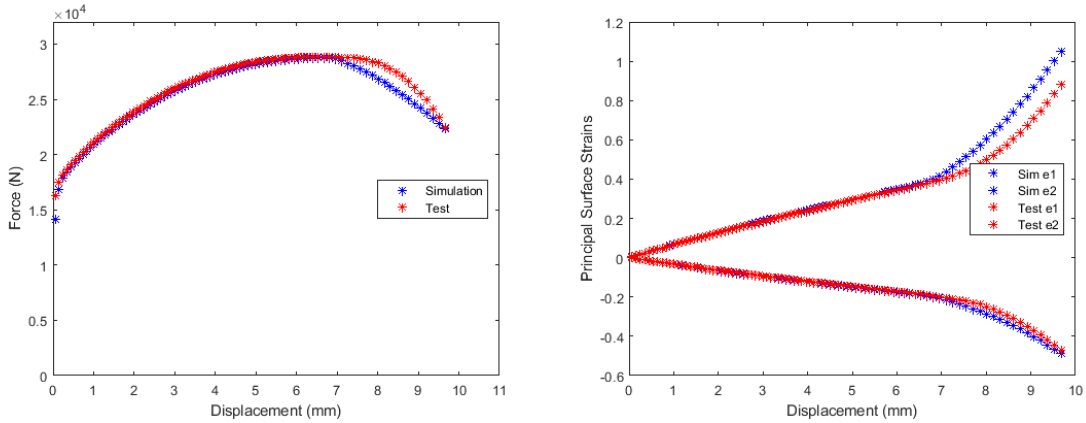

Figure 31: Inconel 625 Linear Interpolation (Test #5)

Table 9: Inconel 625 Linear Interpolation Normalized Mean Square Error Comparison

Test	Force	e1	e2
In625 Test #1	2.66e-08	9.86e-08	9.59e-08
In625 Test #2	4.59e-08	2.22e-07	4.93e-08
In625 Test #3	2.27e-07	6.78e-06	1.15e-05
In625 Test #4	2.17e-08	2.09e-07	5.01e-07
In625 Test #5	6.65e-08	4.89e-06	1.12e-06

2.5.2 Inconel 718

2.5.2.1 Iterative Approach

The "fan" of trial post-necking equivalent true stress-strain curves for Inconel 718 Test #1 (Figure 15) was used as the basis for an iterative FEMU approach (Sec. 2.3.3). In our implementations, a cost function (with a specified convergence criterion or termination threshold) exploring the full (continuous) parameter range of the post-necking hardening exponent n (betweem perfect plasticity and upper bound) was not employed. Rather, the (discrete) trial curve from Figure 15 that produces the lowest normalized mean squared error between test and experiment was adopted as the "optimal" equivalent true stress-strain curve.

The first guess (upper bound with a post-necking hardening exponent $n = 0.2011$) simulation agrees well with the experiment until larger strains (Figure 32), where the force vs. displacement and principal strains vs. displacement results diverge.

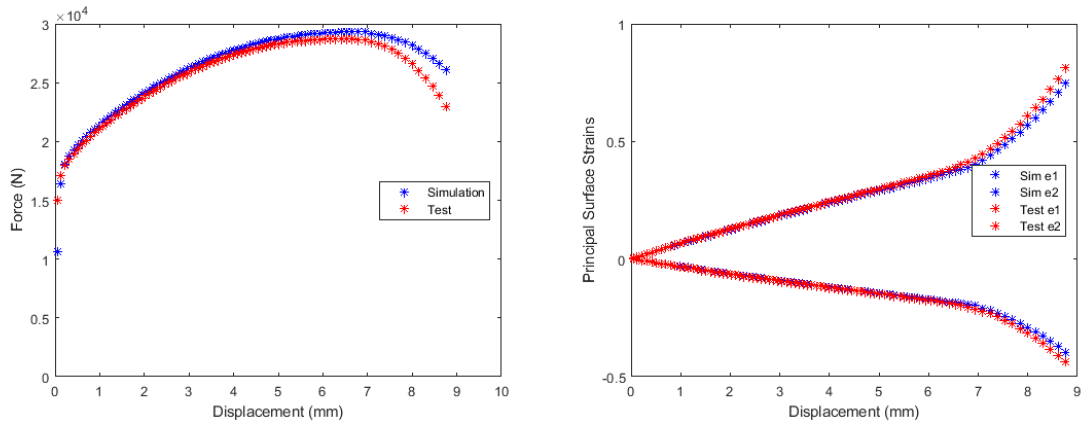

Figure 32: Inconel 718 FEMU First Guess (Test #1)

In particular, the simulation over-predicts the amount of force needed to displace the material, indicating that the first guess is too stiff. Thus, a second guess (first interior curve in Figure 15 with a lower post-necking hardening exponent $n = 0.1041$) was taken from the "fan" of prospective curves. The second guess results in excellent agreement between simulation and experiment (Figure 33), with a reduction in normalized mean squared error for all comparison metrics (Table 10). Use of a third guess (not shown) could slightly improve error metrics. However, the equivalent true stress-strain curve corresponding to Test #1, Guess #2 was selected as our "optimal" candidate.

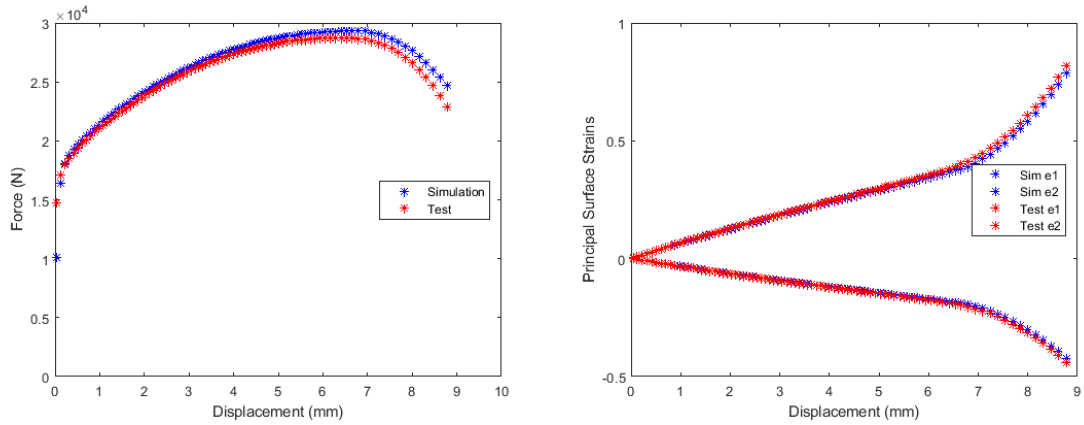

Figure 33: Inconel 718 FEMU Second Guess (Test #1)

Table 10: Inconel 718 Test #1 Normalized Mean Square Error Comparison

Test	Force	e1	e2
In718 Test #1 1st Guess	1.71e-07	5.61e-07	7.78e-07
In718 Test #1 2nd Guess	1.20e-07	2.70e-07	2.84e-07

Next, for validation purposes, the true stress-strain behavior from Test #1, Guess #2 was used to simulate the remaining four experiments in the Inconel 718 tensile test series. Excellent agreement is observed between simulation and experiment in Tests #2-#5 (Figure 34-Figure 37), corroborated by the error metrics in Table 11.

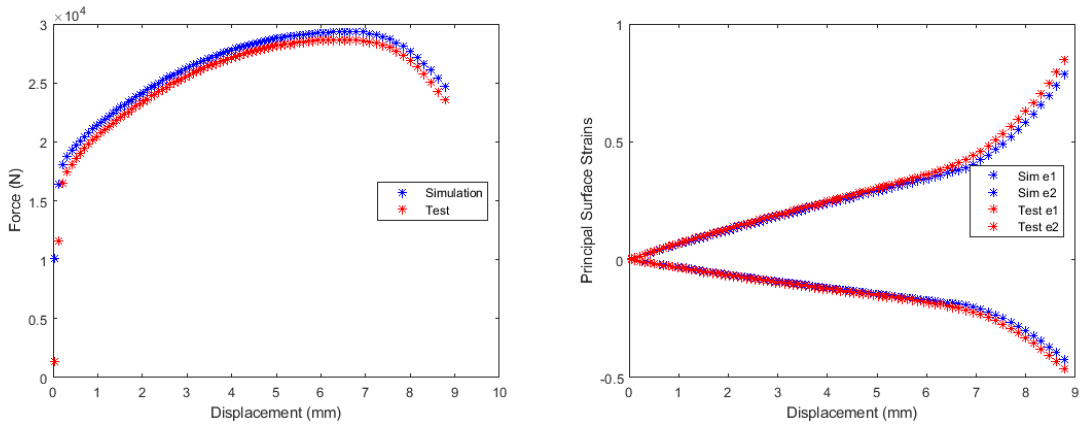

Figure 34: Inconel 718 FEMU Validation (Test #2)

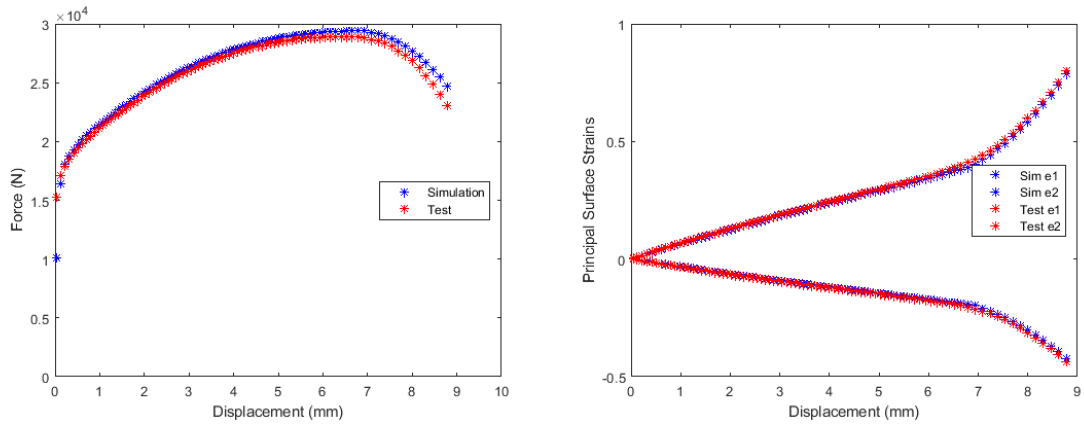

Figure 35: Inconel 718 FEMU Validation (Test #3)

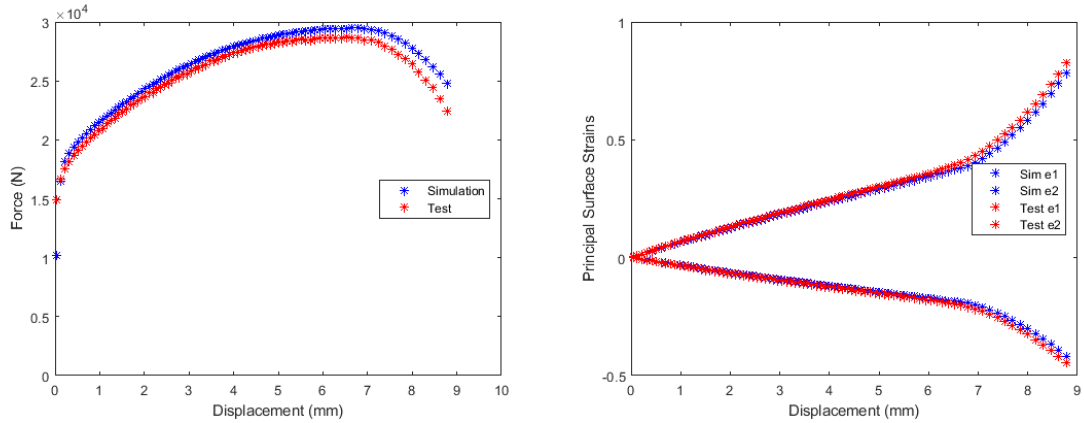

Figure 36: Inconel 718 FEMU Validation (Test #4)

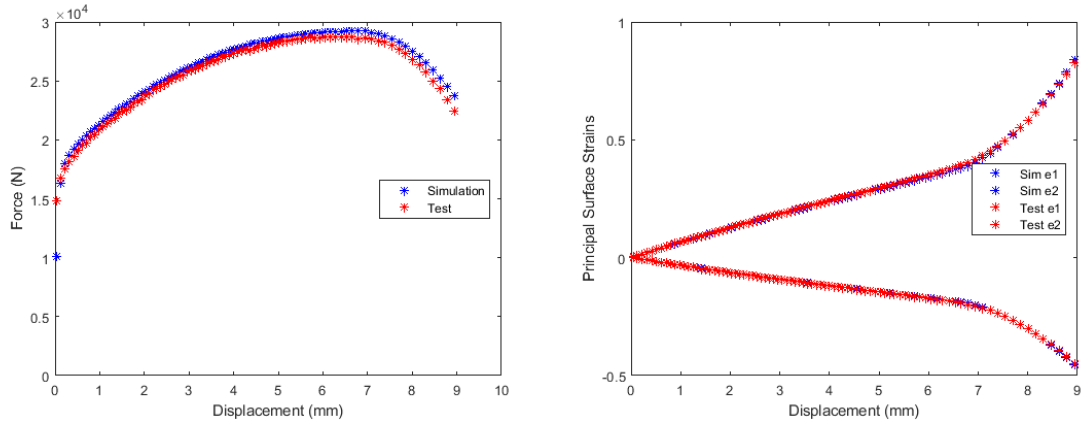

Figure 37: Inconel 718 FEMU Validation (Test #5)

Table 11: Inconel 718 FEMU Validation Normalized Mean Square Error Comparison

Test	Force	e1	e2
In718 Test #2	3.82e-07	8.22e-07	1.25e-06
In718 Test #3	1.13e-07	1.31e-07	2.57e-07
In718 Test #4	1.98e-07	4.81e-07	7.78e-07
In718 Test #5	1.01e-07	3.87e-08	1.87e-08

2.5.2.2 Linear Interpolation

The non-iterative post-necking correction based on linear interpolation between necking and fracture described in Sec. 2.3.4 is employed for Inconel 718 Test #1 (Figure 38). Agreement between simulations and experiment for Test #1 (Figure 38) is excellent. Following, the Test #1 input curve was used in the simulations of Inconel 625 Tests #2-#5 (Figure 39-Figure 42). As a result, a normalized mean square error comparison (cf. Table 10, Table 11, and Table 12) shows that linear interpolation is roughly on the same magnitude as our FEMU approach in predicting principal surface strains, but slightly underperforms at predicting force. This agreement is particularly impressive given the simplicity of generating a linear hardening curve between necking and fracture, and that no iteration is required among trial curves (or, more generally, post-necking hardening exponents n) to converge to the "optimal" material response.

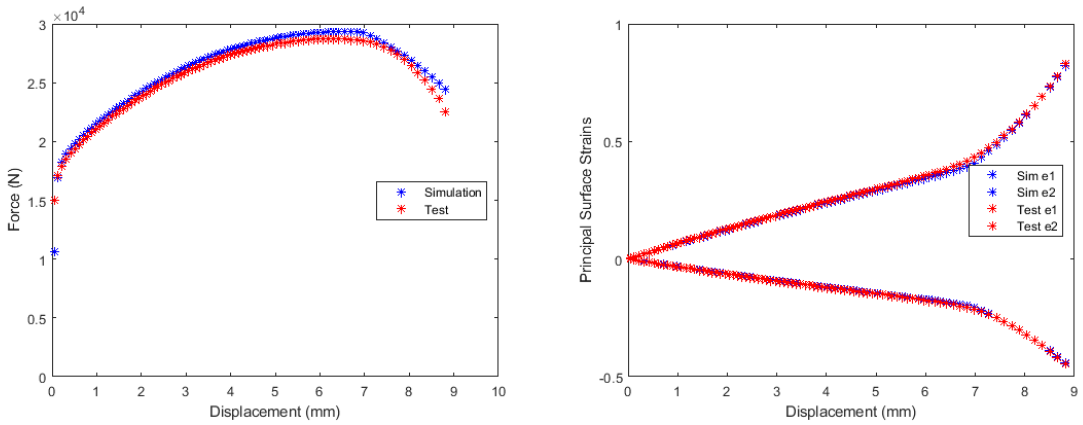

Figure 38: Inconel 718 Linear Interpolation (Test #1)

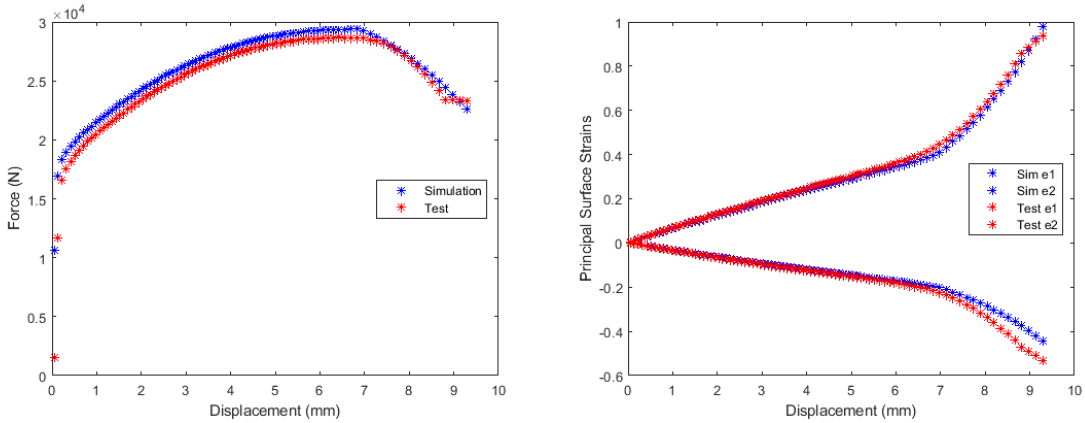

Figure 39: Inconel 718 Linear Interpolation (Test #2)

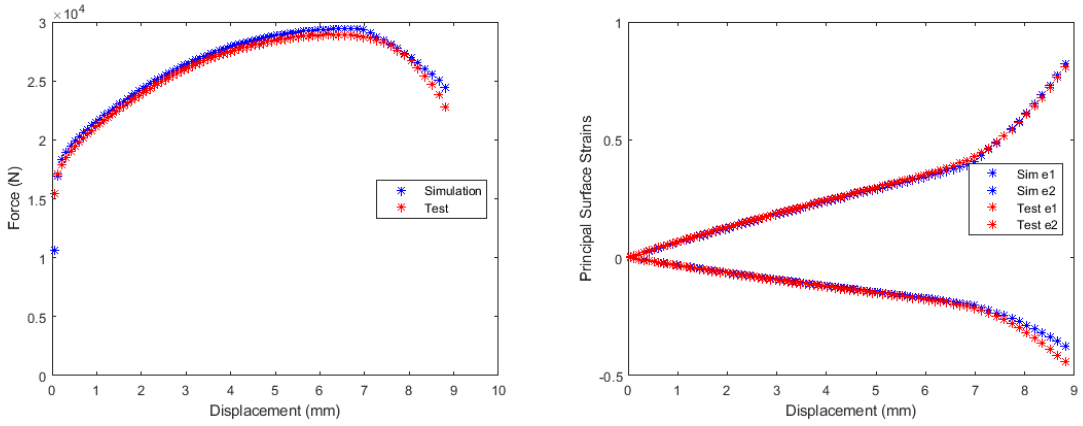

Figure 40: Inconel 718 Linear Interpolation (Test #3)

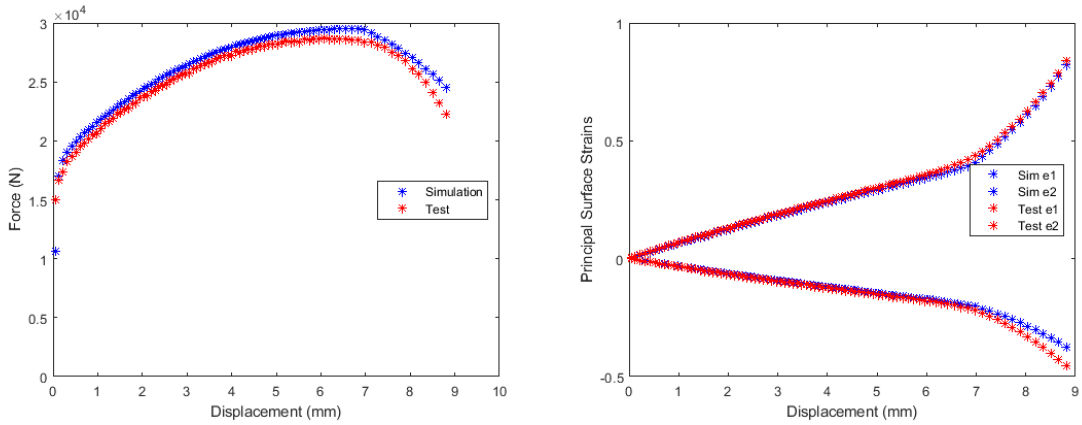

Figure 41: Inconel 718 Linear Interpolation (Test #4)

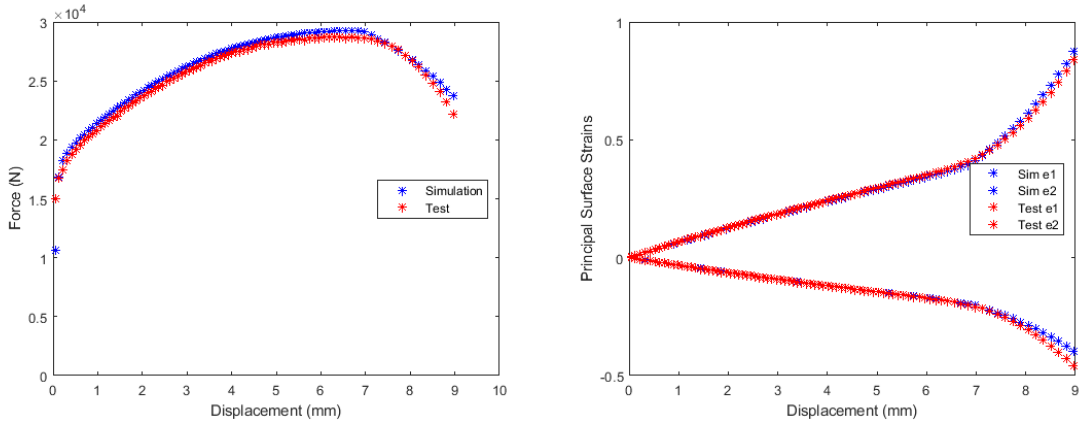

Figure 42: Inconel 718 Linear Interpolation (Test #5)

Table 12: Inconel 718 Linear Interpolation Normalized Mean Square Error Comparison

Test	Force	e1	e2
In718 Test #1	1.05e-07	9.34e-08	7.55e-08
In718 Test #2	3.77e-07	3.66e-07	4.33e-06
In718 Test #3	9.80e-08	7.87e-08	1.67e-06
In718 Test #4	1.80e-07	2.03e-07	2.70e-06
In718 Test #5	9.44e-08	1.79e-07	1.05e-06

2.5.3 17-4 PH Stainless Steel

2.5.3.1 Iterative Approach

The "fan" of trial post-necking equivalent true stress-strain curves for 17-4 PH Stainless Steel Test #5 (Figure 15) was used as the basis for an iterative FEMU approach (Sec. 2.3.3). In our implementation, a cost function (with a specified convergence criterion or termination threshold) exploring the full (continuous) parameter range of the post-necking hardening exponent n (between perfect plasticity and upper bound) was not employed. Rather, the (discrete) trial curve from Figure 15 that produces the lowest normalized mean squared error between test and experiment was adopted as the "optimal" equivalent true stress-strain curve.

The first guess (upper bound with a post-necking hardening exponent $n = 0.1556$) struggles to agree well with the experiment (Figure 43).

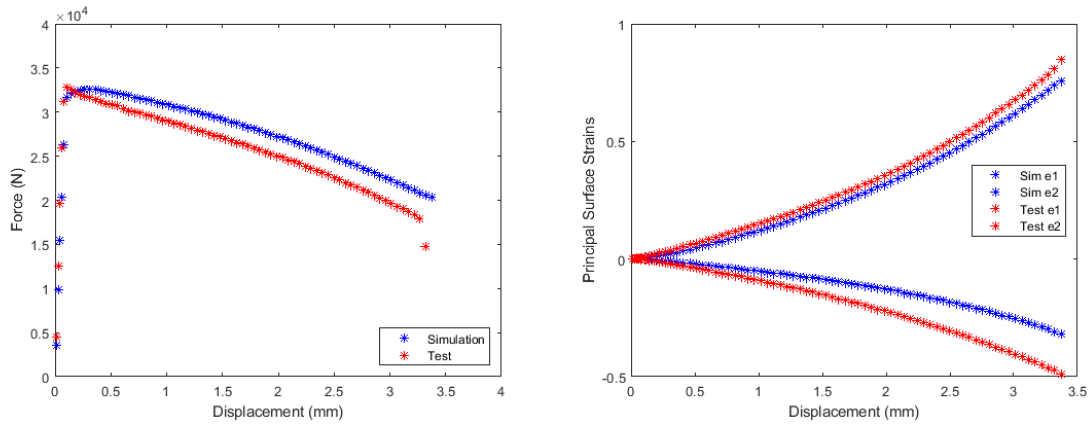

Figure 43: 17-4 PH Stainless Steel FEMU First Guess (Test #5)

In particular, the simulation over-predicts the amount of force needed to displace the material, indicating that the first guess is too stiff. Thus, a second guess (second interior curve in Figure 15 with a lower post-necking hardening exponent $n = 0.0417$) was taken from the "fan" of prospective curves. The second guess results in slightly better agreement between simulation and experiment (Figure 44), with a reduction in normalized mean square error for all comparison metrics (Table 13). Perhaps the use of a third guess (not shown) could improve error metrics. Ultimately, the equivalent true stress-strain curve corresponding to Test #5, Guess #2 was selected as our "optimal" candidate.

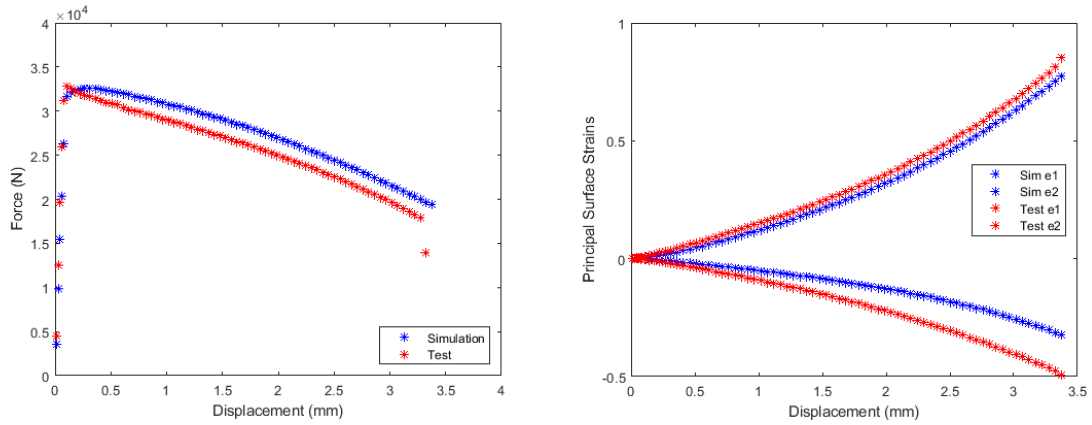

Figure 44: 17-4 PH Stainless Steel FEMU Second Guess (Test #5)

Table 13: 17-4 PH Stainless Steel Test #5 Normalized Mean Square Error Comparison

Test	Force	e1	e2
17-4 PH Stainless Steel Test #5 1st Guess	2.79e-06	3.18e-06	4.81e-05
17-4 PH Stainless Steel Test #5 2nd Guess	2.48e-06	2.65e-06	4.80e-05

Next, for validation purposes, the true stress-strain behavior from Test #5, Guess #2 was used to simulate the remaining four experiments in the 17-4 PH stainless steel tensile test series. Agreement was less favorable likely due to the early necking (just after yield). Comparison between simulation and test for Tests #1-#4 (Figure 45-Figure 48) is corroborated by the error metrics in Table 14.

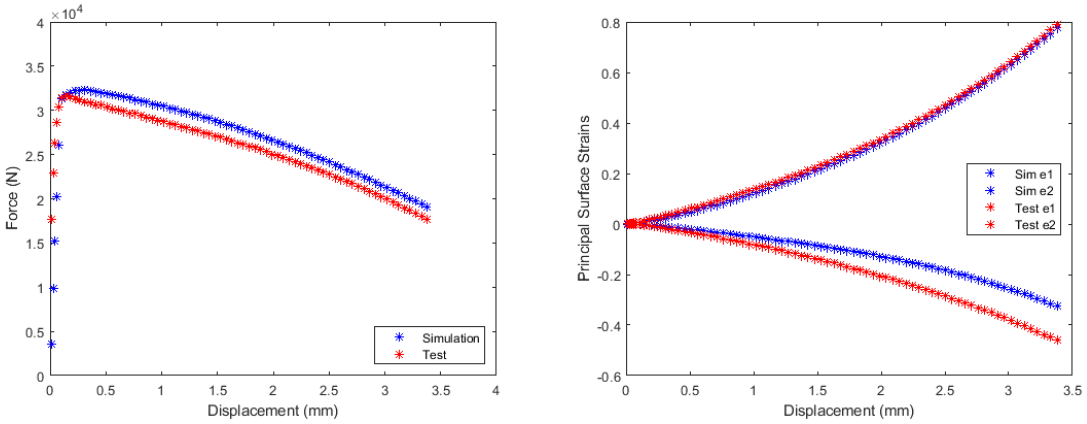

Figure 45: 17-4 PH Stainless Steel FEMU Validation (Test #1)

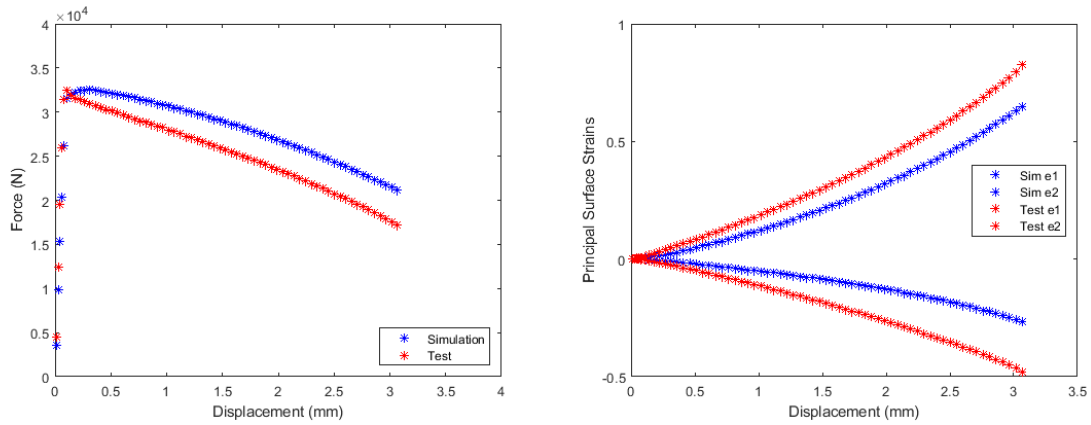

Figure 46: 17-4 PH Stainless Steel FEMU Validation (Test #2)

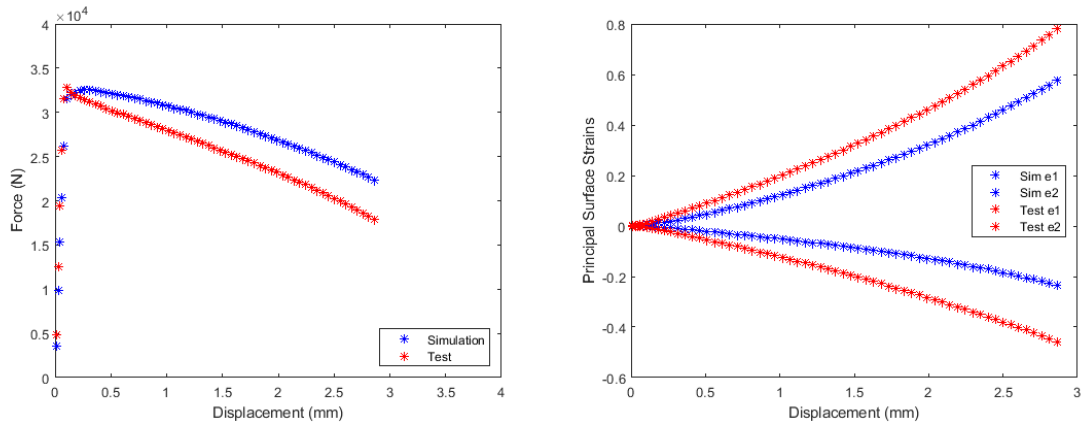

Figure 47: 17-4 PH Stainless Steel FEMU Validation (Test #3)

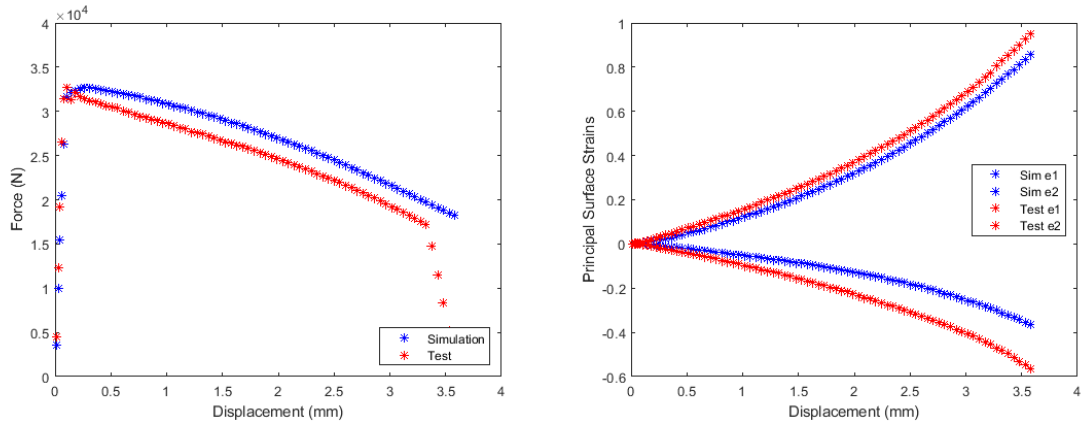

Figure 48: 17-4 PH Stainless Steel FEMU Validation (Test #4)

Table 14: 17-4 PH Stainless Steel FEMU Validation Normalized Mean Square Error Comparison

Test	Force	e1	e2
17-4 PH Stainless Steel Test #1	3.10e-06	3.79e-07	3.69e-05
17-4 PH Stainless Steel Test #2	3.71e-06	2.17e-05	8.79e-05
17-4 PH Stainless Steel Test #3	4.62e-06	3.65e-05	1.17e-04
17-4 PH Stainless Steel Test #4	4.25e-06	3.63e-06	4.28e-05

2.5.3.2 Linear Interpolation

The non-iterative post-necking correction based on linear interpolation between necking and fracture described Sec. 2.3.4 is employed for 17-4 PH Stainless Steel Test #5 (Figure 49). Agreement between simulations and experiment for Test #5 (Figure 49) is reasonable. Following, the Test #5 input curve was used in the simulations of 17-4 PH stainless steel Tests #1-#4 (Figure 50-Figure 53). As a result, a normalized mean square error comparison (cf. Table 13, Table 14, and Table 15) shows that linear interpolation is roughly on the same magnitude as our FEMU approach in predicting principal surface strains, but slightly underperforms at predicting force. This rough agreement is particularly impressive given the simplicity of generating a linear hardening curve between necking and fracture, and that no iteration is required among trial curves (or, more generally, post-necking hardening exponents n) to converge to the "optimal" material response.

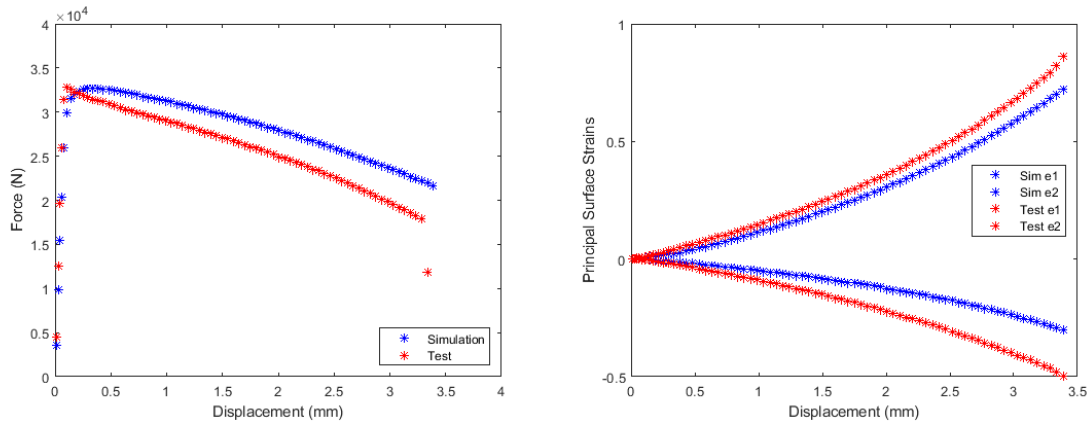

Figure 49: 17-4 PH Stainless Steel Linear Interpolation (Test #5)

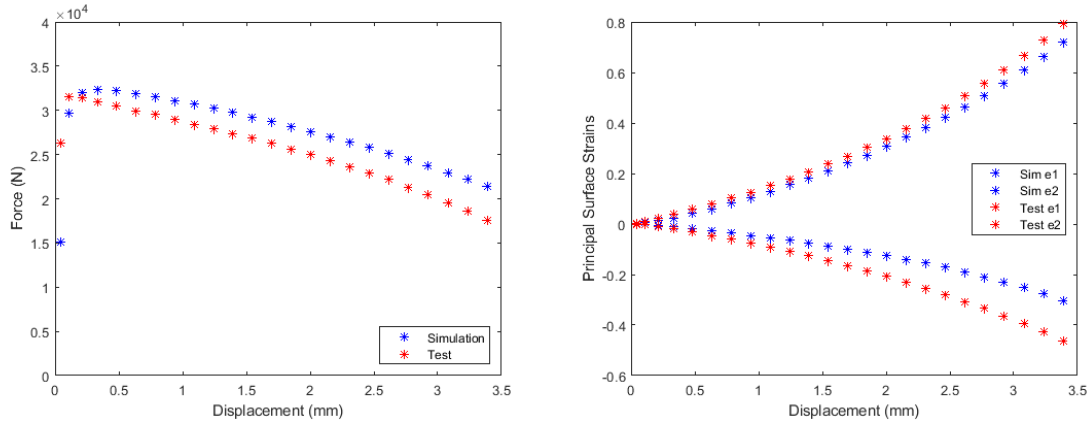

Figure 50: 17-4 PH Stainless Steel Linear Interpolation (Test #1)

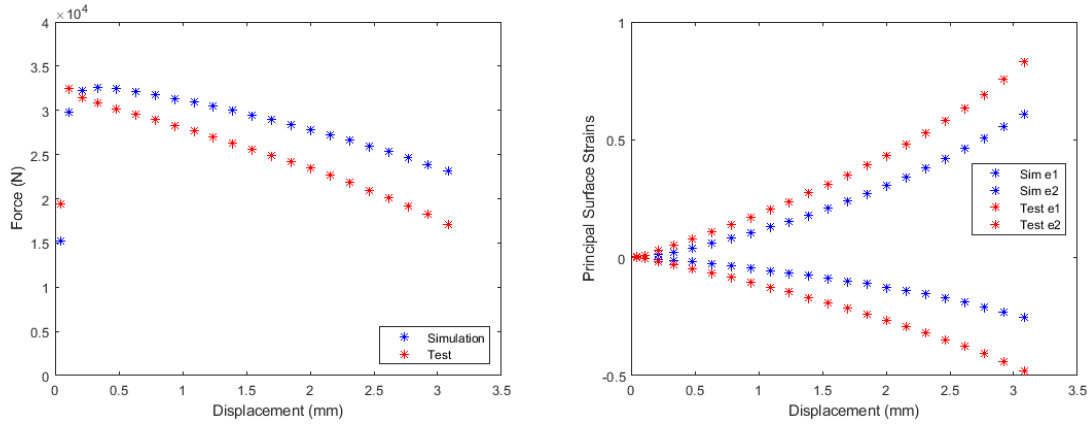

Figure 51: 17-4 PH Stainless Steel Linear Interpolation (Test #2)

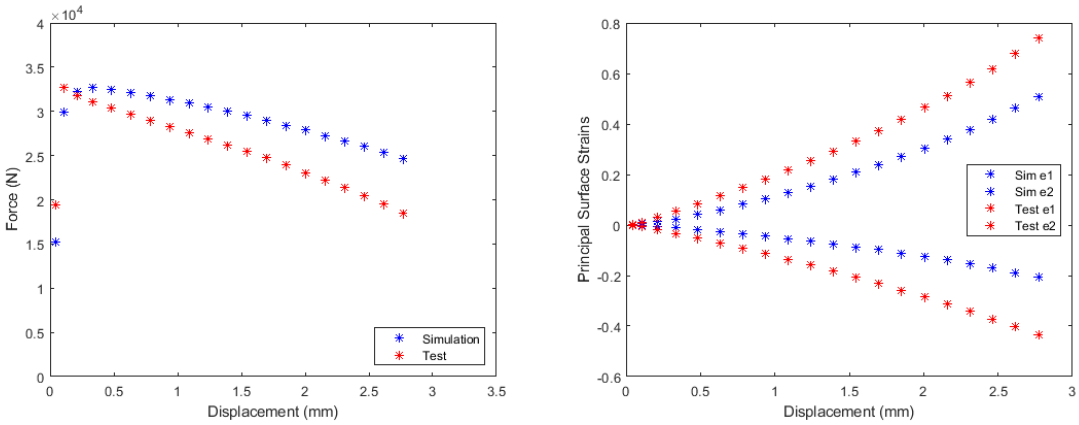

Figure 52: 17-4 PH Stainless Steel Linear Interpolation (Test #3)

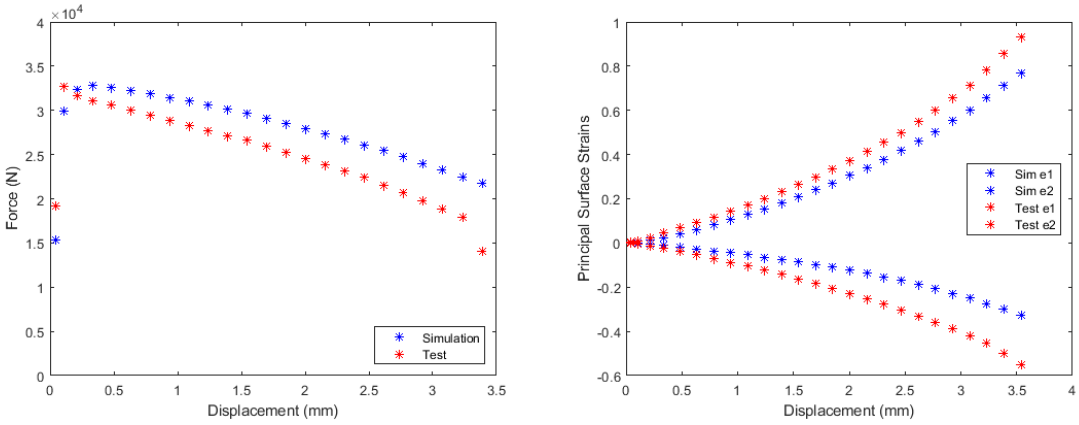

Figure 53: 17-4 PH Stainless Steel Linear Interpolation (Test #4)

Table 15: 17-4 PH Stainless Steel Linear Interpolation Normalized Mean Square Error Comparison

Test	Force	e1	e2
17-4 PH Stainless Steel Test #5	4.70e-06	6.81e-06	5.41e-05
17-4 PH Stainless Steel Test #1	3.03e-05	2.41e-05	3.86e-04
17-4 PH Stainless Steel Test #2	5.32e-05	2.60e-04	8.27e-04
17-4 PH Stainless Steel Test #3	6.27e-05	4.47e-04	0.0012
17-4 PH Stainless Steel Test #4	6.21e-05	7.59e-05	4.52e-04

2.5.4 Ti-6Al-4V Titanium Alloy

2.5.4.1 Iterative Approach

The "fan" of trial post-necking equivalent true stress-strain curves for Ti-6Al-4V Test #2 (Figure 15) was used as the basis for an iterative FEMU approach (Sec. 2.3.3). In our implementation, a cost function (with a specified convergence criterion or termination threshold) exploring the full (continuous) parameter range of the post-necking hardening exponent n (between perfect plasticity and upper bound) was not employed. Rather, the (discrete) trial curve from Figure 15 that produces the lowest normalized mean squared error between test and experiment was adopted as the "optimal" equivalent true stress-strain curve.

The first guess (upper bound with a post-necking hardening exponent $n = 0.0815$) simulation agrees well with the experiment for the force vs. displacement results (Figure 54), but exhibits only fair agreement after necking for the principal strain vs. displacement results.

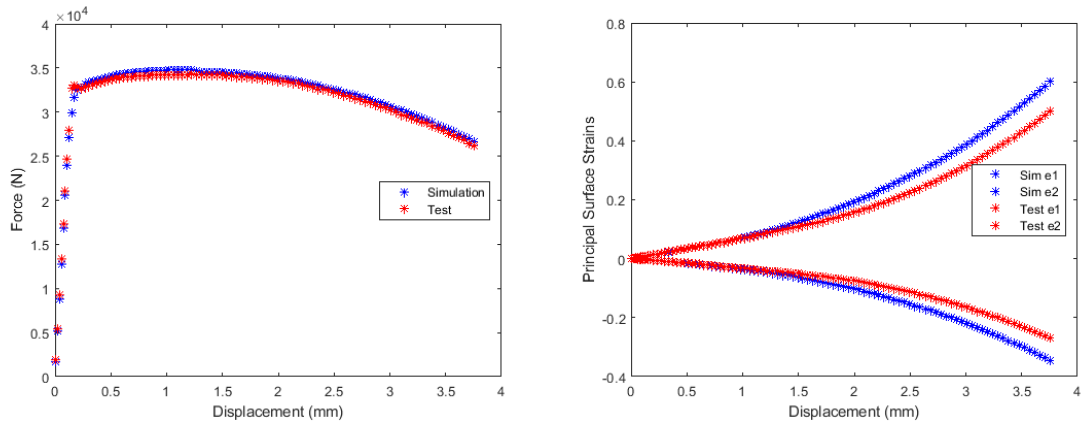

Figure 54: Ti-6Al-4V FEMU First Guess (Test #2)

A second guess (first interior curve in Figure 15 with a lower post-necking hardening exponent $n = 0.0422$) was then taken from the "fan" of prospective curves. The second guess results in worse agreement between simulation and experiment (Figure 55), with an increase in normalized mean square error for all comparison metrics (Table 16). Therefore, the equivalent true stress-strain curve corresponding to Test #2, Guess #1 was selected as our "optimal" candidate.

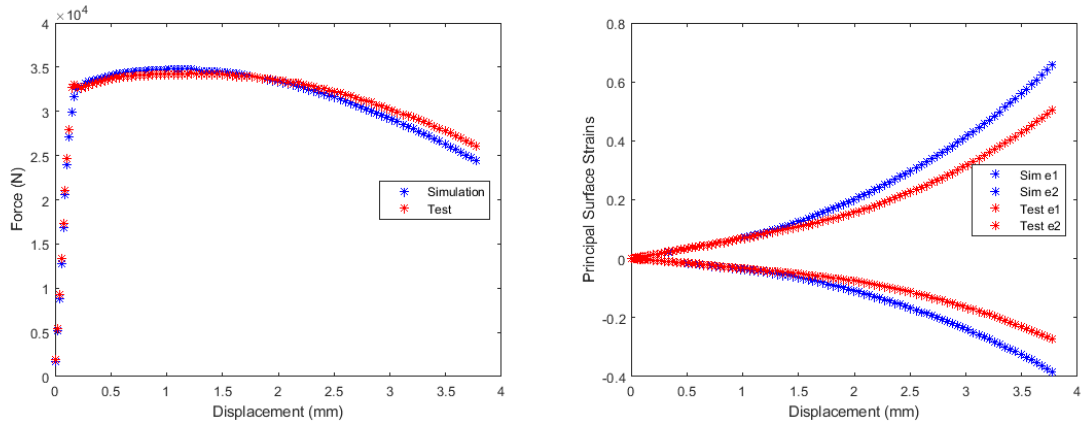

Figure 55: Ti-6Al-4V FEMU Second Guess (Test #2)

Table 16: Ti-6Al-4V Test #2 Normalized Mean Square Error Comparison

Test	Force	e1	e2
Ti-6Al-4V Test #2 1st Guess	3.17e-08	9.56e-06	2.08e-05
Ti-6Al-4V Test #2 2nd Guess	7.92e-08	1.81e-05	3.88e-05

Next, for validation purposes, the true stress-strain behavior from Test #2, Guess #1 was used to simulate the remaining four experiments in the Ti-6Al-4V tensile test series. Very good agreement is observed in force vs. displacement between simulation and experiment. However, the principal strain vs. displacement results exhibit only fair agreement in all validation tests (Figure 56 through Figure 59), corroborated by the error metrics in Table 17.

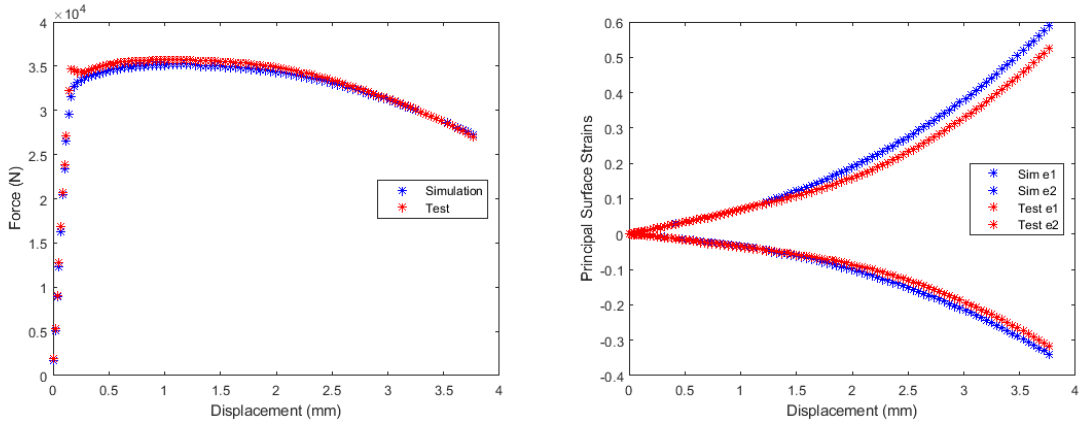

Figure 56: Ti-6Al-4V FEMU Validation (Test #1)

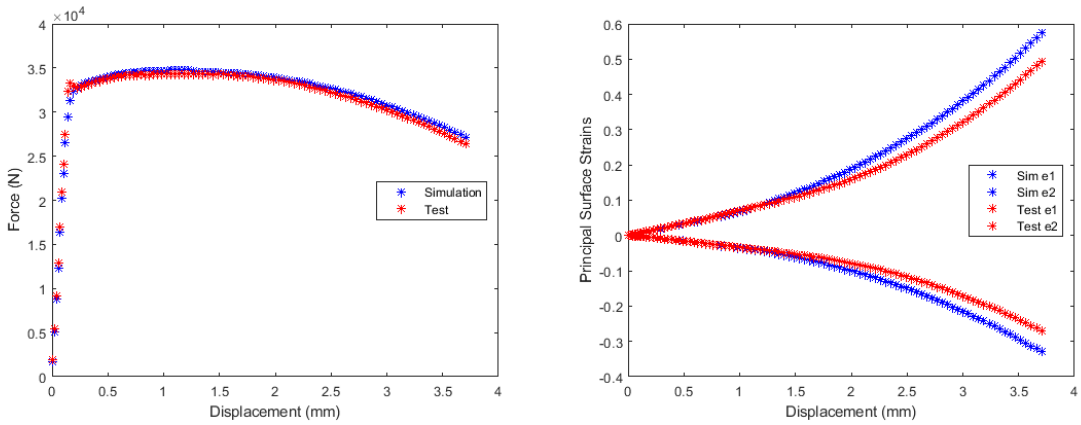

Figure 57: Ti-6Al-4V FEMU Validation (Test #3)

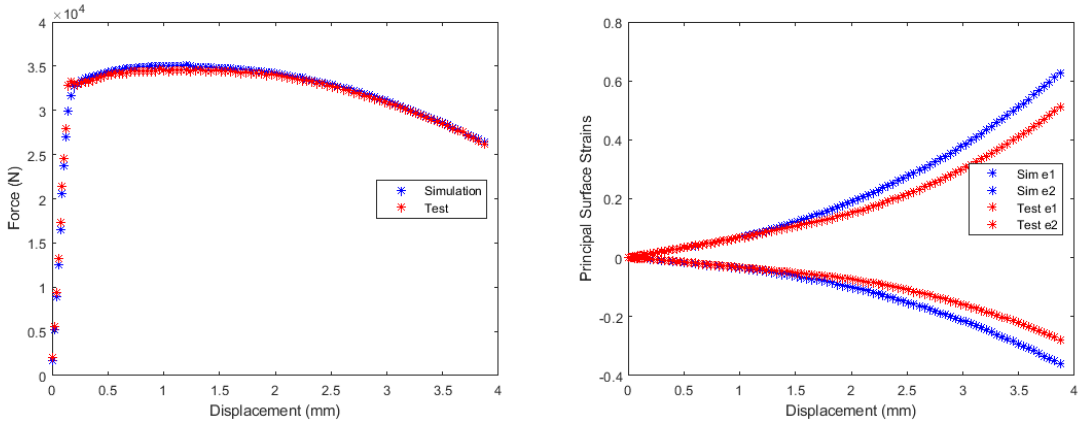

Figure 58: Ti-6Al-4V FEMU Validation (Test #4)

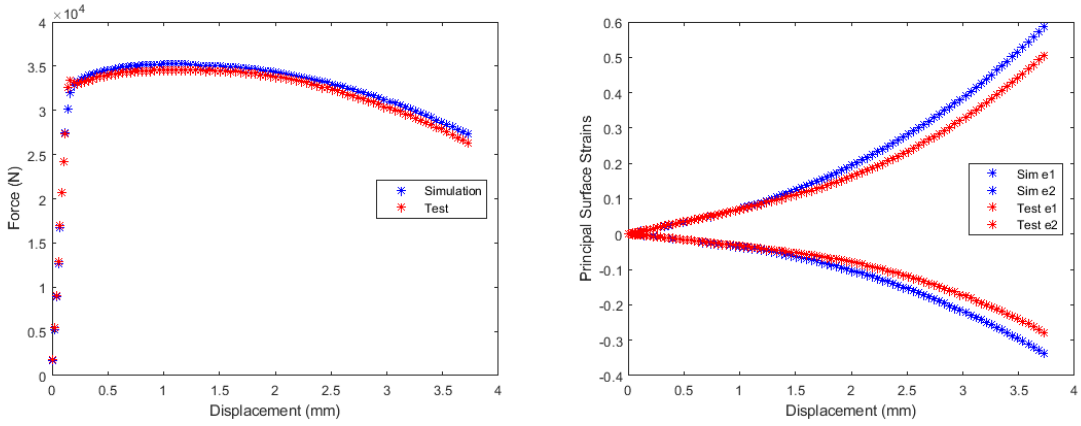

Figure 59: Ti-6Al-4V FEMU Validation (Test #5)

Table 17: Ti-6Al-4V FEMU Validation Normalized Mean Square Error Comparison

Test	Force	e1	e2
Ti-6Al-4V Test #1	4.53e-08	4.25e-06	2.35e-06
Ti-6Al-4V Test #3	3.86e-08	6.17e-06	1.29e-05
Ti-6Al-4V Test #4	2.70e-08	1.14e-05	2.21e-05
Ti-6Al-4V Test #5	5.13e-08	6.20e-06	1.33e-05

2.5.4.2 Linear Interpolation

The non-iterative post-necking correction based on linear interpolation between necking and fracture described Sec. 2.3.4 is employed for Ti-6Al-4V Test #2 (Figure 60). Agreement between simulations and experiment for Test #2 (Figure 60) is excellent for force-displacement and fair for E1/E2-displacement. Following, the Test #1 input curve was used in the simulations of Ti-6Al-4V Test #1 (Figure 61) and Tests #3-#5 (Figure 62-Figure 64). As a result, a normalized mean square error comparison (cf. Table 16, Table 17, and Table 18) shows that linear interpolation is roughly on the same magnitude as our FEMU approach in predicting principal surface strains, but slightly underperforms at predicting force. This agreement is particularly impressive given the simplicity of generating a linear hardening curve between necking and fracture, and that no iteration is required among trial curves (or, more generally, post-necking hardening exponents n) to converge to the "optimal" material response.

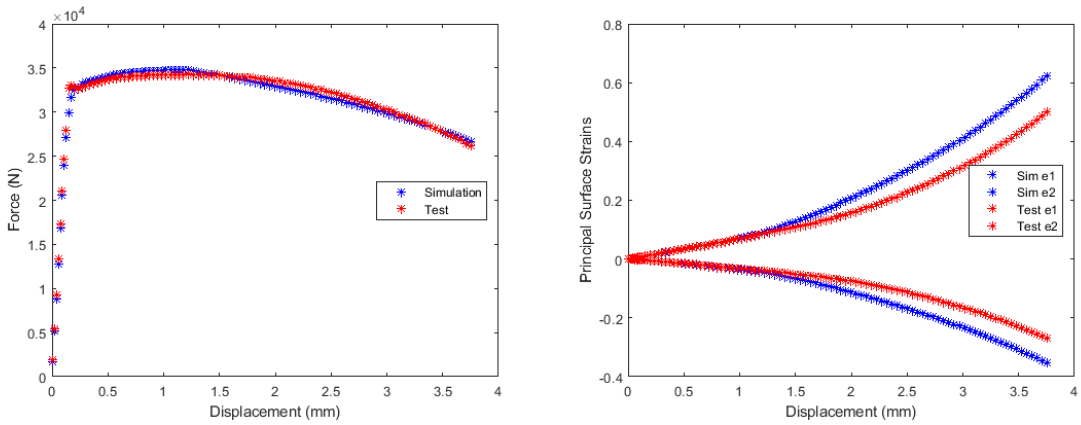

Figure 60: Ti-6Al-4V Linear Interpolation (Test #2)

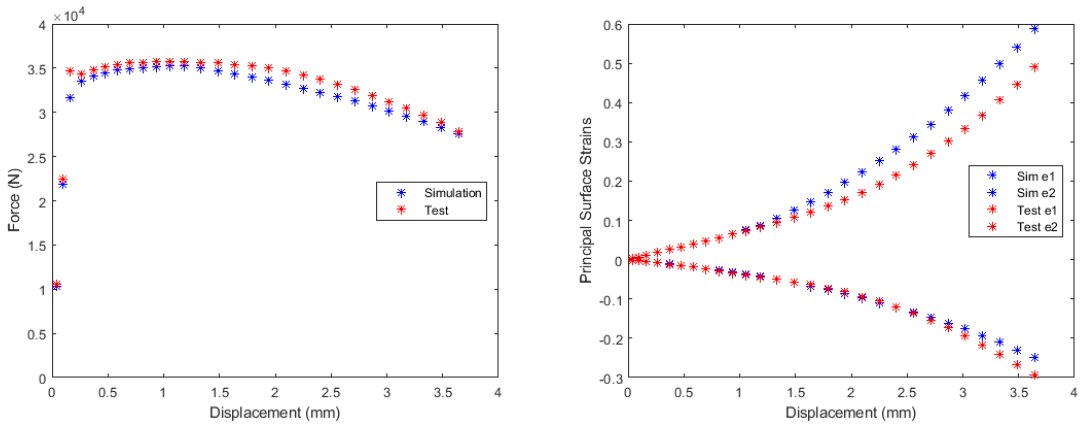

Figure 61: Ti-6Al-4V Linear Interpolation (Test #1)

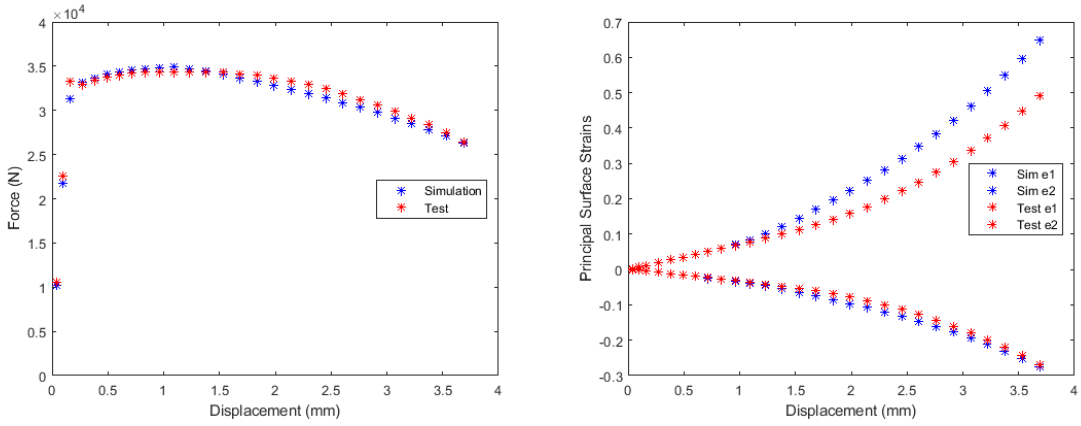

Figure 62: Ti-6Al-4V Linear Interpolation (Test #3)

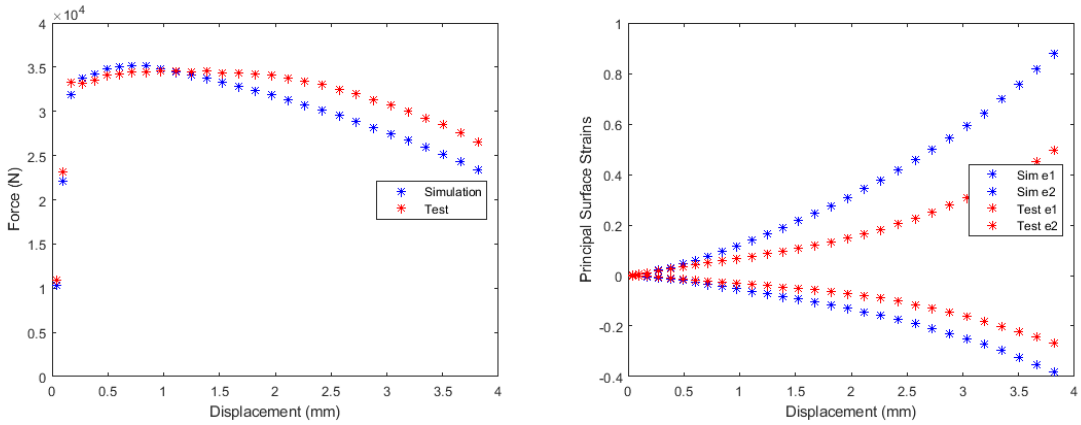

Figure 63: Ti-6Al-4V Linear Interpolation (Test #4)

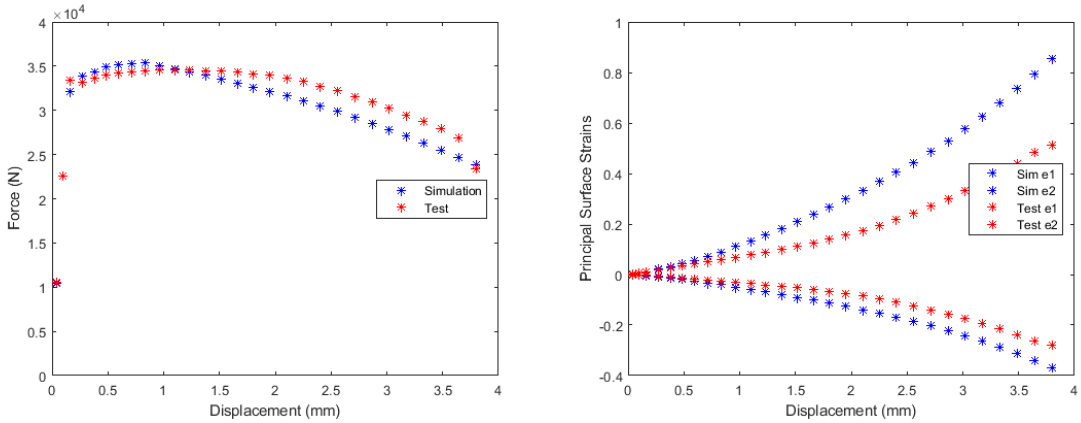

Figure 64: Ti-6Al-4V Linear Interpolation (Test #5)

Table 18: Ti-6Al-4V Linear Interpolation Normalized Mean Square Error Comparison

Test	Force	e1	e2
Ti-6Al-4 Test #2	3.67e-08	1.60e-05	3.13e-05
Ti-6Al-4 Test #1	1.47e-06	1.28e-04	3.07e-05
Ti-6Al-4 Test #3	6.65e-07	2.85e-04	2.58e-05
Ti-6Al-4 Test #4	5.48e-06	0.0016	6.26e-04
Ti-6Al-4 Test #5	3.10e-06	0.0011	3.39e-04

CHAPTER III

LARGE-STRAIN PLASTICITY EXPERIMENTAL PROGRAM AND NUMERICAL SIMULATIONS

3.1 Background

There is a need for experimental data that characterizes the large-strain plasticity of laser powder bed fusion (LPBF) additively manufactured (AM) Ti-6Al-4V across varying stress states, strain rates, temperatures, and build orientations. Although studies exploring build orientation are plentiful (as summarized, for instance, in the recent review by Beese et al. [26]), few have coupled build orientation effects with stress state, strain rate, and/or temperature sensitivity. A notable exception is the work of Wilson-Heid and Beese [30], which investigated the stress-state-dependent plastic deformation of LPBF AM Ti-6Al-4V manufactured in two different build orientations. Mechanical tests under several different stress states (uniaxial tension, plane strain tension, pure shear, and combined tension-shear) were performed. The resulting test data was found to be stress state dependent and slightly anisotropic. A Hill 1948 anisotropic yield criterion was calibrated to the test data, and the calibrated constitutive model performed well in validation experiments.

In this chapter, an experimental program is executed that quantifies the plastic deformation of LPBF AM Ti-6Al-4V over a range of strain rates and build orientations not yet simultaneously investigated in the literature. The significance of strain rate and build orientation on mechanical properties and post-yield hardening behavior are assessed. Equivalent true stress-strain hardening behavior for LPBF AM Ti-6Al-4V is determined using an efficient, novel post-necking correction method developed and validated in Chapter 2 of this thesis. The coupon-level mechanical test data for LPBF AM Ti-6Al-4V presented in this chapter can provide insight on how these metals plastically deform and undergo ductile fracture, as well as inform predictive

computational models that aim to qualify load-bearing AM aircraft components through simulations rather than full-scale physical tests.

3.2 Experiments

The plastic deformation experimental program for LPBF AM Ti-6Al-4V performed in this chapter is outlined in Table 19. It represents a two-factor design of experiments. The first factor, build orientation, has three levels: vertical (longitudinal axis of specimen aligned with build direction), horizontal (longitudinal axis of specimen orthogonal to build direction, and diagonal (longitudinal axis of specimen rotated 45 degrees out of the plane of the build platform). The second factor, strain rate, has two levels: 1E-04 1/s and 1E-02 1/s. All experiments are uniaxial tension tests conducted at room temperature (RT). Five tests are run for each permutation.

Table 19: LPBF AM Ti-6Al-4V Plastic Deformation Test Series

Test Case	Stress State	Strain Rate (1/s)	Orientation	Temp.	Repeats
1	Uniaxial Tension	1E-04	Vertical	RT	5
2	Uniaxial Tension	1E-04	Diagonal	RT	5
3	Uniaxial Tension	1E-04	Horizontal	RT	5
4	Uniaxial Tension	1E-02	Vertical	RT	5
5	Uniaxial Tension	1E-02	Diagonal	RT	5
6	Uniaxial Tension	1E-02	Horizontal	RT	5

3.2.1 Material and Specimen Preparation

Grade 5 Ti-6Al-4V powder (AP&C Powder Metallurgy) conforming to ASTM F2924 [25] with less than ten reuse cycles was used for all specimen builds. The vendor-reported chemical composition of the powder is shown in Table 20.

Table 20: Vendor-Reported Ti-6Al-4V Powder Composition (in wt. %)

Al	V	O	Fe	C	N	H	Y	Other	Ti
6.39	3.85	0.19	0.18	0.02	0.01	0.002	< 0.001	< 0.4	Balance

The vendor-reported median particle size of 37 μm was vetted against in-house static microscopic image analysis (Morpholgi 4, Malvern Panalytical, UK), with the latter returning a median particle size of 31.72 μm, a difference of about 14%. An EOS M290 LPBF machine with a single ytterbium-fiber laser and tool steel recoater arm was used to build all specimens in an argon gas ambient. LPBF process parameters used during the builds are shown in Table 21.

Table 21: AM Build Parameters

Layer Thickness	30 μm
Laser Speed	1050 mm/s
Laser Power	260 W
Laser Wavelength	1060-1100 nm
Laser Spot Diameter	82 μm
Melt Pool Diameter	110-120 μm
Hatch Spacing	140 μm
Stripe Width	5 mm
Stripe Overlap	None
Stripe Rotation	67°/Layer
Build Platform Temp.	150 °C

The EOS M290 printer used the EOS default “striped in-skin with post-contours” scan strategy, where stripes rotate 67 degrees every layer. The individual specimens were built as hexagonal bars along three different orientations – vertical, diagonal or 45-degree, and horizontal – and later machined to their final geometry. The build layout is shown in Figure 65. For vertical and horizontal builds, a small transition layer was placed under the specimens to prevent cracking at the bar/platform interface and facilitate bar separation from the platform. For 45-degree builds, 0.08-in.-thick scaffolds were used to support the bars and transfer heat away to the build platform. Total build time was around 59 hours.

Figure 65: Vertical, Diagonal, and Horizontal AM Ti-6Al-4V Specimens on Build Plate

The first heat treatment (stress relief) was done with the specimens still attached to the build platform in a vacuum furnace (Ipsen USA) at 1202 °F for 3 hours with rapid argon cooling. Specimens were then extracted from the build plate with a band saw. The first heat treatment prevents deformation caused by residual stresses when specimens were removed from the support scaffolding. The second heat treatment (ductility restoration) was done at 1472 °F for 3 hours with rapid argon cooling in the vacuum furnace. After heat treatment, the hex bars were machined on a lathe and ground to the desired nominal dimensions (Figure 66). After machining, the test sections were polished to a target surface roughness of 10 Ra.

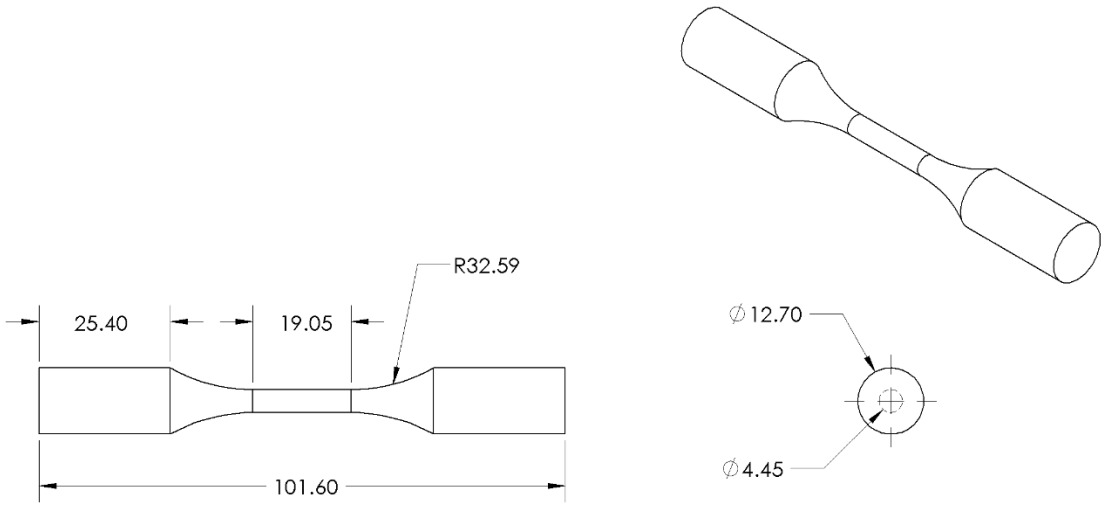

Figure 66: Nominal AM Ti-6Al-4V Plasticity Specimen (Dimensions in mm)

Each specimen's as-built gage dimensions were measured using a non-contact optical 3D measurement system (VR-3000, KEYENCE, Itasca, IL). It is imperative that the modeled specimen have the same gage dimensions as its respective physical specimen for each simulation to match its respective physical tensile test.

To characterize the grain morphology of the as-printed LPBF Ti-6Al-4V, electron backscatter diffraction (EBSD) was performed on a representative specimen from each build orientation (Figure 67). A disk-shaped cross-sectional sample was cut from the specimen gage section and polished to 0.05 micron with colloidal silica on a vibratory polisher. Copper tape was placed on a portion of the specimen to decrease static charge, and silver paste was used to dissipate extra energy from charge buildup. The sample was imaged with an Oxford EBSD camera on an Apreo 2C (Thermo Fisher Scientific) scanning electron microscope (SEM). Data was obtained on the sample's cross-sectional plane at a 70° angle to the electron source, a step size of 0.75 microns, and a 50x magnification using inverse pole figures.

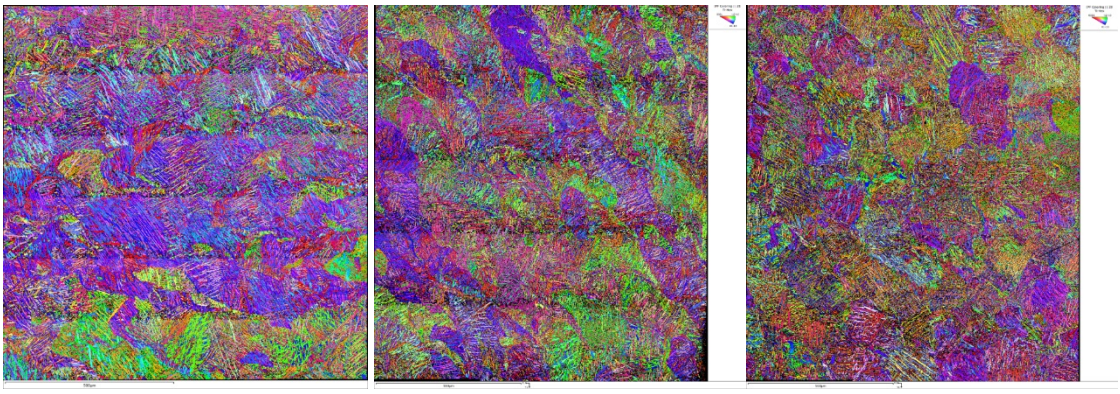

Figure 67: EBSD Maps: Horizontal (Left), Vertical (Middle), Diagonal (Right)

3.2.2 Mechanical Test Setup

A custom-built MTS 858 tabletop servo-hydraulic load frame was used to complete all tensile testing. Two MTS 647 hydraulic wedge grips with 0.5-inch wedges were used to secure about three-quarters of each specimen's shoulder tabs. During testing, an MTS #609 10A-01 load cell measured the force. This data was recorded by the MTS FlexTest60 acquisition system. A clip-on extensometer with an initial separation of 0.577 inch. (14.6558 mm) was placed about the center of the specimen to verify the DIC-based strain measurement. The actuator speed v corresponding to a targeted nominal strain rate $\dot{\varepsilon}$ is calculated using:

$$v = \frac{L_c}{\dot{\varepsilon}} \tag{12}$$

where L_c is the nominal gage length. Actuator speeds for the two nominal strain rates in this experimental program are reported in Table 22 below.

Table 22: Strain Rates and Actuator Speeds

Target Strain Rate (1/s)	Nominal Gage Length (inch)	Actuator Speed (in/s)
1.00E-04	0.75	7.5E-05
1.00E-02	0.75	7.5E-03

Before tensile testing, the load frame was aligned using the MTS 609 alignment fixture. First, a strain-gaged specimen was gripped in the wedge grips of the load frame. The MTS 609 alignment software recorded a three-point bending strain plot in accordance with angularity and concentricity. The “zeroing” of these points, was accomplished by increasing or decreasing the torque in the bolts, eliminating the risk of pre-loading the specimen. A 5% bending range (Class 5 alignment) was considered to be a sufficiently small pre-loading error range.

3.2.3 Digital Image Correlation Setup

All specimens were cleaned with acetone and/or isopropyl alcohol to remove dirt, dust, and other debris. A high-contrast speckle pattern was applied to each test specimen using an airbrush. White paint was uniformly applied to completely cover the specimen’s gage section. After, but before drying, black paint was sprayed from farther back to apply a speckle on top of the white background. All specimens were tested within a few hours of speckling to avoid paint cracking. Additionally, care was taken during mechanical testing to avoid scratching or rubbing off the paint.

A stereo camera setup with two high-performance monochrome cameras (FLIR Grasshopper 3 GS3-U3-89S6M-C) with Schneider XNP Xenoplan compact 50-mm lenses were leveraged to capture sequential images of the motion of the speckle pattern. Three-dimensional digital image correlation (DIC) software (VIC-3D, Correlated Solutions, v.7, Irmo, SC) was used to compute the deformation and strain in the gage section from the series of time-stamped images.

A Gaussian low-pass logarithmic filter was applied to the data when correlating, which averages the strain values at each pixel to reduce noise and present a clear and uniform strain measurement. Data was captured at a frame rate of 0.15 images per second with an F# of 5.6. A virtual extensometer (VE) and virtual strain gage (VSG) were placed on the specimen inside a correlated window of the gage section to calculate the strain in the area of interest (Figure 68).

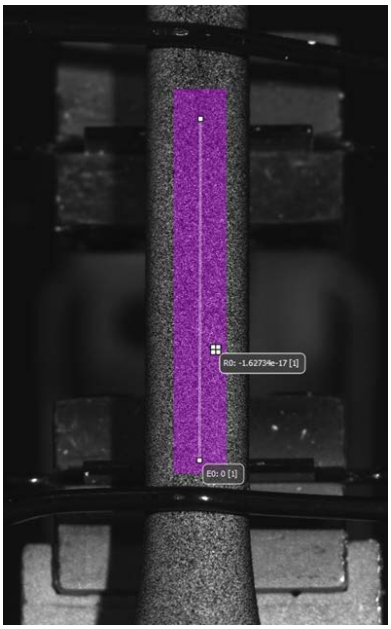

Figure 68: Gripped AM Ti-6Al-4V Specimen with PE, VE, and VSG

The VE was placed to coincide, as much as possible, with the 0.577 inch (14.6558 mm) physical extensometer. The VSG was placed as a 14x14 pixel square region as close as possible to the eventual fracture location. Detailed information on the DIC parameters used in each test can be found in Table 23.

Table 23: AM Ti-6Al-4V DIC Correlation Details

Test	Subset	Step	Filter Size	Pixel/mm	VSG (pixels)	VSG (mm)	VE (mm)
Vertical, 1E-04 Test 1	33	8	23	0.015314	14	0.2144	14.7356
Vertical, 1E-04 Test 2	Test Failed Early During Elastic Regime – Details Not Included						
Vertical, 1E-04 Test 3	27	6	23	0.015314	14	0.2144	14.7158
Vertical, 1E-04 Test 4	33	8	23	0.015314	14	0.2144	14.7083
Vertical, 1E-04 Test 5	31	7	23	0.015314	14	0.2144	14.7192
Diagonal, 1E-04 Test 6	33	8	23	0.015314	14	0.2144	14.7277
Diagonal, 1E-04 Test 7	35	7	23	0.015314	14	0.2144	14.7234
Diagonal, 1E-04 Test 8	35	8	23	0.015314	14	0.2144	14.7174
Diagonal, 1E-04 Test 9	37	9	23	0.015314	14	0.2144	14.7234
Diagonal, 1E-04 Test 10	35	8	23	0.015314	14	0.2144	14.7422
Horizontal, 1E-04 Test 11	35	8	23	0.015314	14	0.2144	14.7219
Horizontal, 1E-04 Test 12	35	8	23	0.015314	14	0.2144	14.7195
Horizontal, 1E-04 Test 13	31	7	23	0.015421	14	0.2159	14.7267
Horizontal, 1E-04 Test 14	31	7	23	0.015421	14	0.2159	14.7235
Horizontal, 1E-04 Test 15	31	7	23	0.015421	14	0.2159	14.7293
Vertical, 1E-02 Test 16	31	7	23	0.015421	14	0.2159	14.7309
Vertical, 1E-02 Test 17	31	7	23	0.015421	14	0.2159	14.7109
Vertical, 1E-02 Test 18	43	10	23	0.015421	14	0.2159	14.7125
Vertical, 1E-02 Test 19	33	8	23	0.015421	14	0.2159	14.7014
Vertical, 1E-02 Test 20	39	9	23	0.015421	14	0.2159	14.7239
Diagonal, 1E-02 Test 21	35	8	23	0.015421	14	0.2159	14.7073
Diagonal, 1E-02 Test 22	33	8	23	0.015421	14	0.2159	14.7117
Diagonal, 1E-02 Test 23	37	9	23	0.015421	14	0.2159	14.7372
Diagonal, 1E-02 Test 24	39	9	23	0.015421	14	0.2159	14.7330
Diagonal, 1E-02 Test 25	39	9	23	0.015421	14	0.2159	14.7395
Horizontal, 1E-02 Test 26	39	9	23	0.015421	14	0.2159	14.7191
Horizontal, 1E-02 Test 27	33	8	23	0.015421	14	0.2159	14.7071
Horizontal, 1E-02 Test 28	33	8	23	0.015421	14	0.2159	14.7401
Horizontal, 1E-02 Test 29	33	8	23	0.015421	14	0.2159	14.7263
Horizontal, 1E-02 Test 30	33	8	23	0.015421	14	0.2159	14.7225

3.3 Finite Element Simulations

3.3.1 Overview of Post-Necking Correction Approach

The novel, iterative post-necking correction method discussed in Section 2.3.2 was leveraged during this test series to help generate equivalent true stress-strain curves for each parameter case (build orientation & strain rate). The local Hencky strain is calculated throughout the test with the help of DIC. By placing a VSG at the site of eventual fracture, the longitudinal

(E1) and transverse (E2) principal surface strain components can be measured at each time step of the test. Assuming incompressibility, E3 and eventually a three-dimensional equivalent strain can be calculated. From there, an adjusted true stress is calculated, and the resultant true stress-strain curve serves as a first guess (upper bound) input curve. Necking is identified at the intersection of the adjusted true stress-strain curve and its slope.

A prospective fan of extrapolated curves is then created using the first guess as the upper bound and altering the strain hardening exponent down towards zero (perfect plasticity). This fan was created using a logarithmically spaced vector of varying hardening exponents, and typically contained 5 or 6 prospective curves. Fans for each test case are shown below in (Figure 69). Parallel simulations of the tensile tests are then completed with a first and second guess input curve in an attempt to converge to matching behavior between test and simulation.

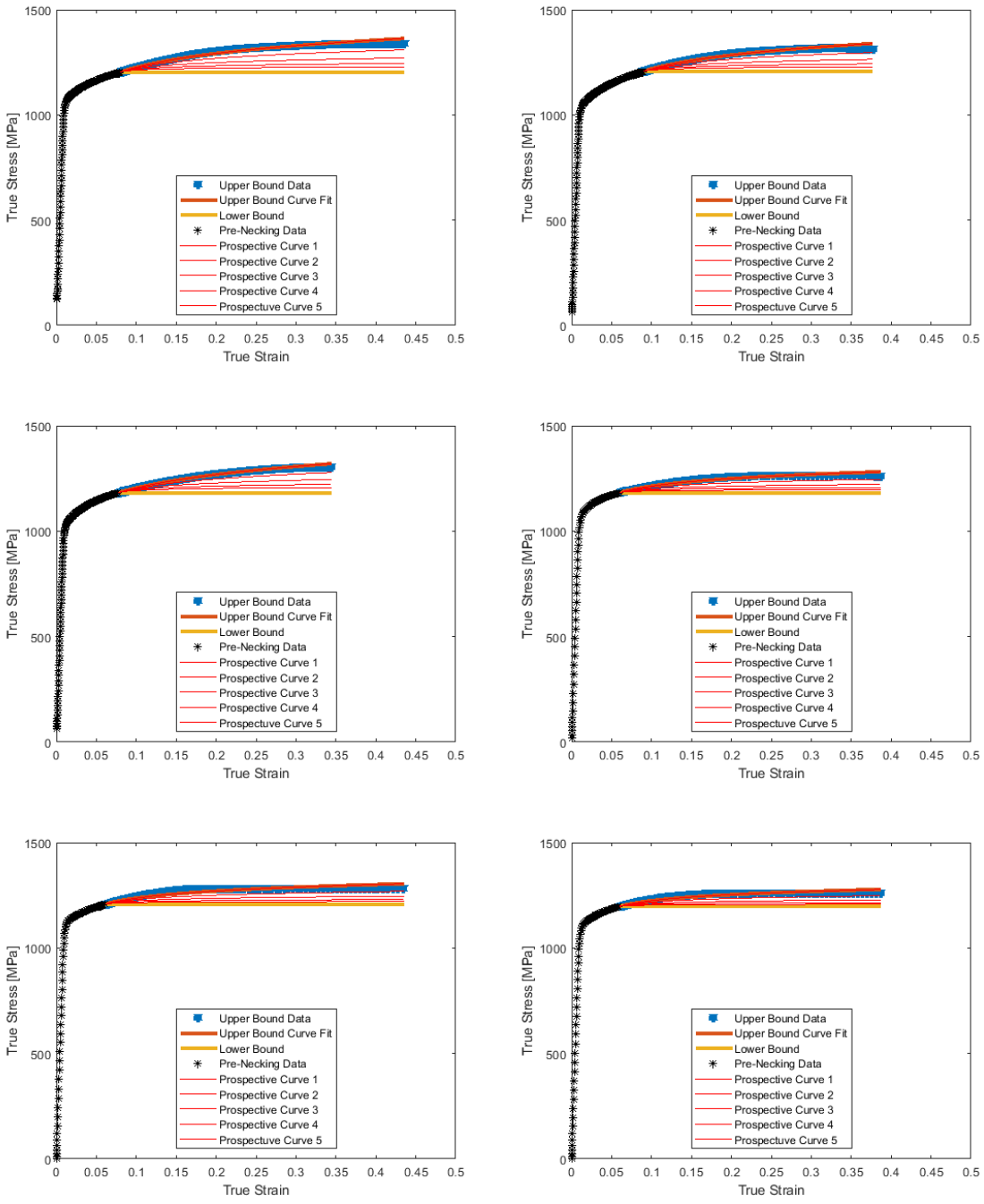

Figure 69: Prospective Fans for: Vertical, 1E-04 /s (Top Left), Diagonal, 1E-04 /s (Top Right), Horizontal, 1E-04 /s (Middle Left), Vertical, 1E-02 /s (Middle Right), Diagonal, 1E-02 /s (Bottom Left), Horizontal, 1E-04 /s (Bottom Right)

3.3.2 Solid Modeling and Meshing

SolidWorks (DASSAULT SYSTEMES, 2019-2020 Student Edition, Waltham MA) computer-aided design (CAD) software was used to create a 3D solid model of each specimen in the test series. It is important to model each test specimen to its exact, as-built/as-machined dimensions (not the nominal dimensions in Figure 66) to best match the simulation to its respective test. Each 3D solid model was then imported as an IGES file into HyperMesh (HyperWorks, v. 2019.1, Altair, Troy, MI) for discretization through finite element meshing (Figure 70).

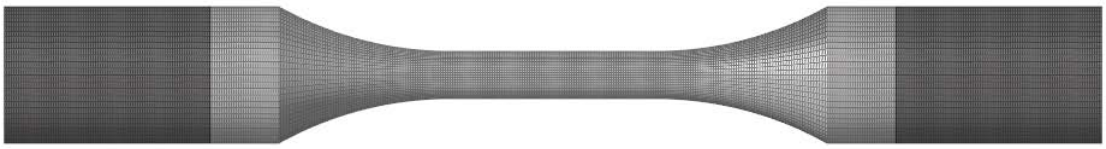

Figure 70: Nominal Mesh for AM Ti-6Al-V4 Test Series

A characteristic element size for the mesh of each test specimen was selected to match the VSG size used for digital image correlation measurements (Table 23). Each specimen contained about 275,000 elements. The typical element density in the specimen gage was about 24 elements across its diameter.

3.3.3 Finite Element Modeling and Simulation Details

Numerical simulations were performed using an explicit solver in the commercial finite-element code LS-DYNA® (version R10.1.0, Ansys/LST, Livermore, CA). Three-dimensional, constant-stress, 8-node, solid hex elements (ELFORM = 1) were used in the simulations. To account for the tendency of under-integrated elements to hourglass, stiffness-based hourglass

control (IHQ = 6) was employed with an hourglass coefficient QH = 0.1. Hourglass energies imposed by the hourglass control algorithm were found to be acceptably low in all simulations.

The specimen grip sections (denoted by dark gray shading in Figure 70) were assumed to constitute approximately 75% of the shoulders, consistent with the experiments. One of the grip sections was held fixed (with all translational and rotational degrees of freedom constrained), while the other was prescribed an "artificial" constant velocity of 1 m/s. This "artificial" actuation speed is sufficiently high to meaningfully reduce the computational cost of explicitly simulating a quasi-static test, but sufficiently low to not introduce inertial effects, often observed as transient oscillations in material response (e.g., force vs. displacement) near simulation startup. Additionally, a small ratio between kinetic energy and initial energy point to lowered dynamic effects, which was the case across the simulations enclosed in this work. A rigid material model (*MAT_020) was assigned to both grip sections. The motion of the rigid gripped sections of the specimen was restricted using a center of mass constraint (CMO = 1) in *MAT_20. For the fixed grip section, the following constraint parameters were set to CON1 = CON2 = 7 to constrain all translational and rotational degrees of freedom. The gripped section driven by the uniaxial actuator was constrained using CON1 = 5, CON2 = 7 so that only axial translation was permitted. The ungripped section of the specimen (denoted by light gray shading in Figure 70) was modeled using the *MAT_024 material card. This elasto-plastic constitutive model requests as input density (Table 24), linear elastic material parameters (modulus of elasticity and Poisson's ratio (Table 24)), as well as post-yield equivalent true stress-strain curve. Running in shared-memory parallel on eight CPUs, the simulations took anywhere from 8-12 hours, depending mostly on the ductility of each Ti-6Al-4V specimen's behavior. Because the same velocity was used across all simulations, a larger ductility (failure strain) required a longer simulation termination time, which directly relates to computational expense.

Table 24: LPBF Ti-6Al-4V Elastic Material Properties for MAT_024 Input

Parameter Case	Density (tonne/mm^3)	Elastic Modulus (GPa)	Poisson's ratio
Vertical, 1E-04 /s	4.43e-09	113	0.35
Diagonal, 1E-04 /s	4.43e-09	110	0.35
Horizontal, 1E-04 /s	4.43e-09	110	0.35
Vertical, 1E-02 /s	4.43e-09	116	0.35
Diagonal, 1E-02 /s	4.43e-09	113	0.35
Horizontal, 1E-02 /s	4.43e-09	111	0.35

3.4 Results

Material properties (mean ± one standard deviation) for each of the four metal alloys are reported in Table 25. The elastic modulus was obtained through a linear regression of the pre-yield, linear elastic portion of the stress-strain curve. The yield point was taken to coincide with the proportional limit, i.e., the transition from linear to nonlinear true stress-strain response. The ultimate tensile strength (UTS) was obtained as the absolute maximum of the post-yield true stress-strain curve. The failure strain is the true strain reported by the DIC VSG at specimen fracture, defined here as initial material separation in the specimen gage section. Considerable difference in calculated elastic modulus values and values reported in literature can be explained by the low data density at small strains in DIC strain measurement. In order to fully capture an accurate elastic modulus, a higher frame rate and smaller filter would be required.

Table 25: AM Ti-6Al-4V Material Properties (Mean +/- Standard Deviation)

	Elastic Modulus (GPa)	Yield Strength (MPa)	UTS (MPa)	Failure Strain
Vertical, 1.00E-04 /s	106.6 ± 1.802	939.5 ± 56.61	1325 ± 30.61	0.4321 ± 0.0213
Diagonal, 1.00E-04 /s	109.8 ± 2.753	943.2 ± 11.11	1322 ± 8.330	0.3753 ± 0.0293
Horizontal, 1.00E-04 /s	105.7 ± 5.509	916.6 ± 22.03	1304 ± 3.470	0.3350 ± 0.0146
Vertical, 1.00E-02 /s	109.4 ± 2.341	1004 ± 29.68	1263 ± 12.17	0.4728 ± 0.0504
Diagonal, 1.00E-02 /s	105.7 ± 2.199	1027 ± 6.770	1287 ± 7.660	0.4569 ± 0.0233
Horizontal, 1.00E-02 /s	101.2 ± 4.455	1011 ± 19.20	1253 ± 21.92	0.3922 ± 0.0301

To assess agreement between simulation and experiment, the error in measured quantities – namely axial force vs. axial displacement and principal Hencky surface strains (maximum E1 and minimum E2) vs. displacement – was quantified. Displacement in each test was calculated from the virtual extensometer, and force was obtained from the load cell. Displacement in each simulation was calculated by tracking the axial elongation of two nodes whose initial separation correlates with the virtual extensometer length; force was obtained on a cross-sectional plane placed on the anticipated fracture plane (i.e., the cross-sectional plane containing the most highly strained elements). Principal Hencky surface strain histories in the tests were measured using a DIC virtual strain gage placed at the failure location. Principal surface strain histories in the simulations were obtained from a representative surface element on the anticipated fracture plane. Because the simulation is symmetric, any element on either side of the anticipated fracture plane will report the same surface strain values. The error between simulation and experiment was quantified for each metric (force vs. displacement and principal surface strains vs. displacement) using the normalized mean squared error function found in Eq. (10) with the mean squared error given by Eq. (11).

In addition to the force vs. displacement and principal surface strains vs. displacement plots, a qualitative comparison was done by juxtaposing the final frame from DIC with a frame in the simulation with the corresponding displacement. The final pictures display maximum principal surface strain contours spatially plotted on the specimen/mesh. Care was taken to match the fringe range (maximum, minimum, and number of color tiles) between both the simulation and test to ensure honest comparison.

3.4.1 Vertical, 1E-04 /s

3.4.1.1 Iterative Simulations for Material Card Generation

The "fan" of trial post-necking equivalent true stress-strain curves for the first of six parameter cases (vertical, 1E-04 /s) Test #1 (Figure 69) was used as the basis for an iterative FEMU approach (Sec. 2.3.3). In the implementation, a cost function (with a specified convergence criterion or termination threshold) exploring the full (continuous) parameter range of the post-necking hardening exponent n (between perfect plasticity and upper bound) was not employed. Rather, the (discrete) trial curve from Figure 69 that produces the lowest normalized mean squared error between test and experiment was adopted as the "optimal" equivalent true stress-strain curve.

The first guess (upper bound with a post-necking hardening exponent $n = 0.0646$) simulation agrees well with the experiment until larger strains (Figure 71), where the force vs. displacement and principal strain vs. displacement results diverge.

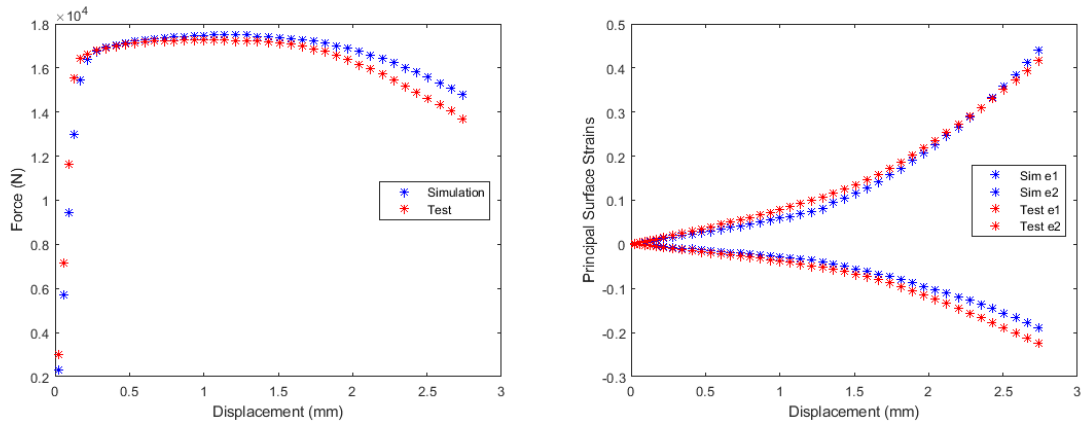

Figure 71: Vertical, 1E-04 /s Test #1 First Guess Simulation vs. Test

In particular, the simulation over-predicts the amount of force needed to displace the material, indicating that the first guess is too stiff. Thus, a second guess (first interior curve in Figure 69 with a lower post-necking hardening exponent n =0.0334) was taken from the "fan" of prospective curves. The second guess results in excellent agreement for force vs. displacement between simulation and experiment (Figure 72), with a reduction in normalized mean square error (Table 26), and the principal surface strain agreement is on the same magnitude. Therefore, the equivalent true stress-strain curve corresponding to Test #1, Guess #2 (Figure 73) was selected as our "optimal" candidate.

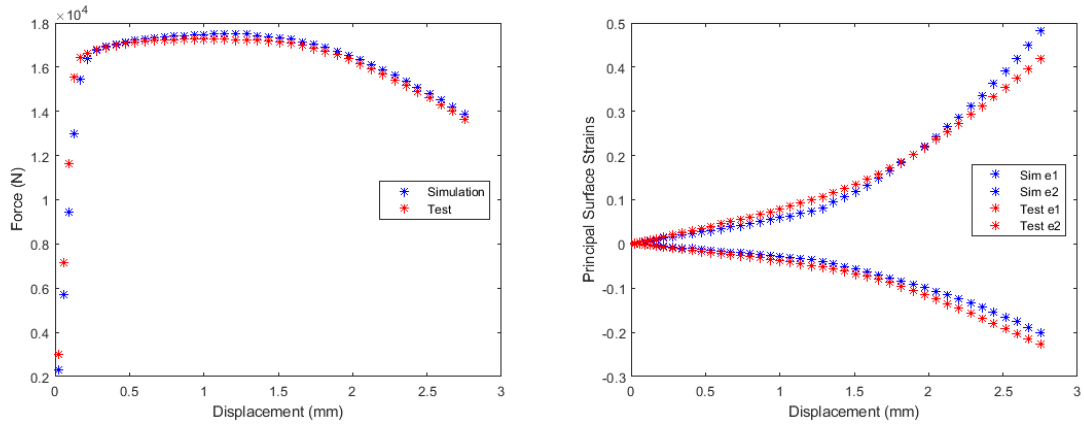

Figure 72: Vertical, 1E-04 /s Test #1 Second Guess Simulation vs. Test

Table 26: Vertical, 1E-04 /s Test #1 Normalized Mean Square Error Comparison

Test	Force-Displacement	e1-Displacement	e2-Displacement
Test #1 1st Guess	1.40e-06	5.74e-06	3.44e-05
Test #1 2nd Guess	9.45e-07	1.31e-05	2.17e-05

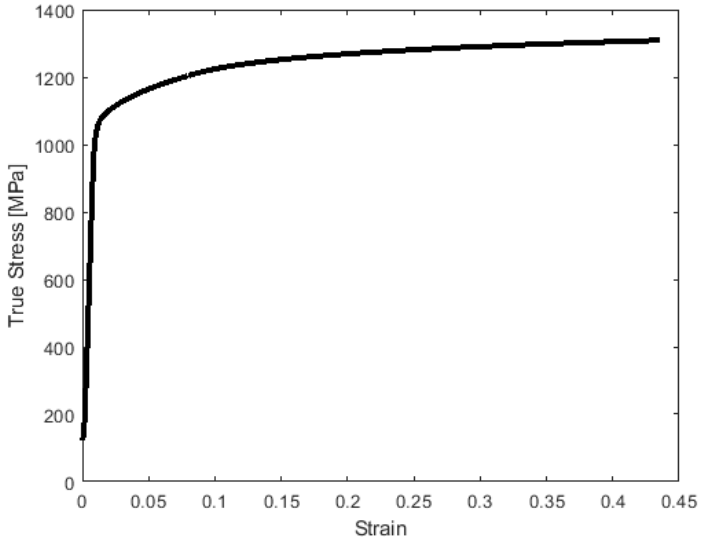

Figure 73: Vertical, 1E-04 /s Test #1 True Stress-Strain Input Curve

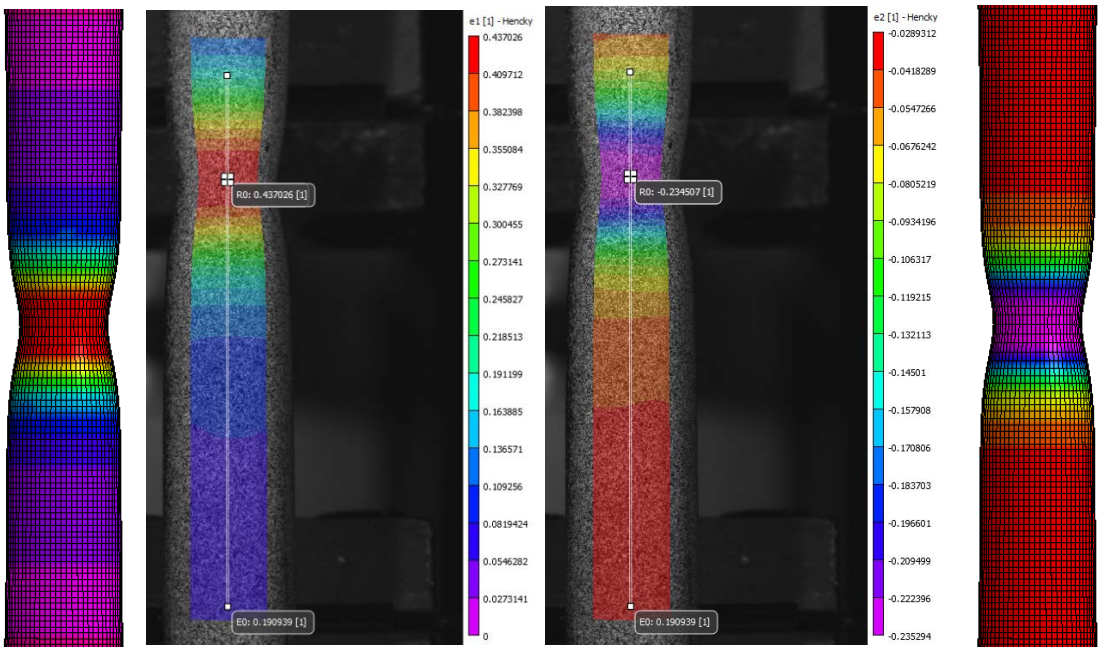

Figure 74: Vertical, 1E-04 /s Test #1 Second Guess Principal Strain Comparison

3.4.1.2 Validation Simulations

Next, for validation purposes, the true stress-strain behavior from Test #1, Guess #2 was used to simulate the remaining three experiments in the vertical, 1E-04 /s tensile test series (test two failed prior to yield). Good agreement is seen between simulation and experiment for Tests #3-#5 (Figure 75-Figure **77**) corroborated by the error metrics in Table 27.

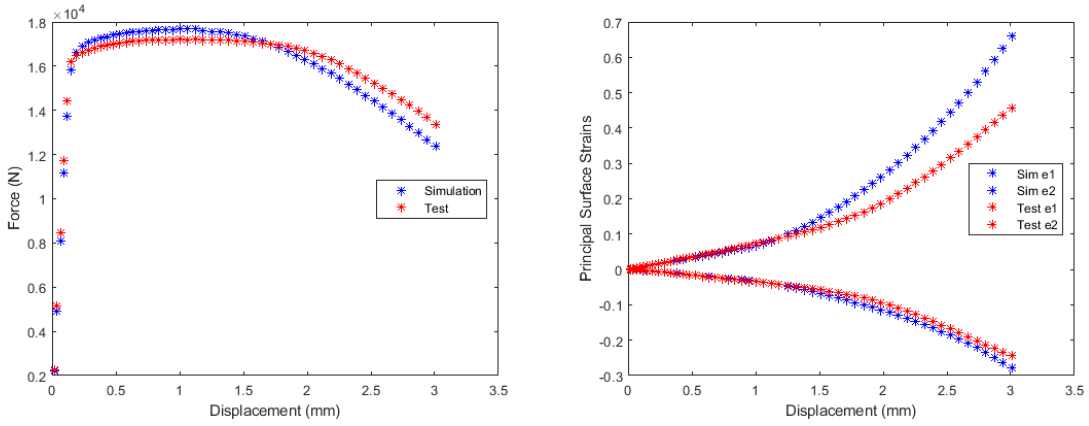

Figure 75: Vertical, 1E-04 /s Test #3 with Test #1 Second Guess Material Card

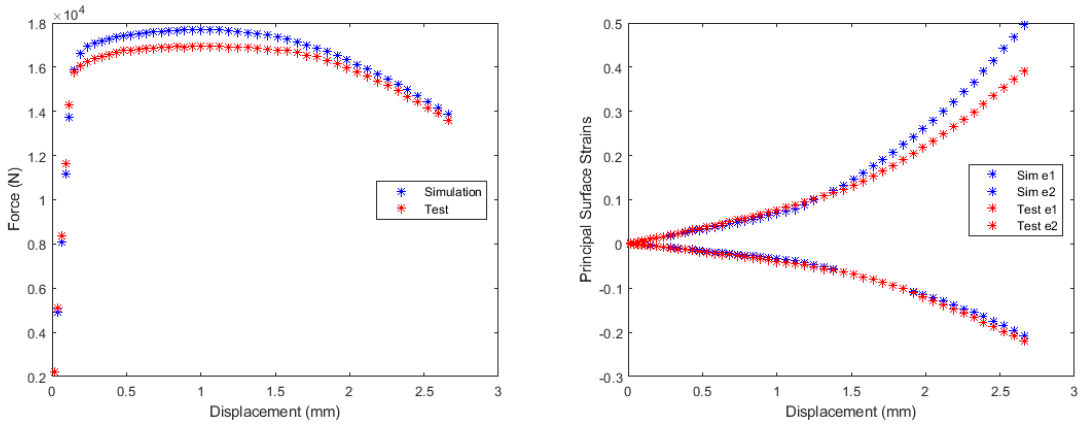

Figure 76: Vertical, 1E-04 /s Test #4 with Test #1 Second Guess Material Card

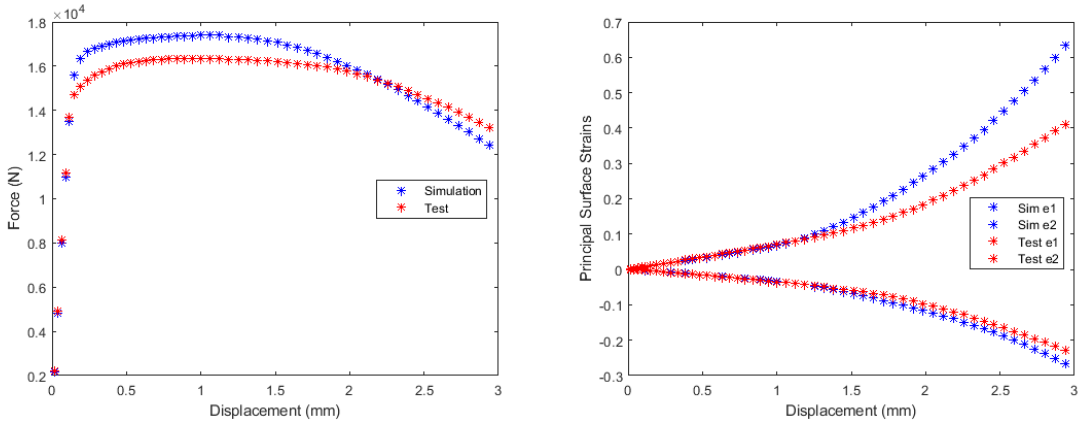

Figure 77: Vertical, 1E-04 / s Test #5 with Test #1 Second Guess Material Card

Table 27: Vertical, 1E-04 /s Validation Simulations Normalized Mean Square Error Comparison

Test	Force-Displacement	e1-Displacement	e2-Displacement
Test #3	4.12e-07	1.07e-04	1.23e-05
Test #4	5.81e-07	3.78e-05	3.42e-06
Test #5	1.09e-06	1.52e-04	1.73e-05

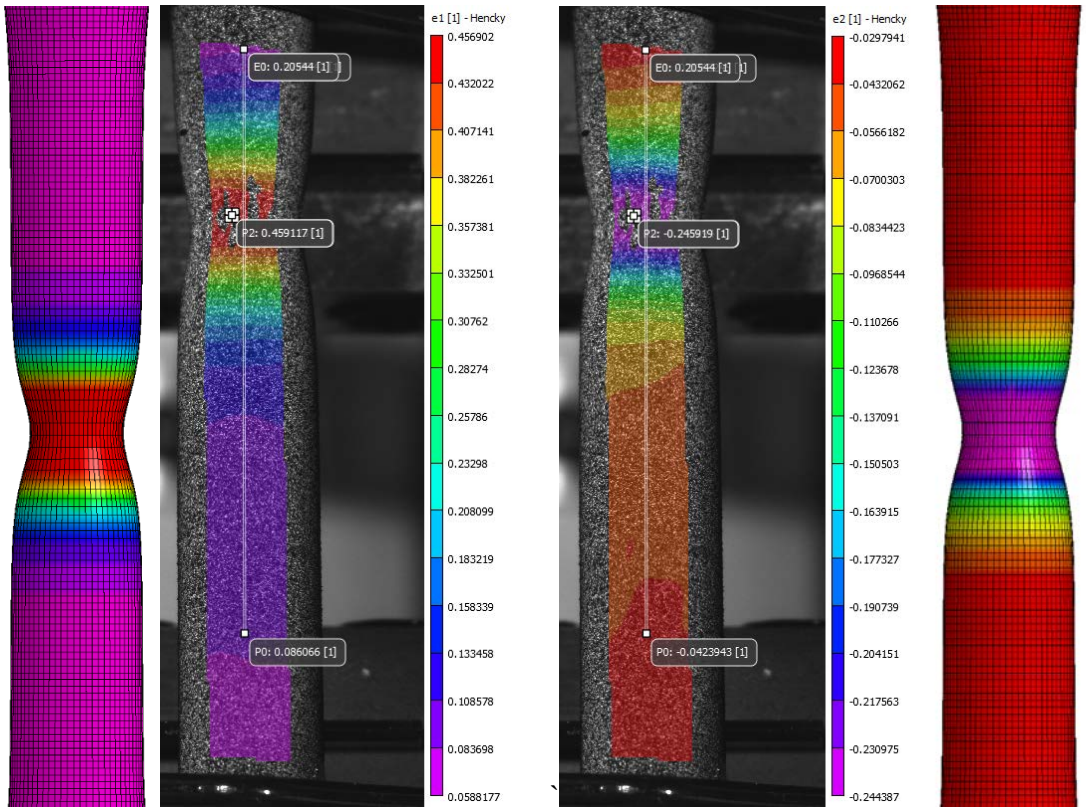

Figure 78: Vertical, 1E-04 /s Test #3 with Test #1 Material Card Principal Strain Comparison

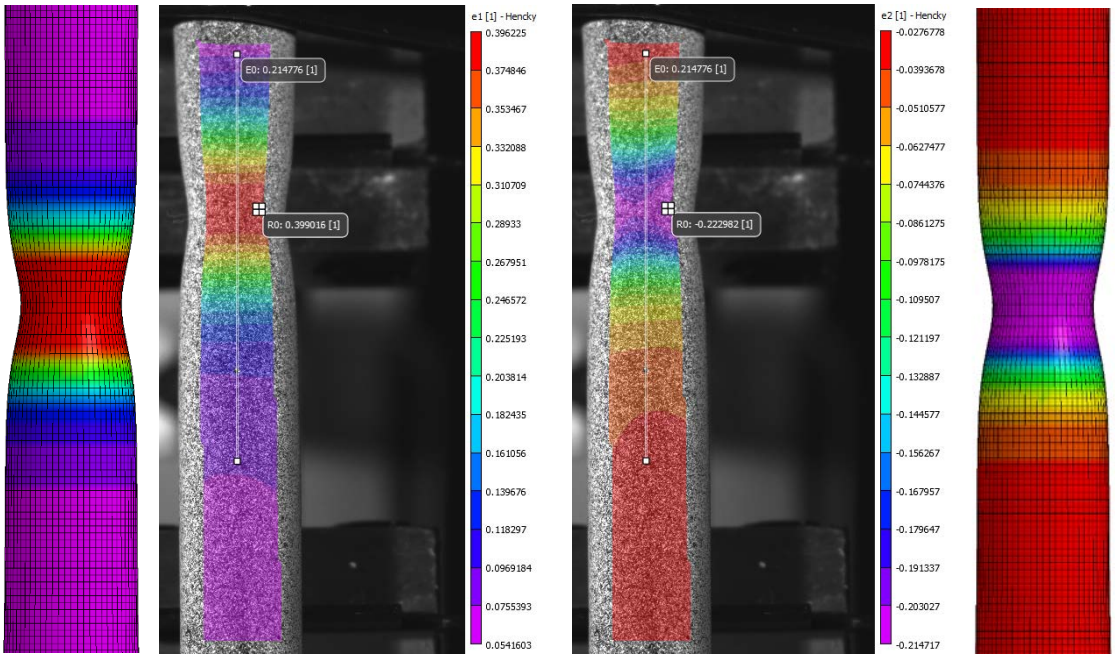

Figure 79: Vertical, 1E-04 /s Test #4 with Test #1 Material Card Principal Strain Comparison

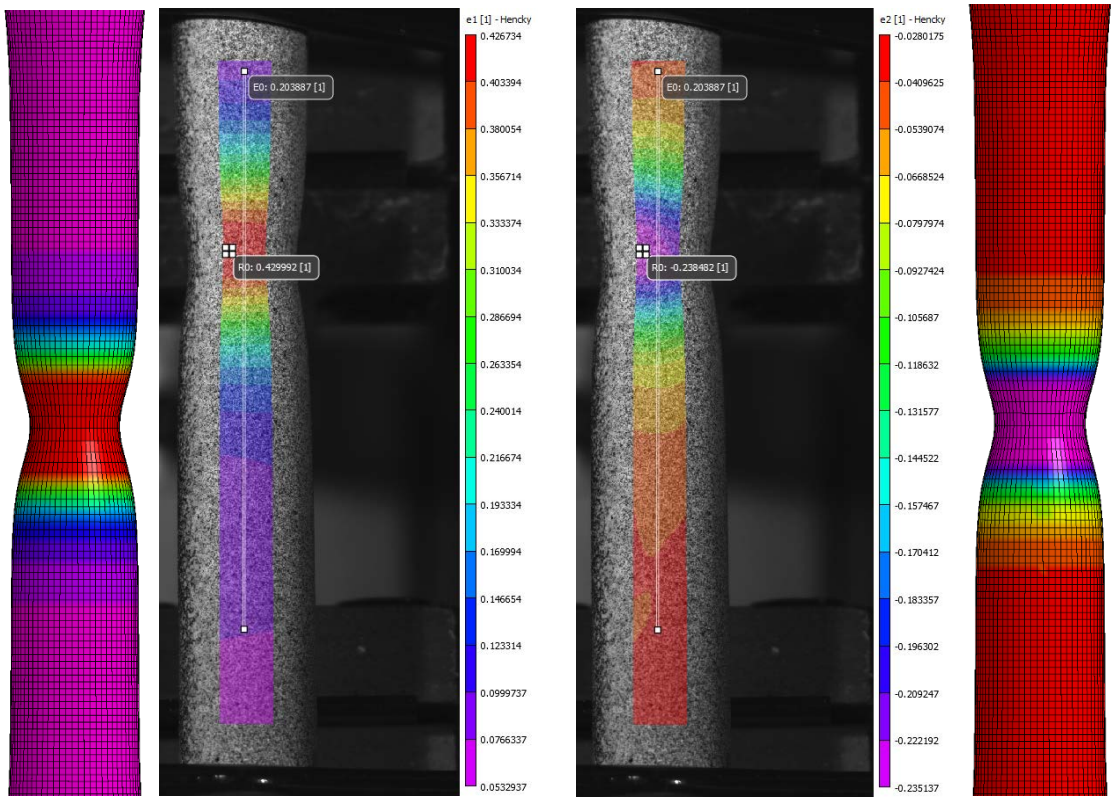

Figure 80: Vertical, 1E-04 /s Test #5 with Test #1 Material Card Principal Strain Comparison

3.4.2 Diagonal, 1E-04 /s

3.4.2.1 Iterative Simulations for Material Card Generation

The "fan" of trial post-necking equivalent true stress-strain curves for the second of six parameter cases (diagonal, 1E-04 /s) Test #6 (Figure 69**)** was used as the basis for an iterative FEMU approach (Sec. 2.3.3). In our implementation, a cost function (with a specified convergence criterion or termination threshold) exploring the full (continuous) parameter range of the post-necking hardening exponent n (between perfect plasticity and upper bound) was not employed. Rather, the (discrete) trial curve from Figure 69 that produces the lowest normalized mean squared error between test and experiment was adopted as the "optimal" equivalent true stress-strain curve.

The first guess (upper bound with a post-necking hardening exponent $n = 0.0584$) simulation agrees very well with the experiment for force vs. displacement (Figure 81), except for the maximum principal strain vs. displacement at large strains, where results diverge.

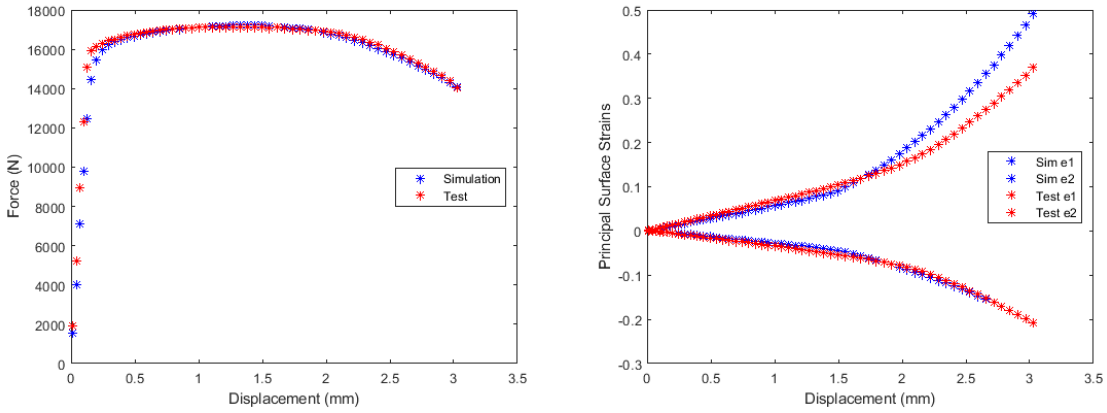

Figure 81: Diagonal, 1E-04 /s Test #6 First Guess Simulation vs. Test

In attempt minimize the error between simulation and experiment for the maximum principal surface strain vs. displacement, a second guess (first interior curve in Figure 69 with a lower post-necking hardening exponent $n = 0.0302$) was taken from the "fan" of prospective curves. The second guess results in worse agreement for force vs. displacement and principal strain vs. displacement between simulation and experiment (Figure 82), with an increase in normalized mean square error (Table 28) across all metrics. Therefore, the equivalent true stress-strain curve corresponding to Test #6, Guess #1 (Figure 83) was selected as our "optimal" candidate.

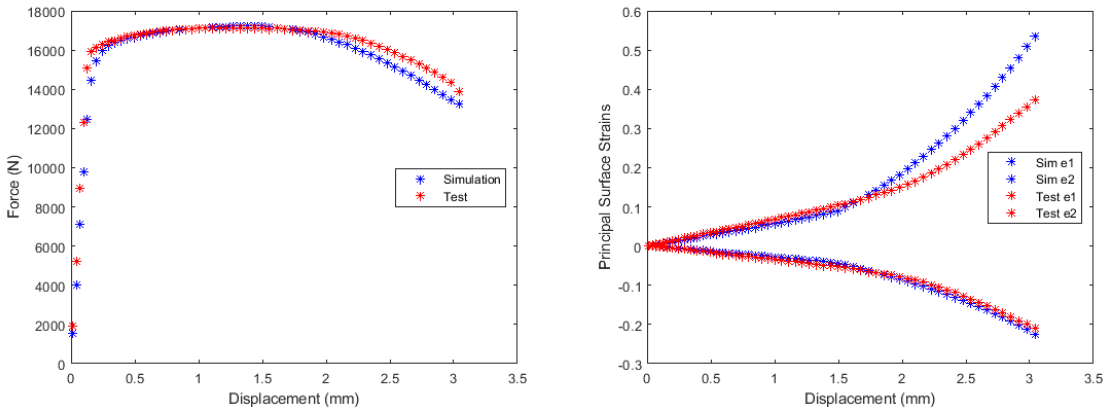

Figure 82: Diagonal, 1E-04 /s Test #6 Second Guess Simulation vs. Test

Table 28: Diagonal, 1E-04 /s Test #6 Normalized Mean Square Error Comparison

Test	Force-Displacement	e1-Displacement	e2-Displacement
Test #6 1st Guess	4.73e-07	3.99e-05	1.93e-06
Test #6 2nd Guess	6.41e-07	6.92e-05	4.19e-06

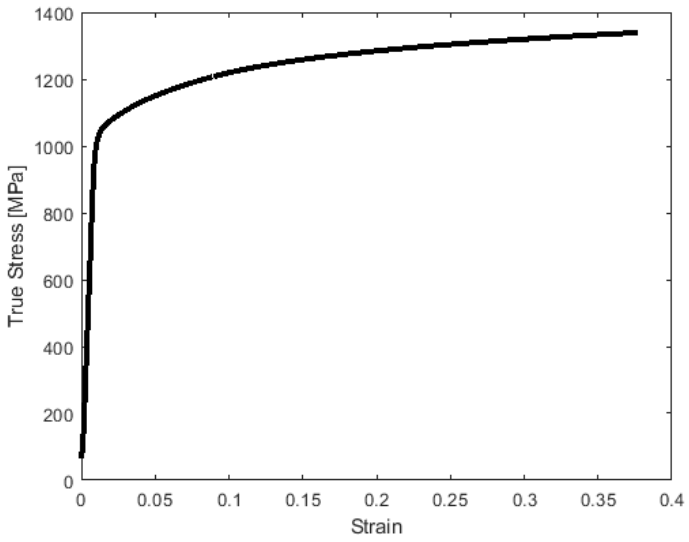

Figure 83: Diagonal, 1E-04 /s Test #6 True Stress-Strain Input Curve

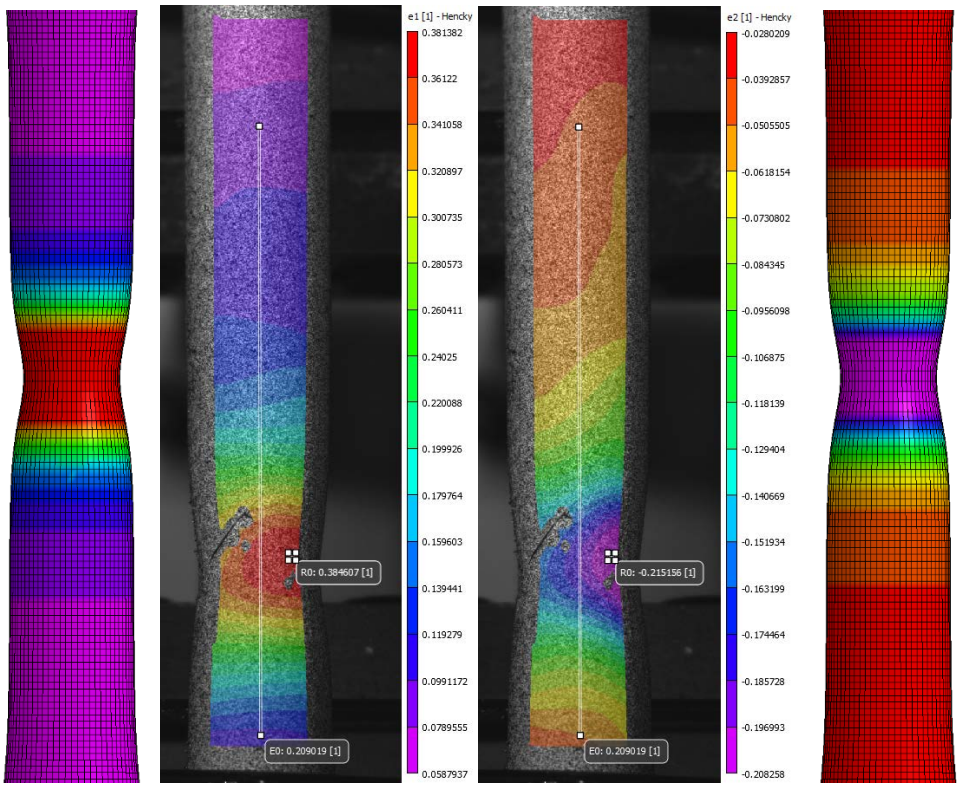

Figure 84: Diagonal, 1E-04 /s Test #6 First Guess Principal Strain Comparison

3.4.2.2 Validation Simulations

Next, for validation purposes, the true stress-strain behavior from Test #6, Guess #1 was used to simulate the remaining four experiments in the diagonal, 1E-04 /s tensile test series. Good agreement is seen between simulation and experiment for Tests #7-#10 (Figure 85-Figure 88) corroborated by the error metrics in Table 29.

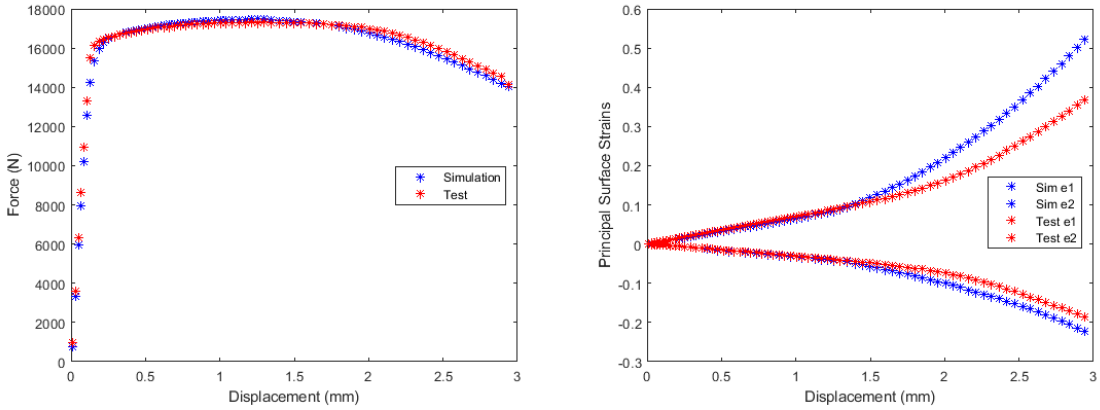

Figure 85: Diagonal, 1E-04 /s Test #7 with Test #6 First Guess Material Card

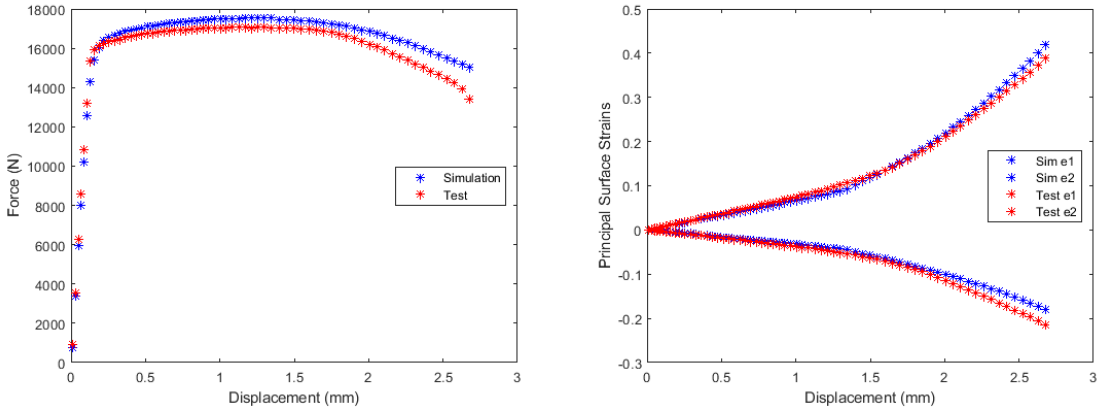

Figure 86: Diagonal, 1E-04 /s Test #8 with Test #6 First Guess Material Card

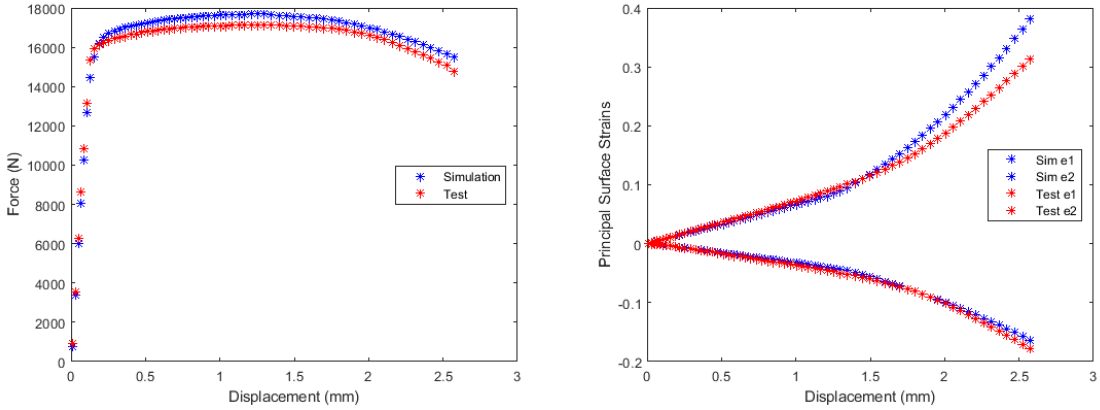

Figure 87: Diagonal, 1E-04 /s Test #9 with Test #6 First Guess Material Card

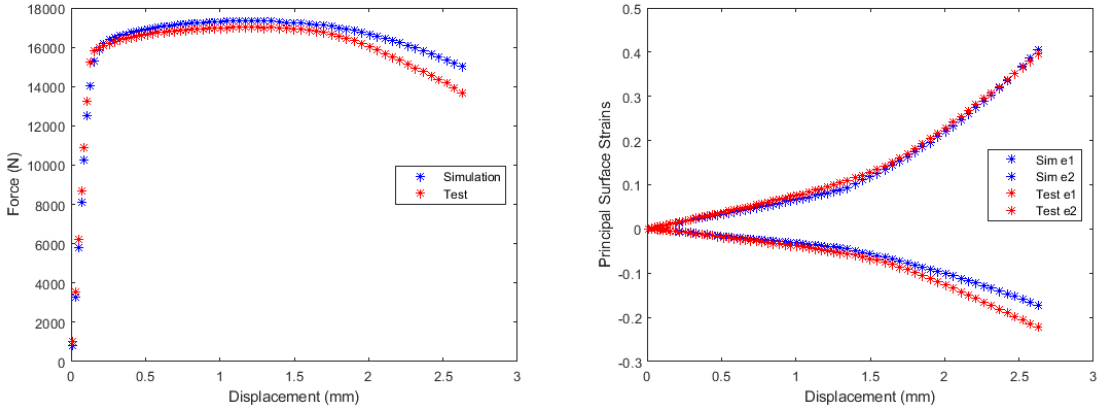

Figure 88: Diagonal, 1E-04 /s Test #10 with Test #6 First Guess Material Card

Table 29: Diagonal, 1E-04 /s Validation Simulations Normalized Mean Square Error Comparison

Test	Force-Displacement	e1-Displacement	e2-Displacement
Test #7	7.77e-08	5.07e-05	2.29e-05
Test #8	3.61e-07	1.66e-06	1.00e-05
Test #9	2.44e-07	1.29e-05	2.00e-06
Test #10	3.33e-07	9.06e-07	2.13e-05

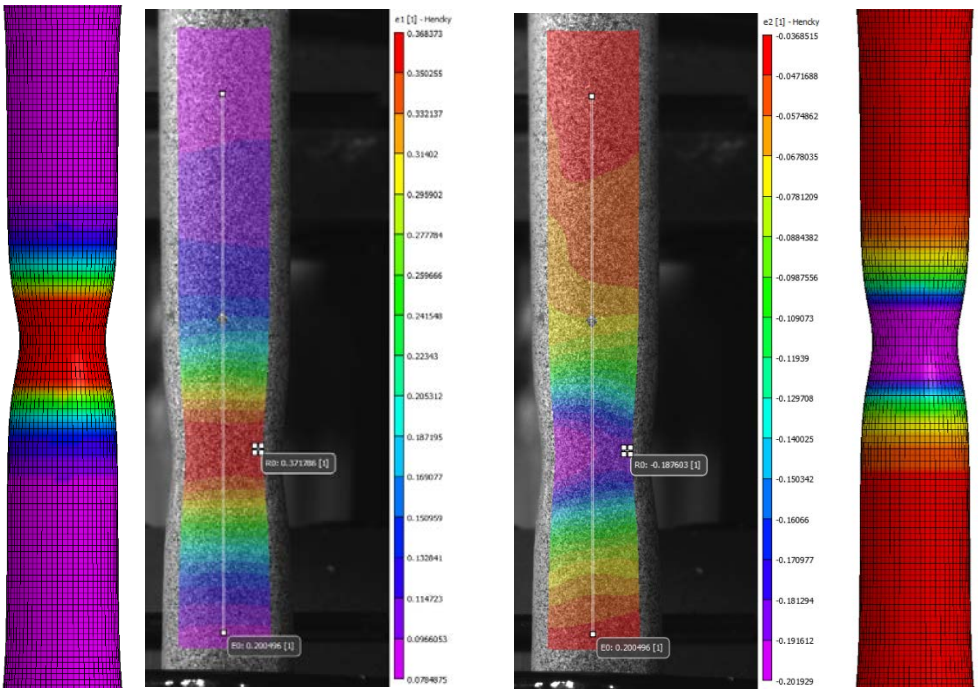

Figure 89: Diagonal, 1E-04 /s Test #7 with Test #6 Material Card Principal Strain Comparison

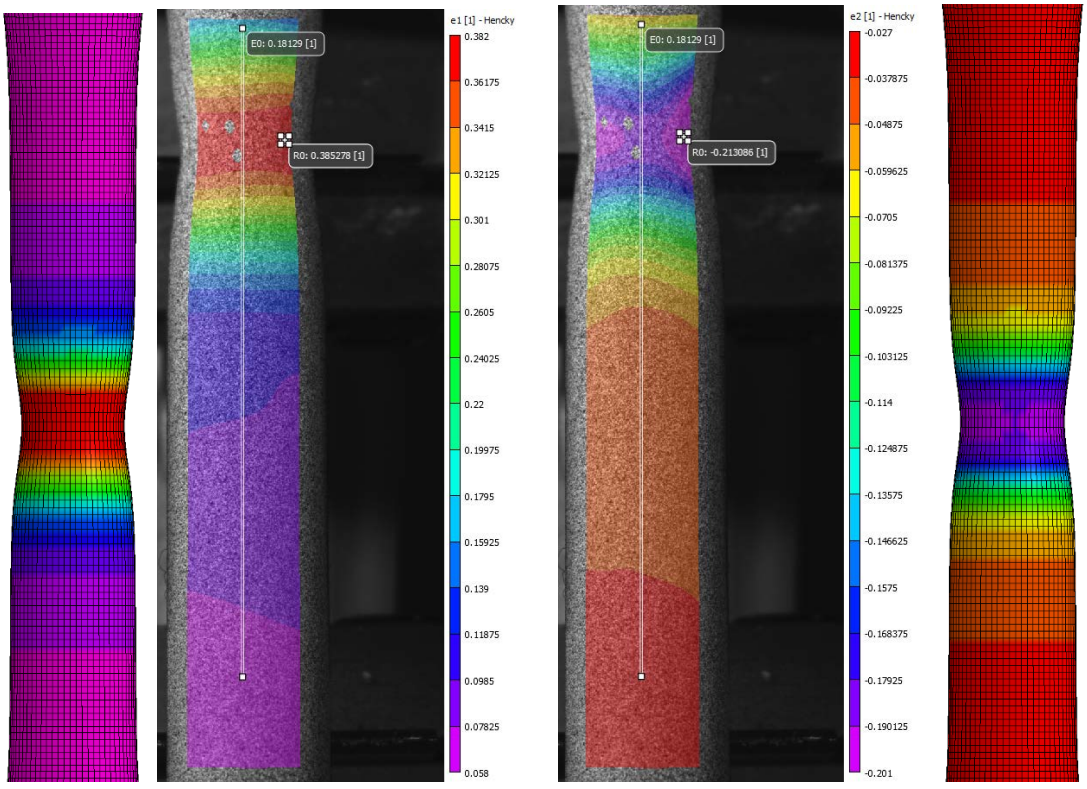

Figure 90: Diagonal, 1E-04 /s Test #8 with Test #6 Material Card Principal Strain Comparison

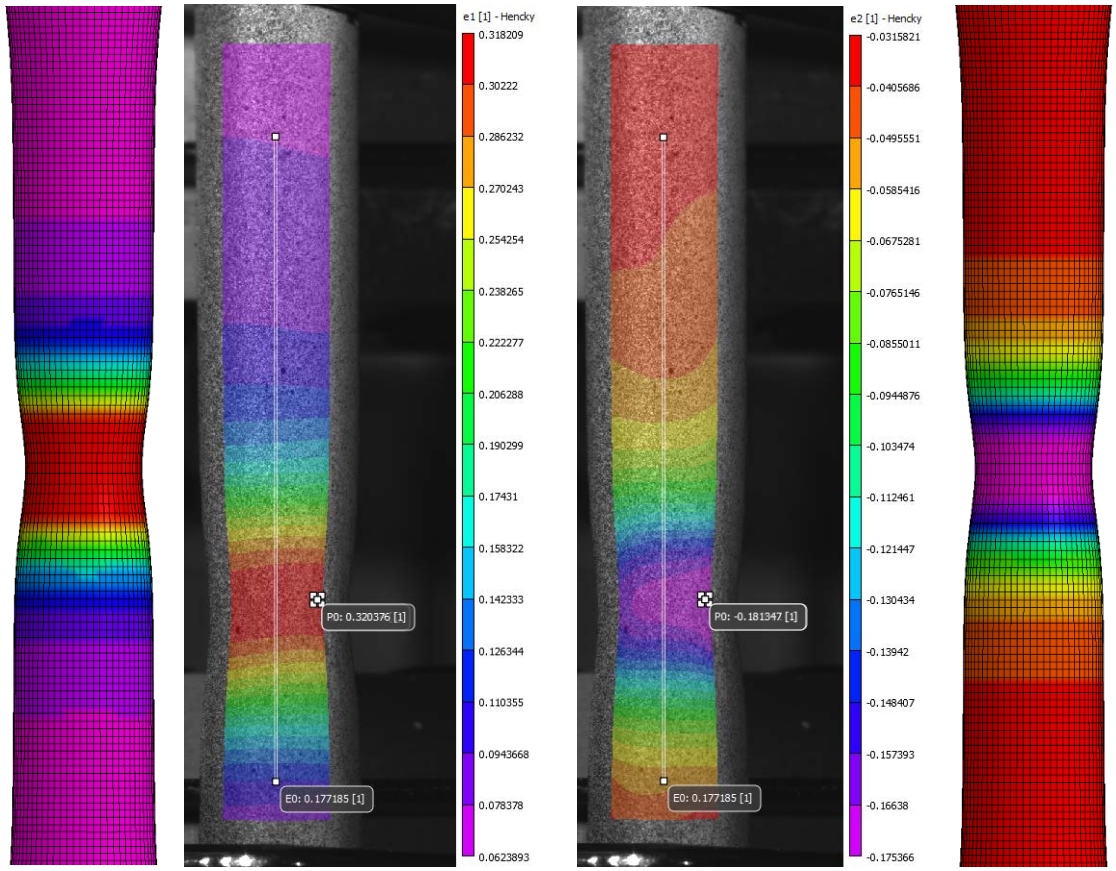

Figure 91: Diagonal, 1E-04 /s Test #9 with Test #6 Material Card Principal Strain Comparison

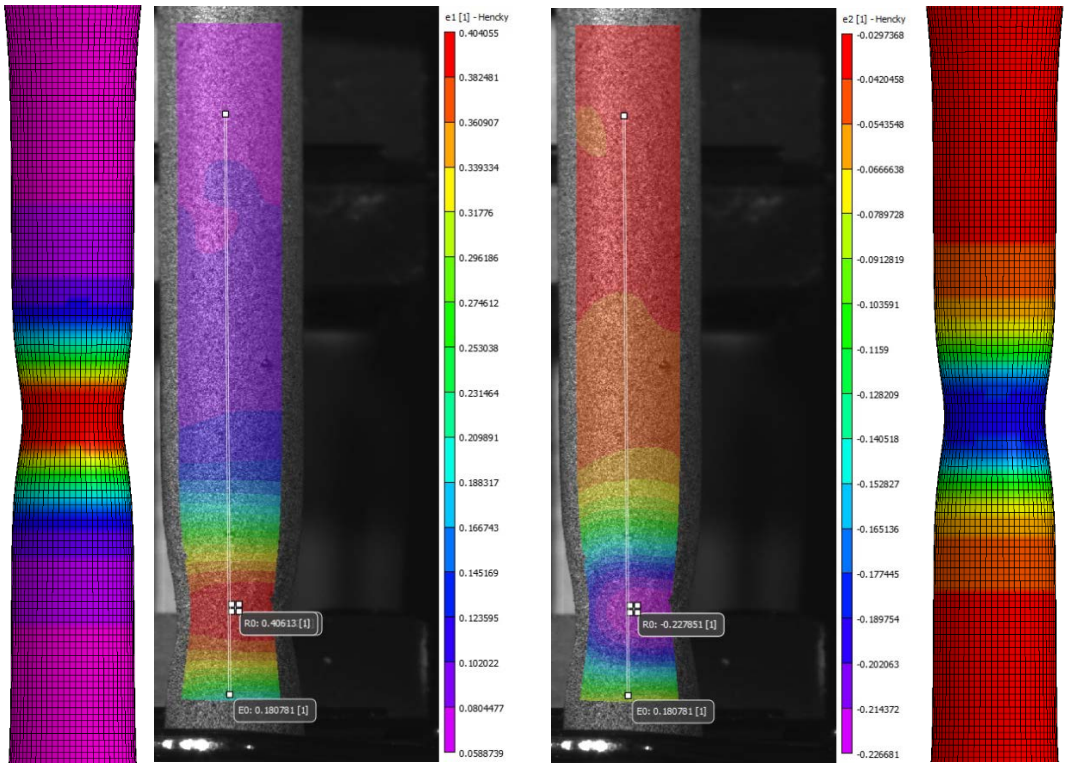

Figure 92: Diagonal, 1E-04 /s Test #10 with Test #6 Material Card Principal Strain Comparison

3.4.3 Horizontal, 1E-04 /s

3.4.3.1 Iterative Simulations for Material Card Generation

The "fan" of trial post-necking equivalent true stress-strain curves for the third of six parameter cases (horizontal, 1E-04 /s) Test #11 (Figure 69**)** was used as the basis for an iterative FEMU approach (Sec. 2.3.3). In our implementation, a cost function (with a specified convergence criterion or termination threshold) exploring the full (continuous) parameter range of the post-necking hardening exponent n (between perfect plasticity and upper bound) was not employed. Rather, the (discrete) trial curve from Figure 69 that produces the lowest normalized mean squared error between test and experiment was adopted as the "optimal" equivalent true stress-strain curve.

The first guess (upper bound with a post-necking hardening exponent $n = 0.0731$) simulation agrees very well with the experiment for force vs. displacement (Figure 93), except for the maximum principal strain vs. displacement at large strains, where results diverge.

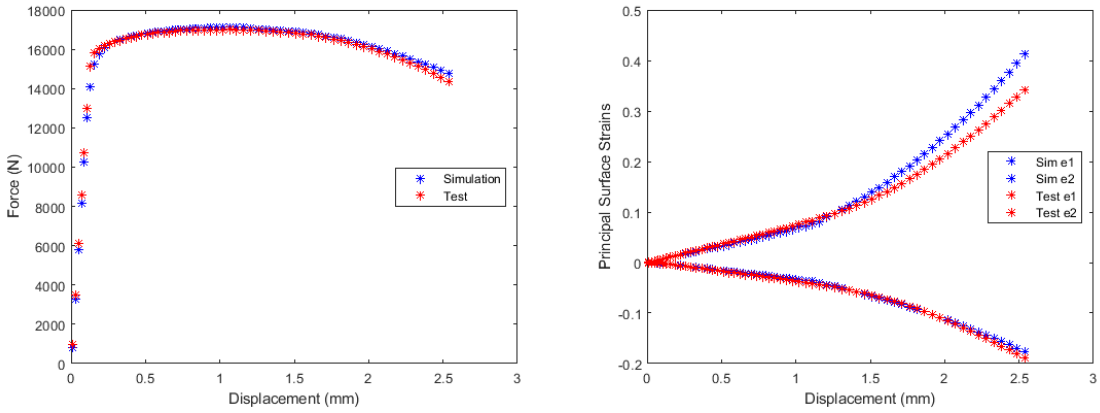

Figure 93: Horizontal, 1E-04 /s Test #11 First Guess Simulation vs. Test

In attempt minimize the error between simulation and experiment for the maximum principal surface strain vs. displacement, a second guess (first interior curve in Figure 69 with a lower post-necking hardening exponent $n = 0.0379$) was taken from the "fan" of prospective curves. The second guess results in slightly worse agreement between simulation and experiment (Figure 94), with an increase in normalized mean square error (Table 30) across two of the three metrics. Therefore, the equivalent true stress-strain curve corresponding to Test #6, Guess #1 (Figure 95) was selected as our "optimal" candidate.

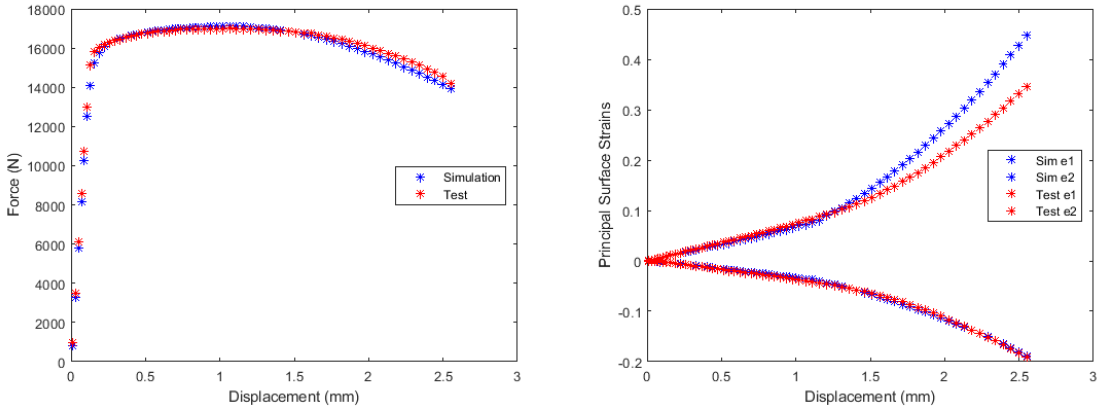

Figure 94: Horizontal, 1E-04 /s Test #11 Second Guess Simulation vs. Test

Table 30: Horizontal, 1E-04 /s Test #11 Normalized Mean Square Error Comparison

Test	Force-Displacement	e1-Displacement	e2-Displacement
Test 11 1st Guess	5.85e-08	1.48e-05	1.26e-06
Test 11 2nd Guess	7.97e-08	3.07e-05	5.55e-07

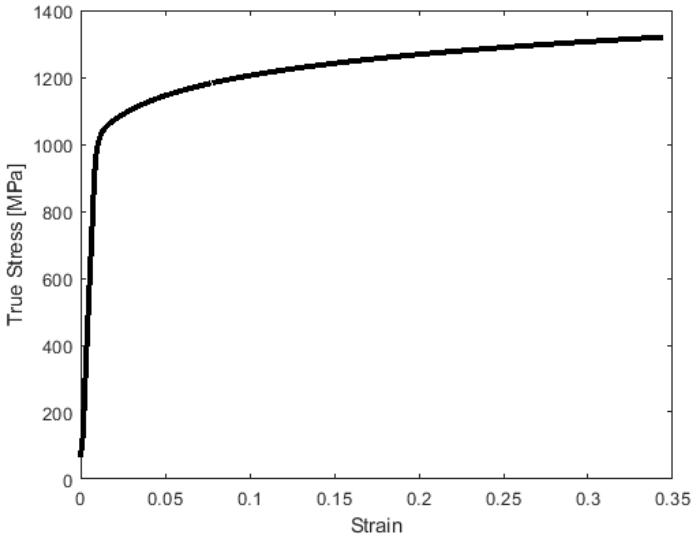

Figure 95: Horizontal, 1E-04 /s Test #11 True Stress-Strain Input Curve

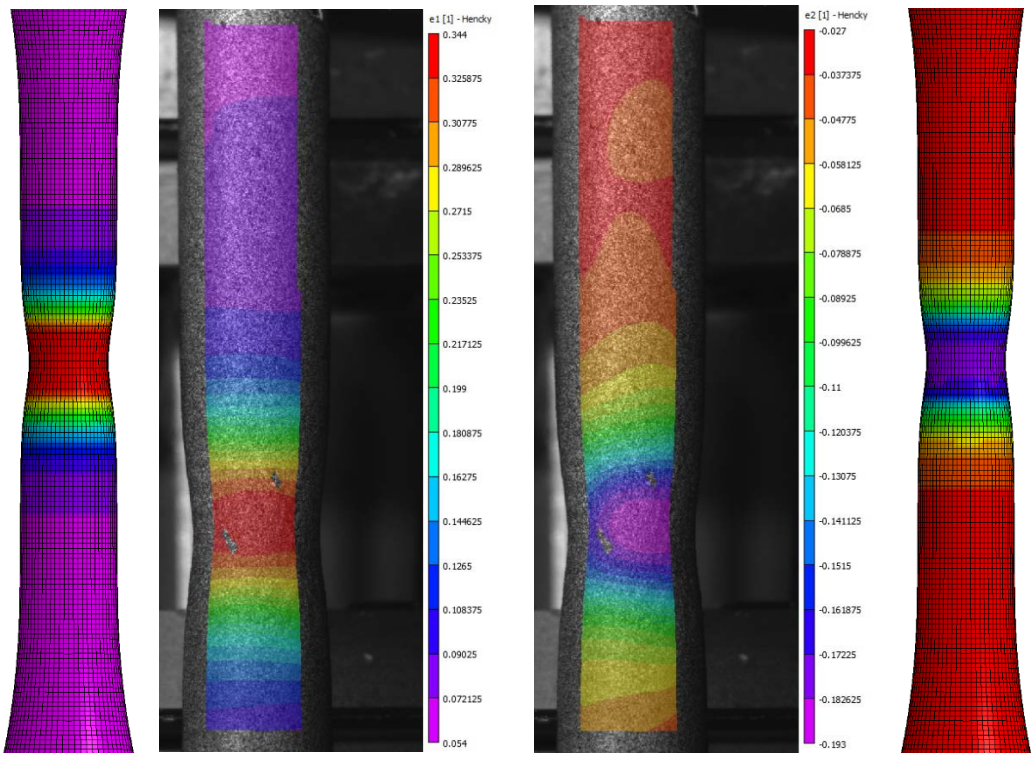

Figure 96: Horizontal, 1E-04 /s Test #11 First Guess Principal Strain Comparison

3.4.3.2 Validation Simulations

Next, for validation purposes, the true stress-strain behavior from Test #11, Guess #1 was used to simulate the remaining four experiments in the horizontal, 1E-04 /s tensile test series. Good agreement is seen between simulation and experiment for Test #13 (Figure 97) and Test #15 (Figure 98) corroborated by the error metrics in Table 30. Test #12 and Test #14 were not processed.

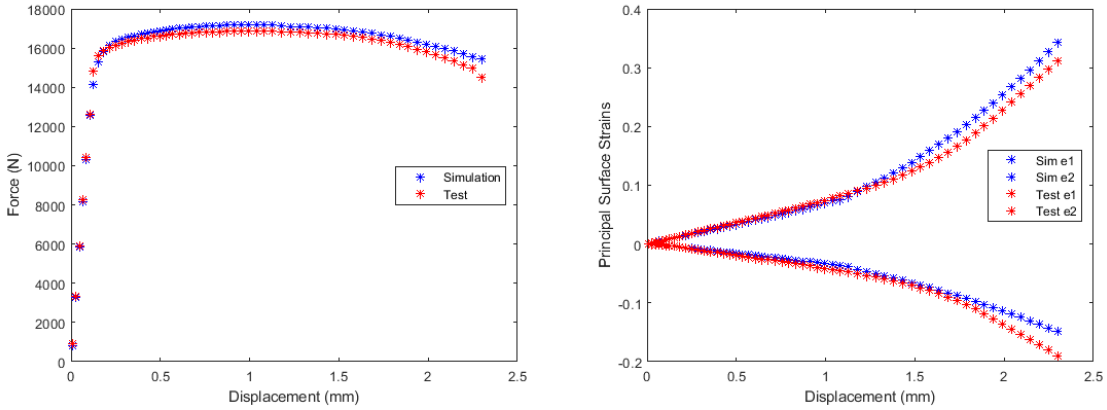

Figure 97: Horizontal, 1E-04 /s Test #13 with Test #11 First Guess Material Card

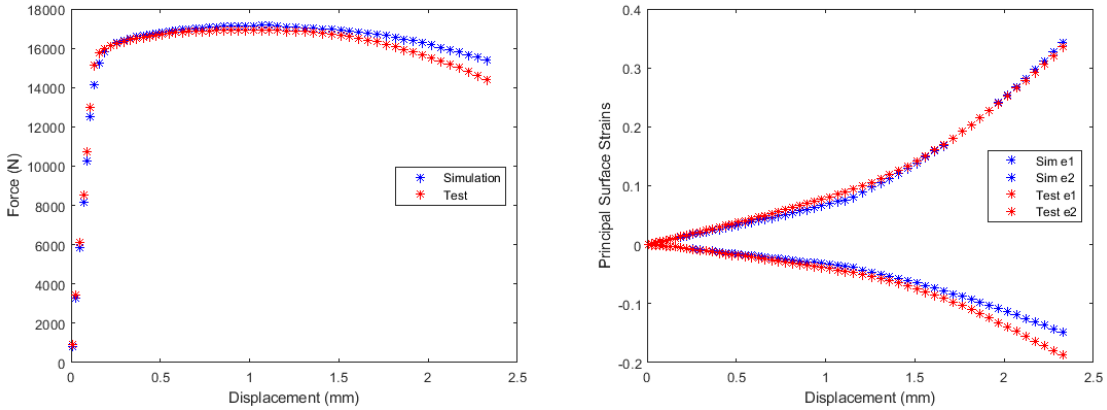

Figure 98: Horizontal, 1E-04 /s Test #15 with Test #11 First Guess Material Card

Table 31: Horizontal, 1E-04 /s Validation Simulations Normalized Mean Square Error Comparison

Test	Force-Displacement	e1-Displacement	e2-Displacement
Test #13	1.44e-07	6.97e-06	1.69e-05
Test #15	2.24e-07	9.20e-07	1.92e-05

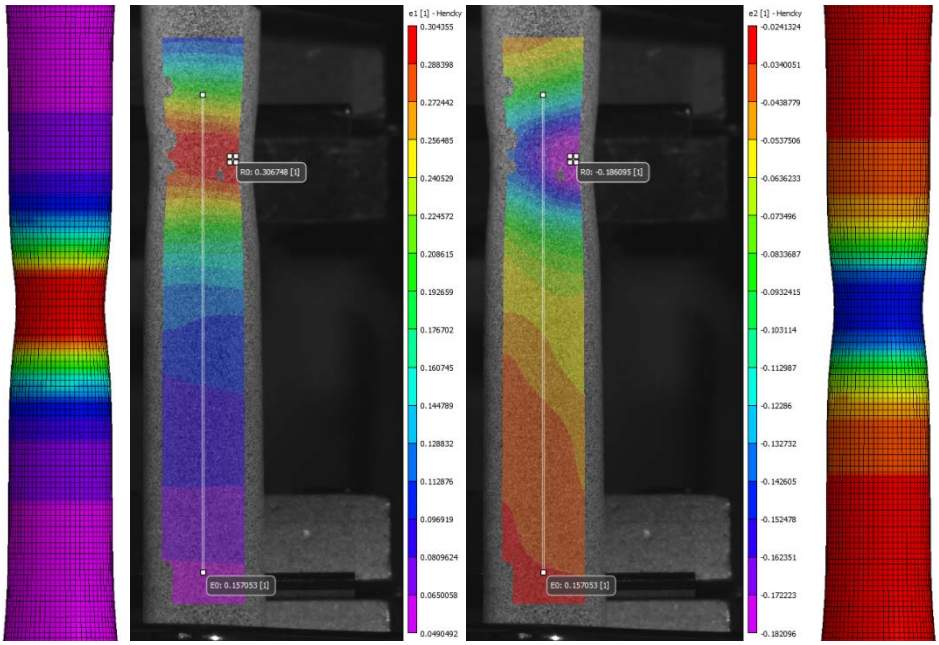

Figure 99: Horizontal, 1E-04 /s Test #13 with Test #11 Material Card Principal Strain Comparison

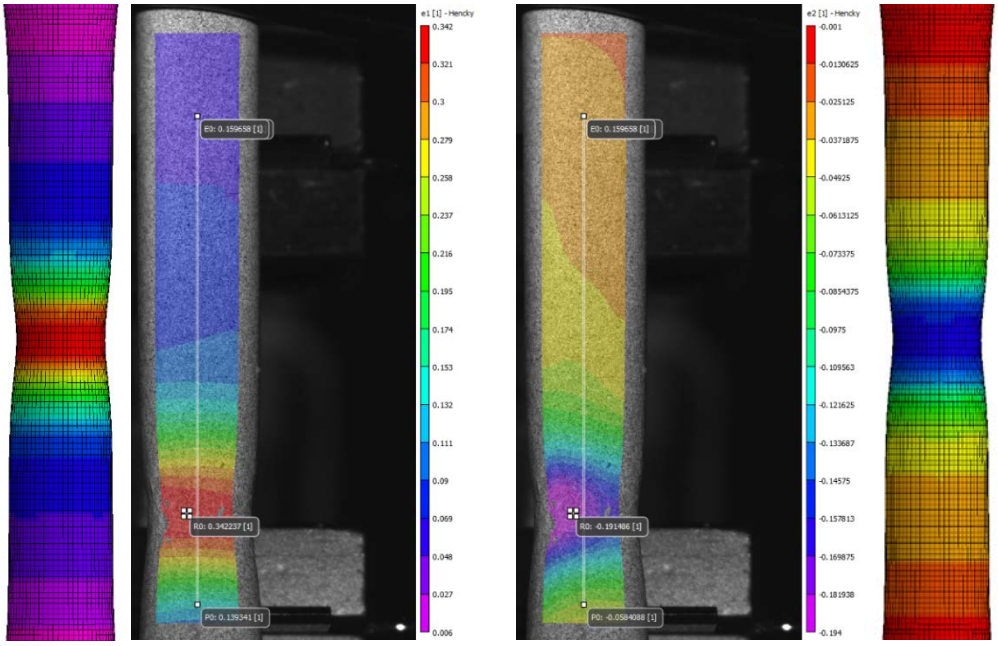

Figure 100: Horizontal, 1E-04 /s Test #15 with Test #11 Material Card Principal Strain Comparison

3.4.4 Vertical, 1E-02 /s

3.4.4.1 Iterative Simulations for Material Card Generation

The "fan" of trial post-necking equivalent true stress-strain curves for the fourth of six parameter cases (vertical, 1E-02 /s) Test #17 (Figure 69) was used as the basis for an iterative FEMU approach (Sec. 2.3.3). In our implementation, a cost function (with a specified convergence criterion or termination threshold) exploring the full (continuous) parameter range of the post-necking hardening exponent n (between perfect plasticity and upper bound) was not employed. Rather, the (discrete) trial curve from Figure 69 that produces the lowest normalized mean squared error between test and experiment was adopted as the "optimal" equivalent true stress-strain curve.

The first guess (upper bound with a post-necking hardening exponent $n = 0.0346$) simulation agrees well with the experiment until larger strains (Figure 101), where the maximum principal strain vs. displacement results diverge.

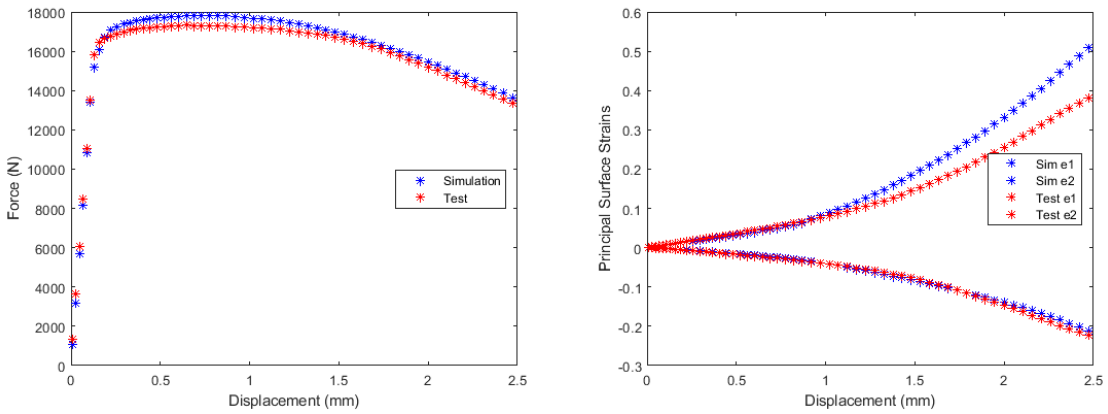

Figure 101: Vertical, 1E-02 /s Test #17 First Guess Simulation vs. Test

In attempt to minimize the error between simulation and test for the maximum principal strain vs. displacement, a second guess (first interior curve in Figure 69 with a lower post-necking hardening exponent $n = 0.0179$) was taken from the "fan" of prospective curves. The second

guess results in roughly the same agreement for force vs. displacement between simulation and experiment (Figure 102), with a small reduction in normalized mean square error (Table 32) for two of the three metrics. Therefore, the equivalent true stress-strain curve corresponding to Test #1, Guess #2 (Figure 104) was selected as our "optimal" candidate.

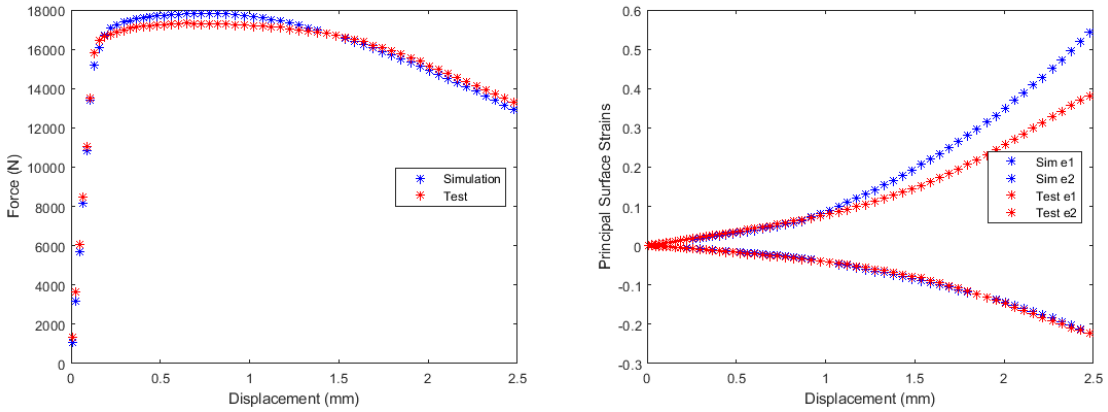

Figure 102: Vertical, 1E-02 /s Test #17 Second Guess Simulation vs. Test

Table 32: Vertical, 1E-02 /s Test #17 Normalized Mean Square Error Comparison

Test	Force-Displacement	e1-Displacement	e2-Displacement
Test #17 1st Guess	1.84e-07	5.01e-05	2.02e-06
Test #17 2nd Guess	1.63e-07	7.53e-05	8.86e-07

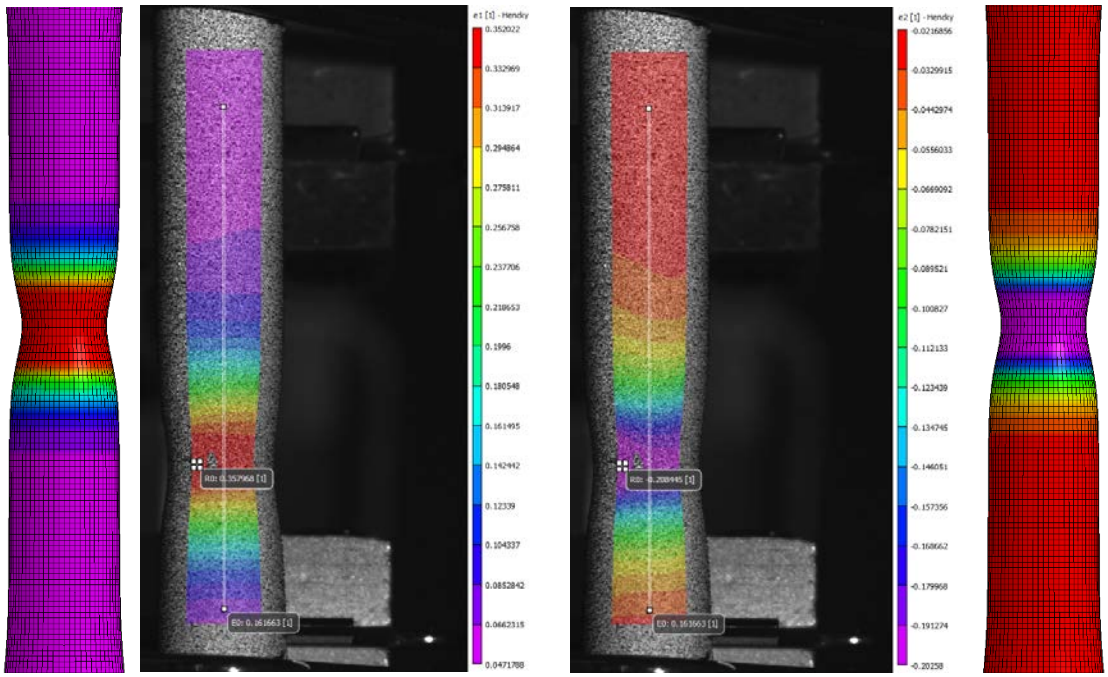

Figure 103: Vertical, 1E-02 /s Test #17 Second Guess Principal Strain Comparison

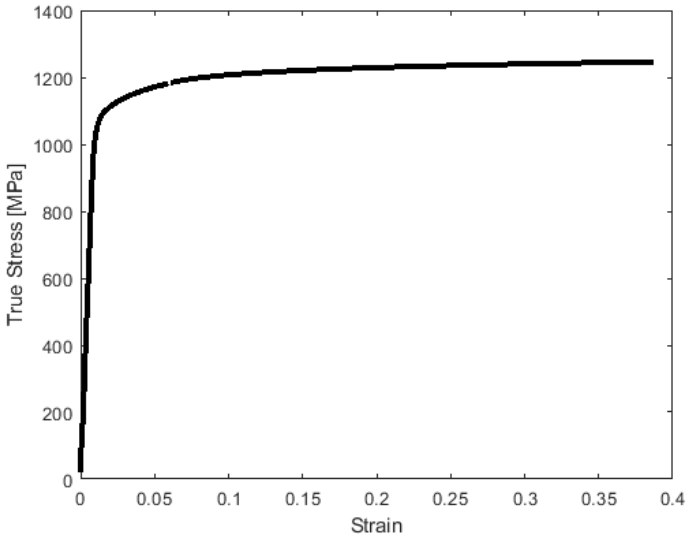

Figure 104: Vertical, 1E-02 /s Test #17 True Stress-Strain Input Curve

3.4.4.2 Validation Simulations

Next, for validation purposes, the true stress-strain behavior from Test #17, Guess #2 was used to simulate the remaining three experiments in the vertical, 1E-02 /s tensile test series (Test #18 was not processed). Good agreement is seen between simulation and experiment for Tests #16 (Figure 105), Test#19 (Figure 106), and Test #20 (Figure 107) corroborated by the error metrics in Table 33.

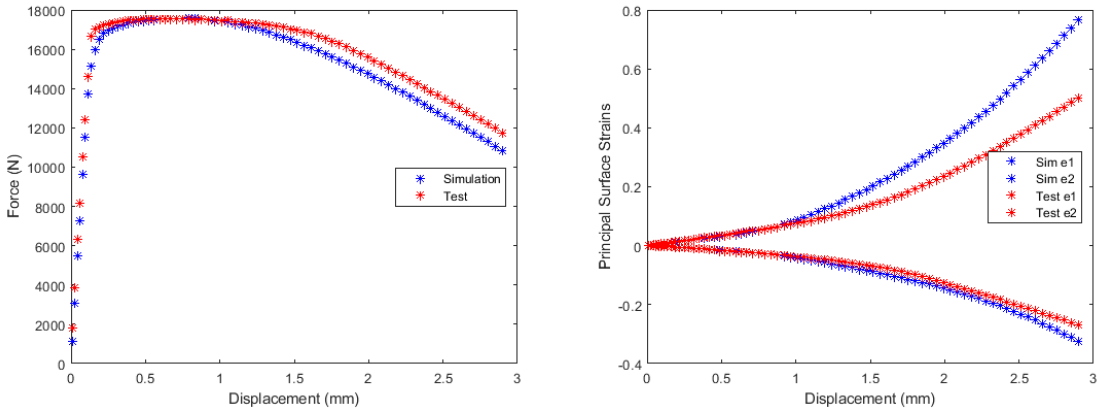

Figure 105: Vertical, 1E-02 /s Test #16 with Test #17 Second Guess Material Card

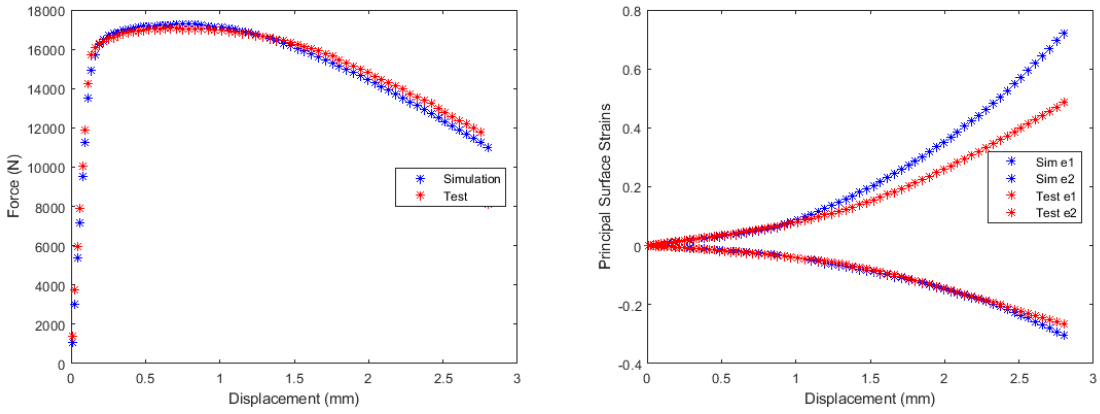

Figure 106: Vertical, 1E-02 /s Test #19 with Test #17 Second Guess Material Card (nominal mesh/specimen)

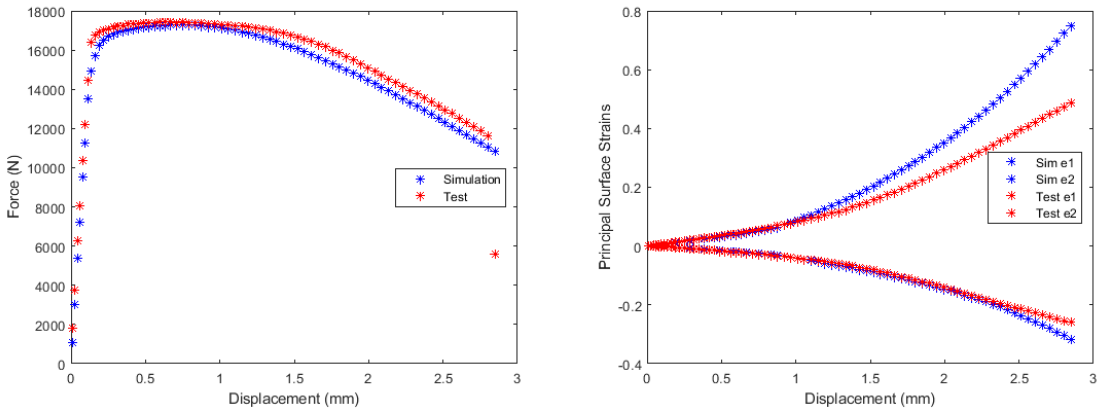

Figure 107: Vertical, 1E-02 /s Test #20 with Test #17 Second Guess Material Card

Table 33: Vertical, 1E-02 /s Validation Simulations Normalized Mean Square Error Comparison

Test	Force-Displacement	e1-Displacement	e2-Displacement
Test #16	3.58e-07	8.73e-05	1.03e-05
Test #19	2.34e-07	6.43e-05	2.33e-06
Test #20	6.29e-07	6.99e-05	5.83e-06

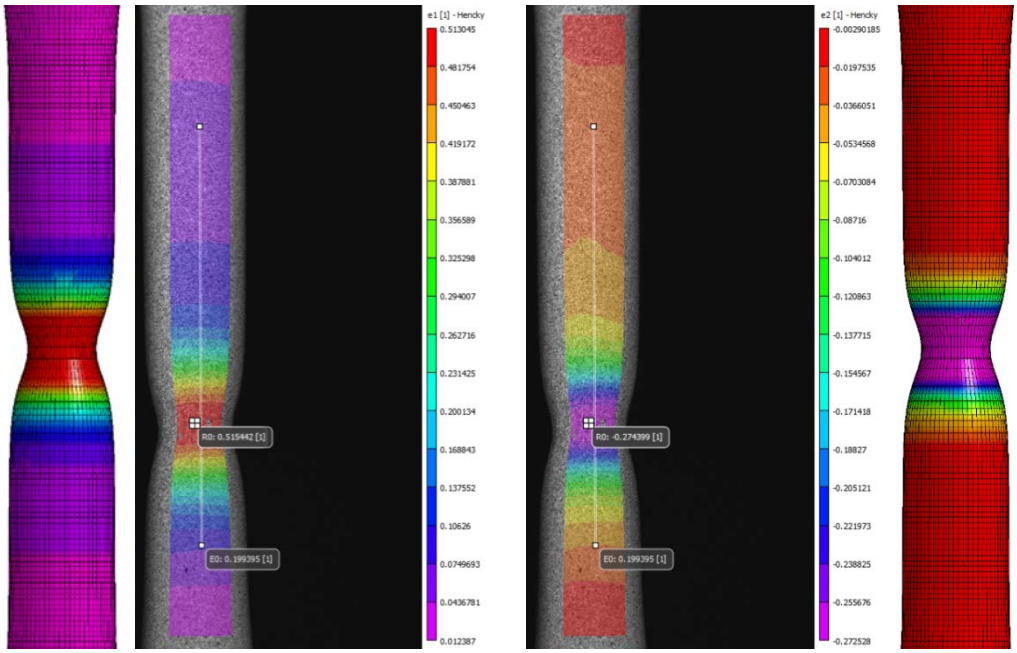

Figure 108: Vertical, 1E-02 /s Test #16 with Test #17 Material Card Principal Strain Comparison

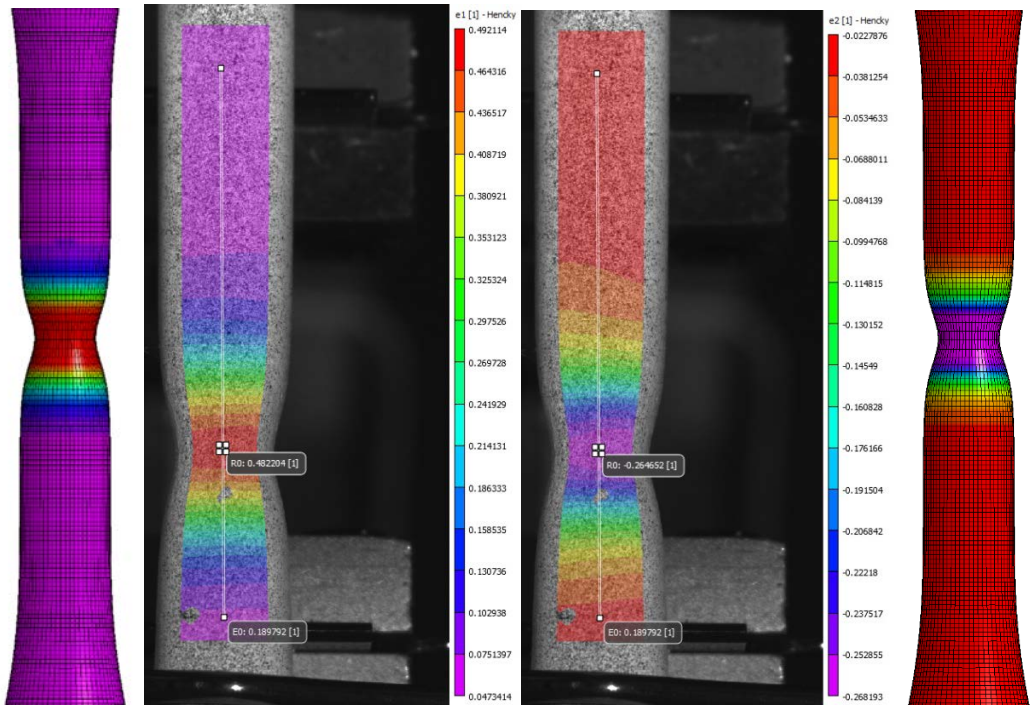

Figure 109: Vertical, 1E-02 /s Test #19 with Test #17 Material Card Principal Strain Comparison

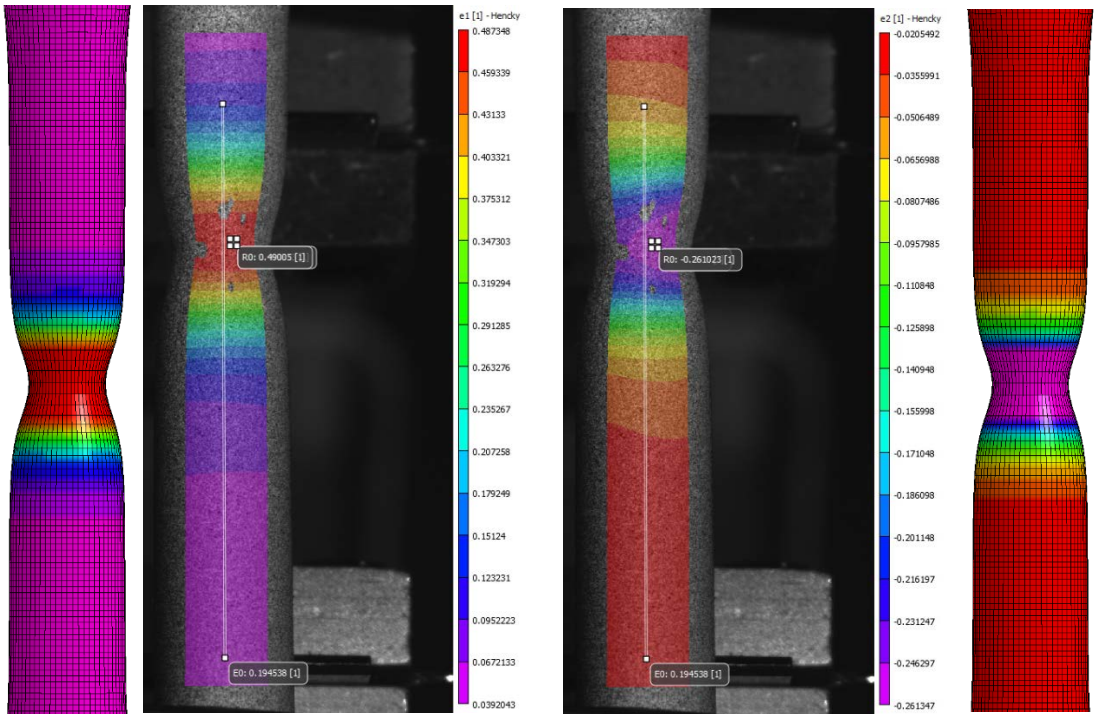

Figure 110: Vertical, 1E-02 /s Test #20 with Test #17 Material Card Principal Strain Comparison

3.4.5 Diagonal, 1E-02 /s

3.4.5.1 Iterative Simulations for Material Card Generation

The "fan" of trial post-necking equivalent true stress-strain curves for the fifth of six parameter cases (diagonal, 1E-02 /s) Test #22 (Figure 69**)** was used as the basis for an iterative FEMU approach (Sec. 2.3.3). In our implementation, a cost function (with a specified convergence criterion or termination threshold) exploring the full (continuous) parameter range of the post-necking hardening exponent n (between perfect plasticity and upper bound) was not employed. Rather, the (discrete) trial curve from Figure 69 that produces the lowest normalized mean squared error between test and experiment was adopted as the "optimal" equivalent true stress-strain curve.

The first guess (upper bound with a post-necking hardening exponent $n = 0.0309$) simulation agrees very well with the experiment for force vs. displacement (Figure 111), except for the maximum principal strain vs. displacement at large strains, where results diverge.

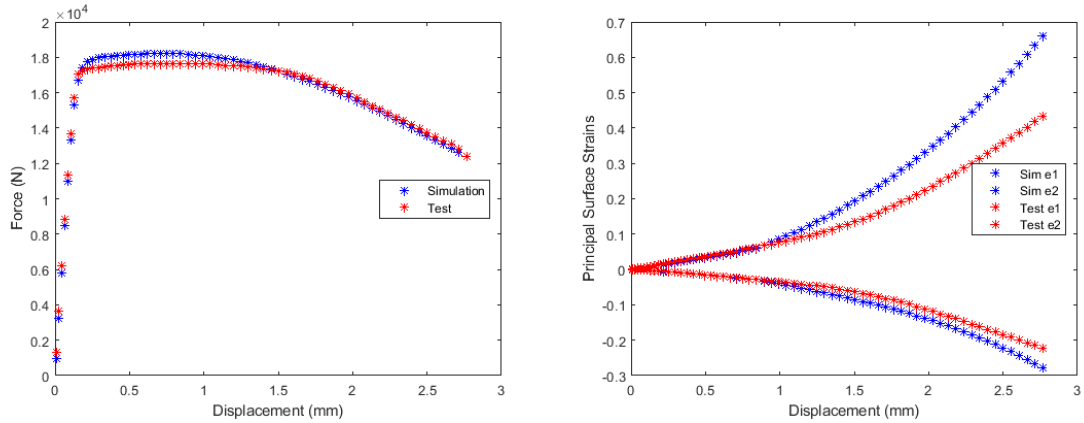

Figure 111: Diagonal, 1E-02 /s Test #22 First Guess Simulation vs. Test

In attempt minimize the error between simulation and experiment for the maximum principal surface strain vs. displacement, a second guess (first interior curve in Figure 69 with a

lower post-necking hardening exponent $n = 0.0160$) was taken from the "fan" of prospective curves. The second guess results in worse agreement for force vs. displacement and principal strain vs. displacement between simulation and experiment (Figure 112), with an increase in normalized mean square error (Table 34) across all metrics. Therefore, the equivalent true stress-strain curve corresponding to Test #6, Guess #1 (Figure 114) was selected as our "optimal" candidate.

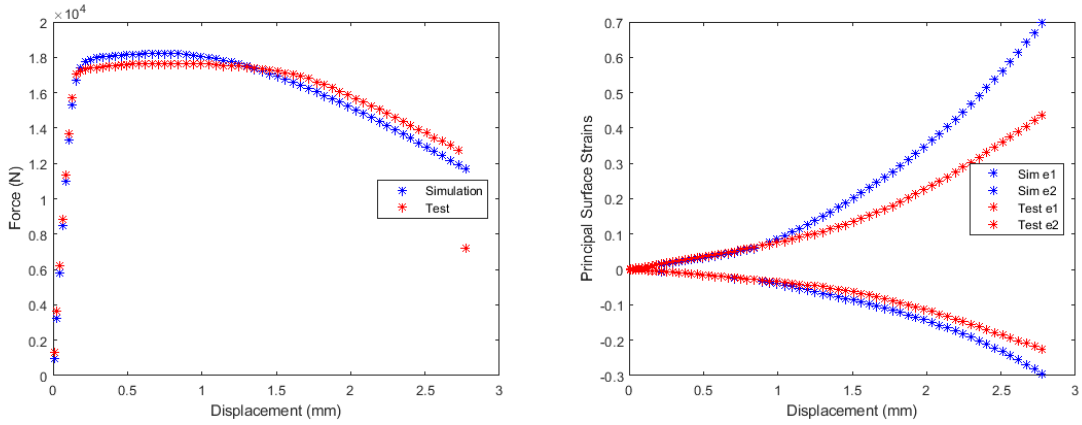

Figure 112: Diagonal, 1E-02 /s Test #22 Second Guess Simulation vs. Test

Table 34: Diagonal, 1E-02 /s Test #22 Normalized Mean Square Error Comparison

Test	Force-Displacement	e1-Displacement	e2-Displacement
Test #22 1st Guess	1.38e-07	1.10e-04	2.69e-05
Test #22 2nd Guess	6.62e-07	1.44e-04	3.83e-05

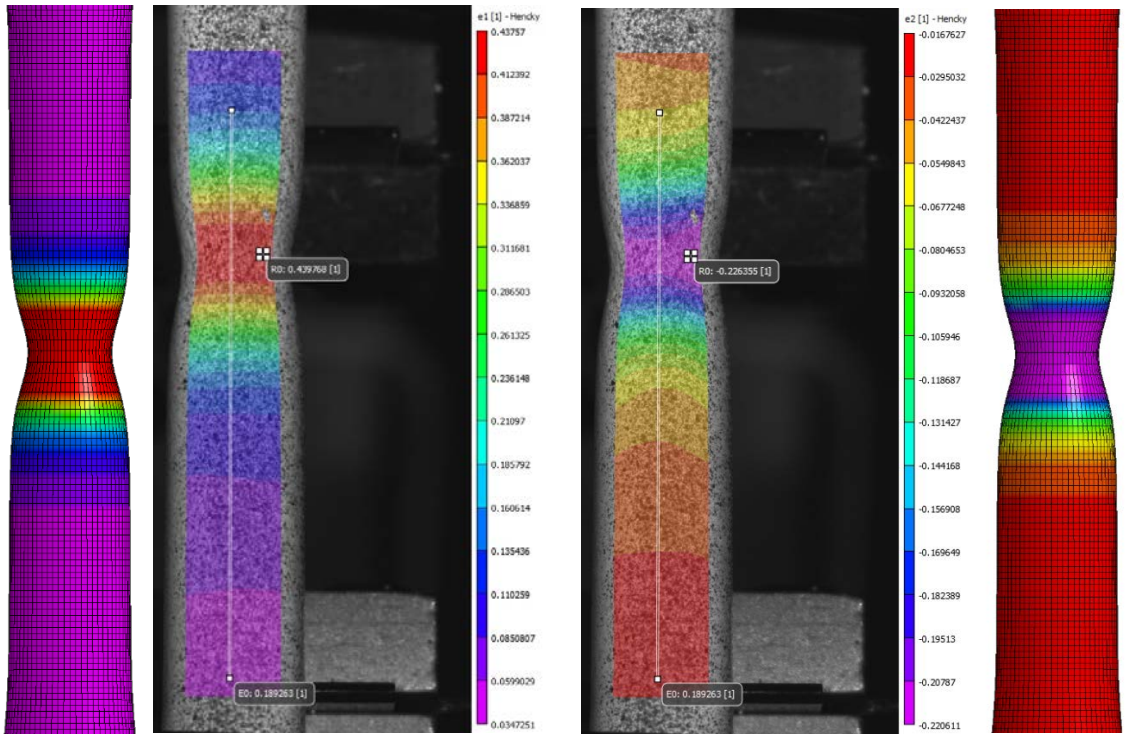

Figure 113: Diagonal, 1E-02 /s Test #22 First Guess Principal Strain Comparison

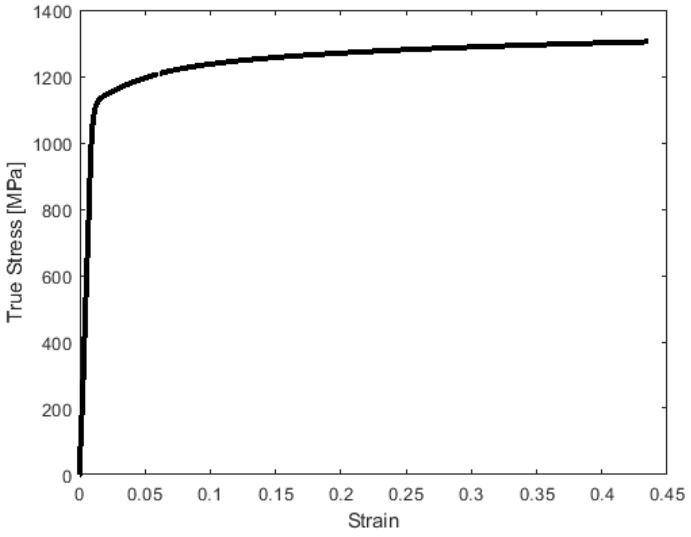

Figure 114: Diagonal, 1E-02 /s Test #22 True Stress-Strain Input Curve

3.4.5.2 Validation Simulations

Next, for validation purposes, the true stress-strain behavior from Test #22, Guess #1 was used to simulate the remaining four experiments in the diagonal, 1E-02 /s tensile test series. Good agreement is seen between simulation and experiment for Test #21 (Figure 115), and Test #23-25 (Figure 116-Figure 118) corroborated by the error metrics in Table 35.

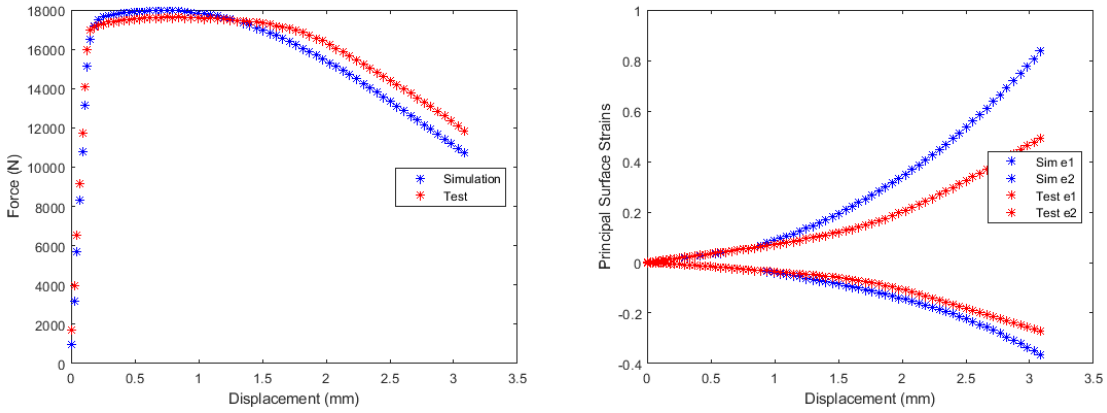

Figure 115: Diagonal, 1E-02 /s Test #21 with Test #22 First Guess Material Card

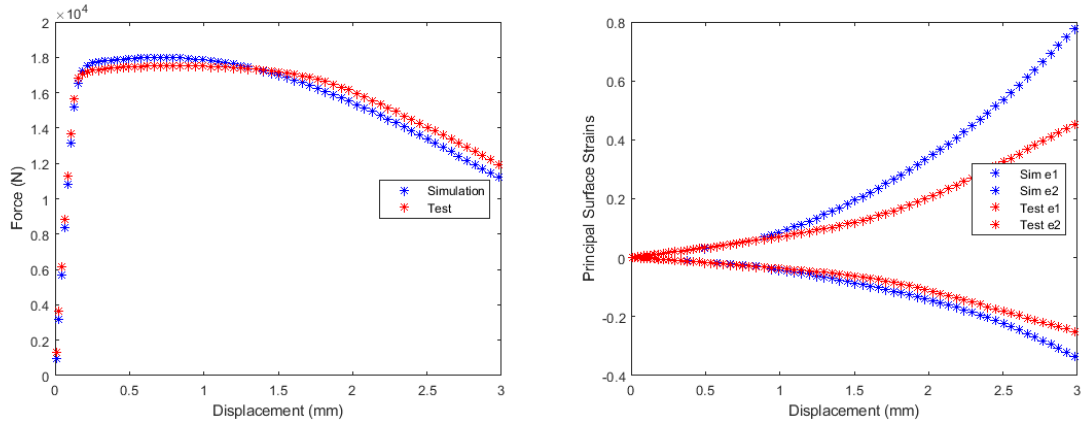

Figure 116: Diagonal, 1E-02 /s Test #23 with Test #22 First Guess Material Card

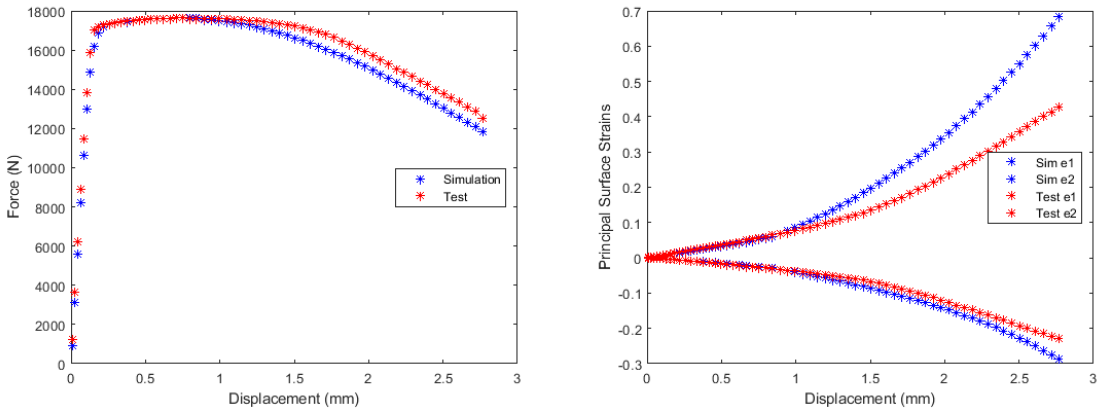

Figure 117: Diagonal, 1E-02 /s Test #24 with Test #22 First Guess Material Card (nominal mesh/specimen)

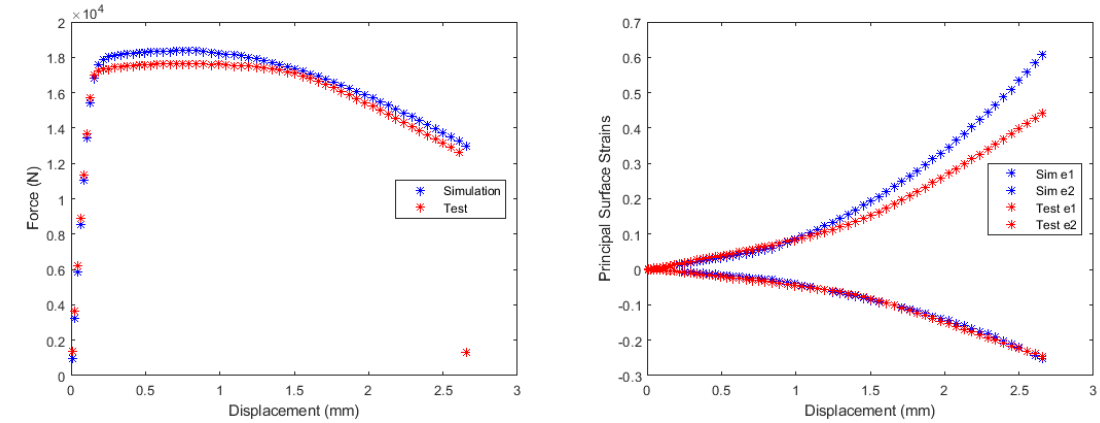

Figure 118: Diagonal, 1E-02 /s Test #25 with Test #22 First Guess Material Card

Table 35: Diagonal, 1E-02 /s Validation Simulations Normalized Mean Square Error Comparison

Test	Force-Displacement	e1-Displacement	e2-Displacement
Test #21	4.85e-07	1.78e-04	3.60e-05
Test #23	2.54e-07	1.87e-04	3.48e-05
Test #24	3.27e-07	1.29e-04	2.00e-05
Test #25	3.04e-06	4.86e-05	1.14e-06

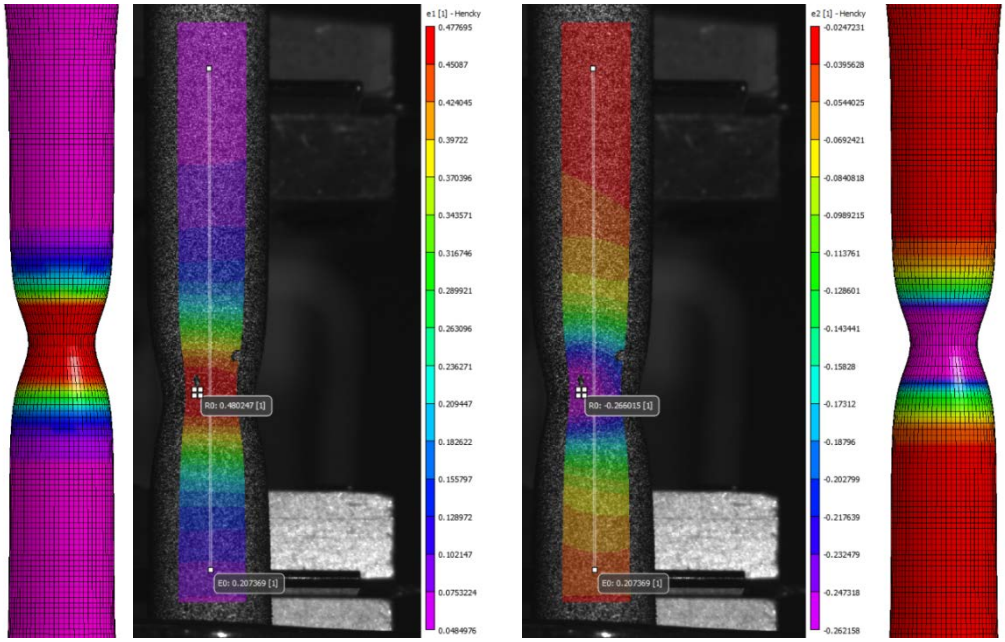

Figure 119: Diagonal, 1E-02 /s Test #21 with Test #22 Material Card Principal Strain Comparison

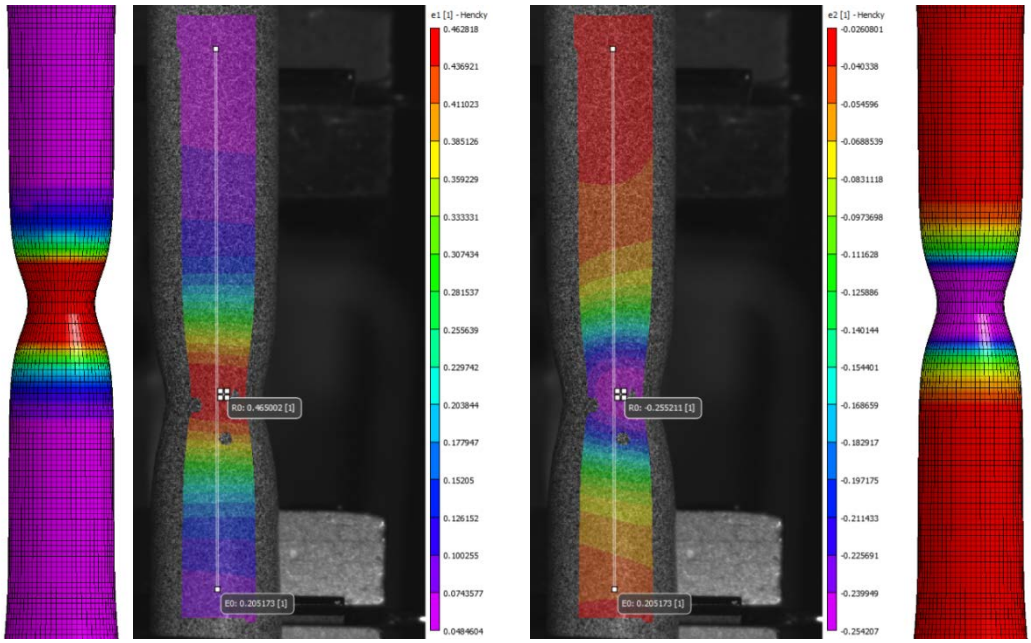

Figure 120: Diagonal, 1E-02 /s Test #23 with Test #22 Material Card Principal Strain Comparison

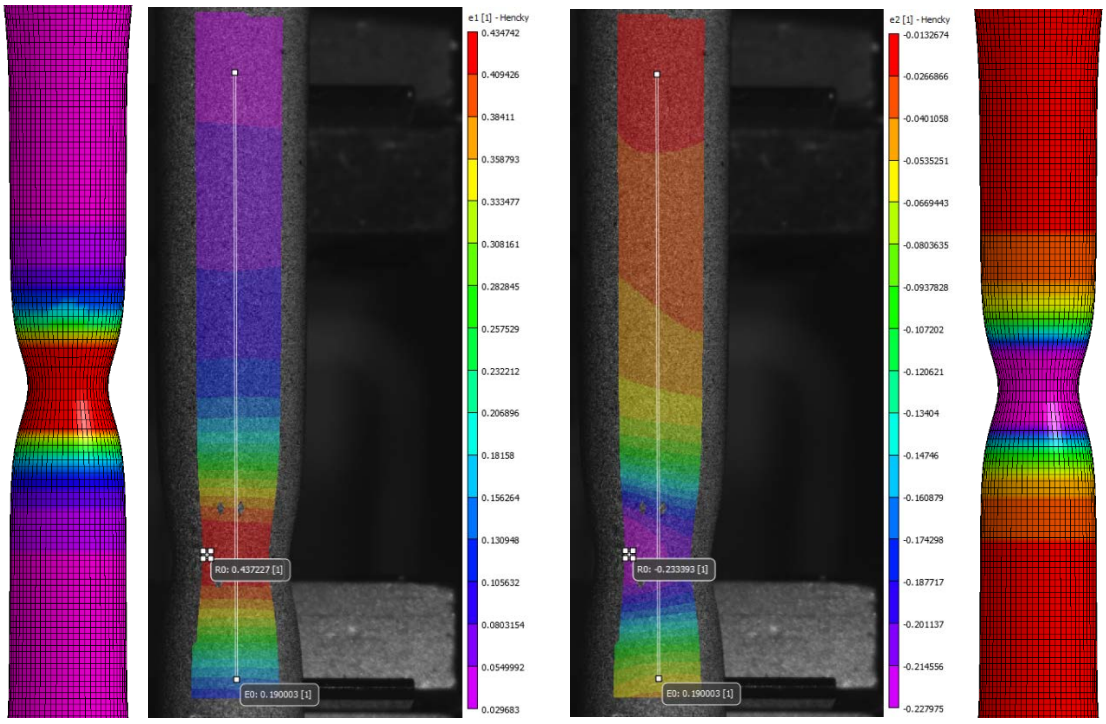

Figure 121: Diagonal, 1E-02 /s Test #24 with Test #22 Material Card Principal Strain Comparison

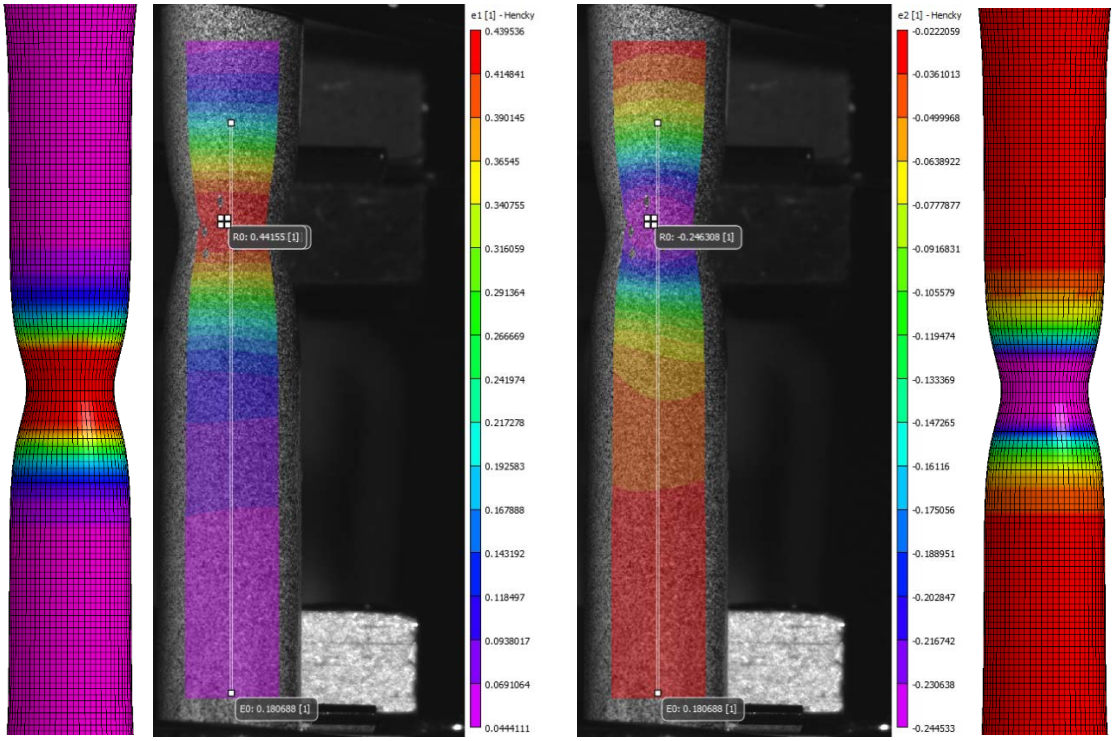

Figure 122: Diagonal, 1E-02 /s Test #25 with Test #22 Material Card Principal Strain Comparison

3.4.6 Horizontal, 1E-02 /s

3.4.6.1 Iterative Simulations for Material Card Generation

The "fan" of trial post-necking equivalent true stress-strain curves for the first of six parameter cases (horizontal, 1E-02 /s) Test #26 (Figure 69) was used as the basis for an iterative FEMU approach (Sec. 2.3.3). In our implementation, a cost function (with a specified convergence criterion or termination threshold) exploring the full (continuous) parameter range of the post-necking hardening exponent n (between perfect plasticity and upper bound) was not employed. Rather, the (discrete) trial curve from Figure 69 that produces the lowest normalized mean squared error between test and experiment was adopted as the "optimal" equivalent true stress-strain curve.

The first guess (upper bound with a post-necking hardening exponent $n = 0.0260$) simulation agrees well with the experiment until larger strains (Figure 123), where the force vs. displacement and principal strain vs. displacement results diverge.

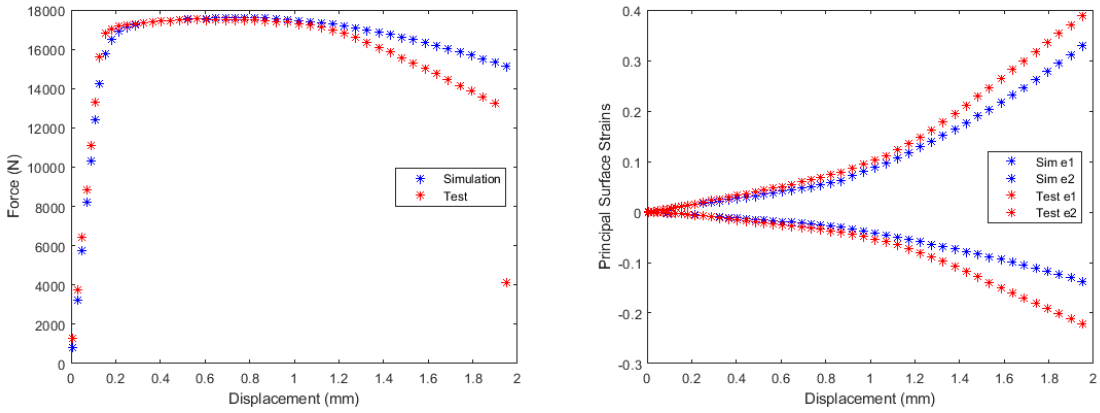

Figure 123: Horizontal, 1E-02 /s Test #26 First Guess Simulation vs. Test

In particular, the simulation over-predicts the amount of force needed to displace the material, indicating that the first guess is too stiff. Thus, a second guess (first interior curve in Figure 69 with a lower post-necking hardening exponent $n = 0.0134$) was taken from the "fan" of prospective curves. The second guess results in excellent agreement for force vs. displacement between simulation and experiment (Figure 124), with a reduction in normalized mean square error (Table 36), and the principal surface strain agreement is on the same magnitude. Therefore, the equivalent true stress-strain curve corresponding to Test #1, Guess #2 (Figure 126) was selected as our "optimal" candidate.

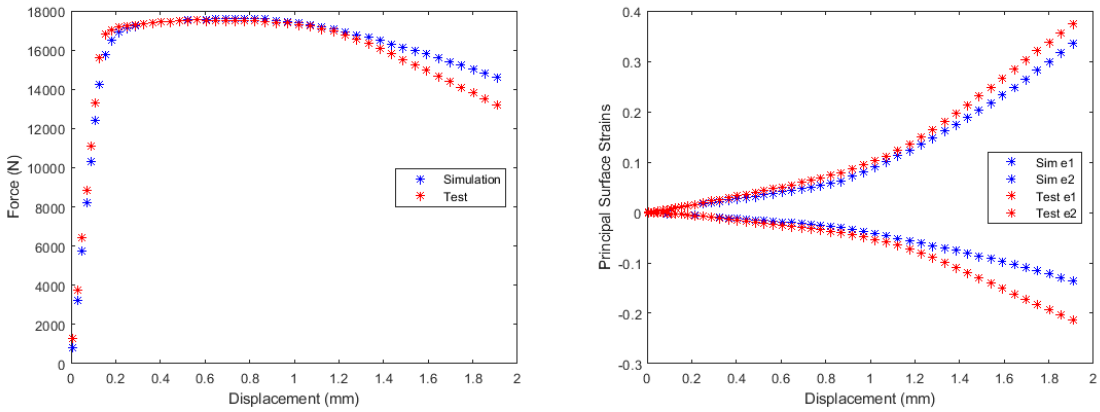

Figure 124: Horizontal, 1E-02 /s Test #26 Second Guess Simulation vs. Test

Table 36: Horizontal, 1E-02 /s Test 26 Normalized Mean Square Error Comparison

Test	Force-Displacement	e1-Displacement	e2-Displacement
Test #26 1st Guess	6.47e-06	2.46e-05	1.25e-04
Test #26 2nd Guess	7.22e-07	1.34e-05	1.16e-04

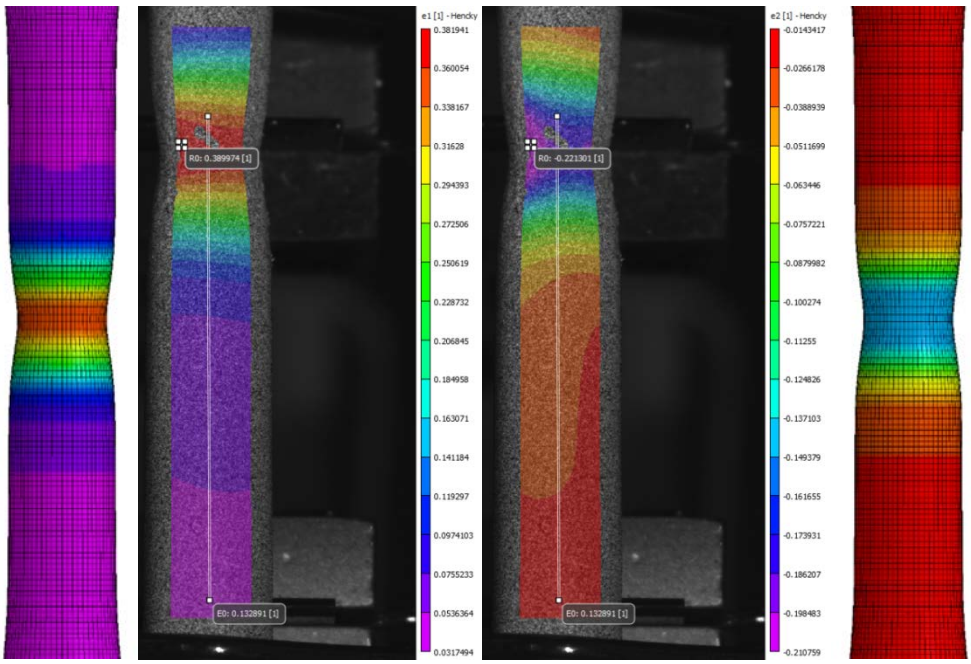

Figure 125: Horizontal, 1E-02 /s Test #26 Second Guess Principal Strain Comparison

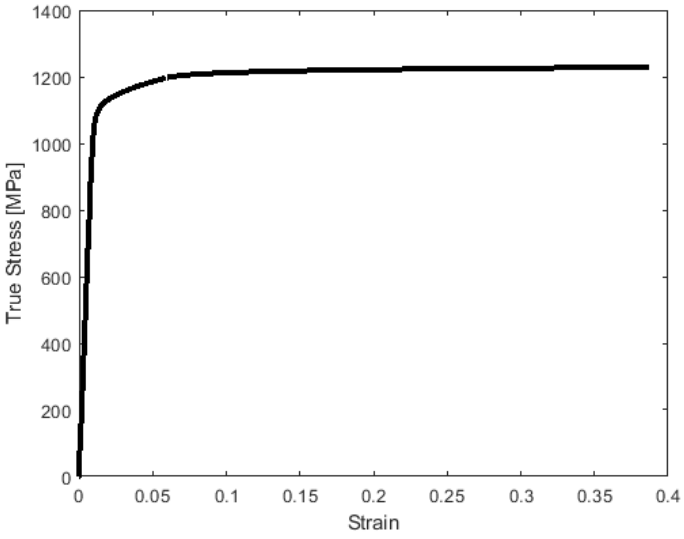

Figure 126: Horizontal, 1E-02 /s Test #26 True Stress-Strain Input Curve

3.4.6.2 Validation Simulations

Next, for validation purposes, the true stress-strain behavior from Test #26, Guess #2 was used to simulate the remaining four experiments in the horizontal, 1E-02 /s tensile test series. Good agreement is seen between simulation and experiment for Tests #27-#30 (Figure 127-Figure 130) corroborated by the error metrics in Table 37.

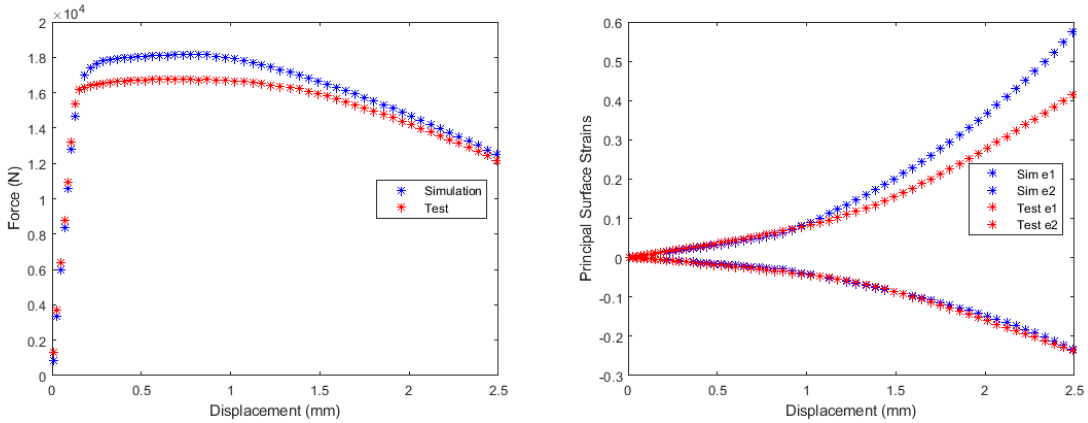

Figure 127: Horizontal, 1E-02 /s Test #27 with Test #26 Second Guess Material Card

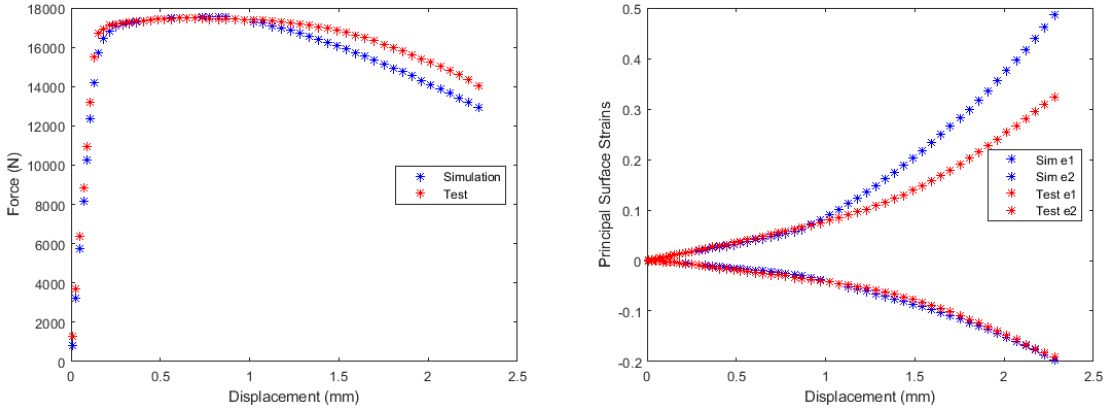

Figure 128: Horizontal, 1E-02 /s Test #28 with Test #26 Second Guess Material Card

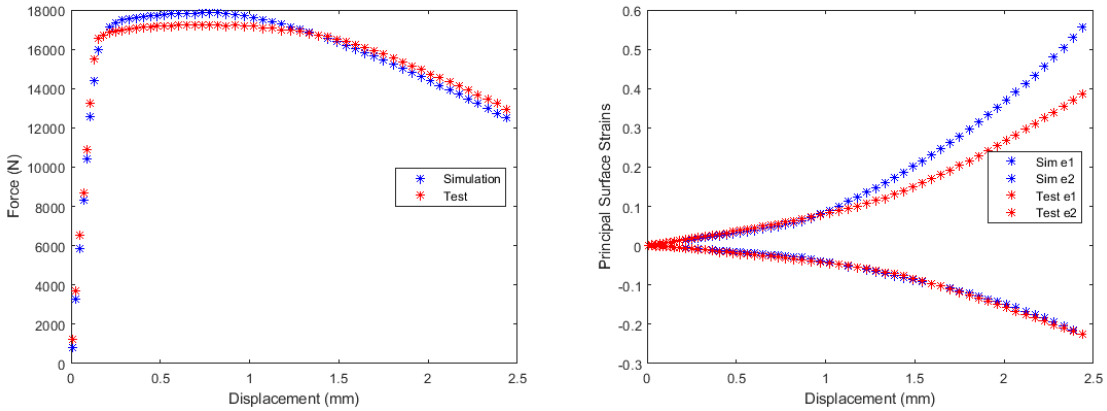

Figure 129: Horizontal, 1E-02 /s Test #29 with Test #26 Second Guess Material Card

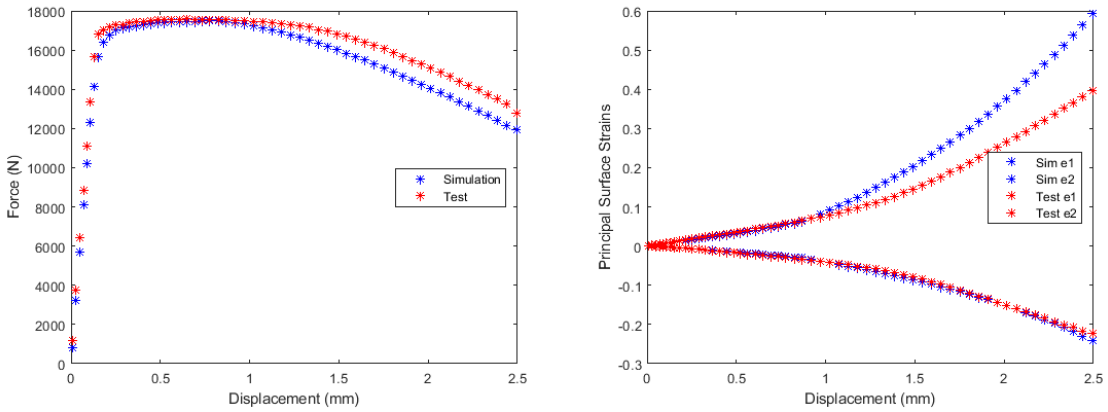

Figure 130: Horizontal, 1E-02 /s Test #30 with Test #26 Second Guess Material Card

Table 37: Horizontal, 1E-02 /s Validation Simulations Normalized Mean Square Error Comparison

	Force-Displacement	e1-Displacement	e2-Displacement
Test #27	1.24e-06	6.33e-05	1.84e-06
Test #28	6.85e-07	1.40e-04	2.36e-06
Test #29	2.97e-07	8.88e-05	1.06e-06
Test #30	6.82e-07	1.09e-04	1.63e-06

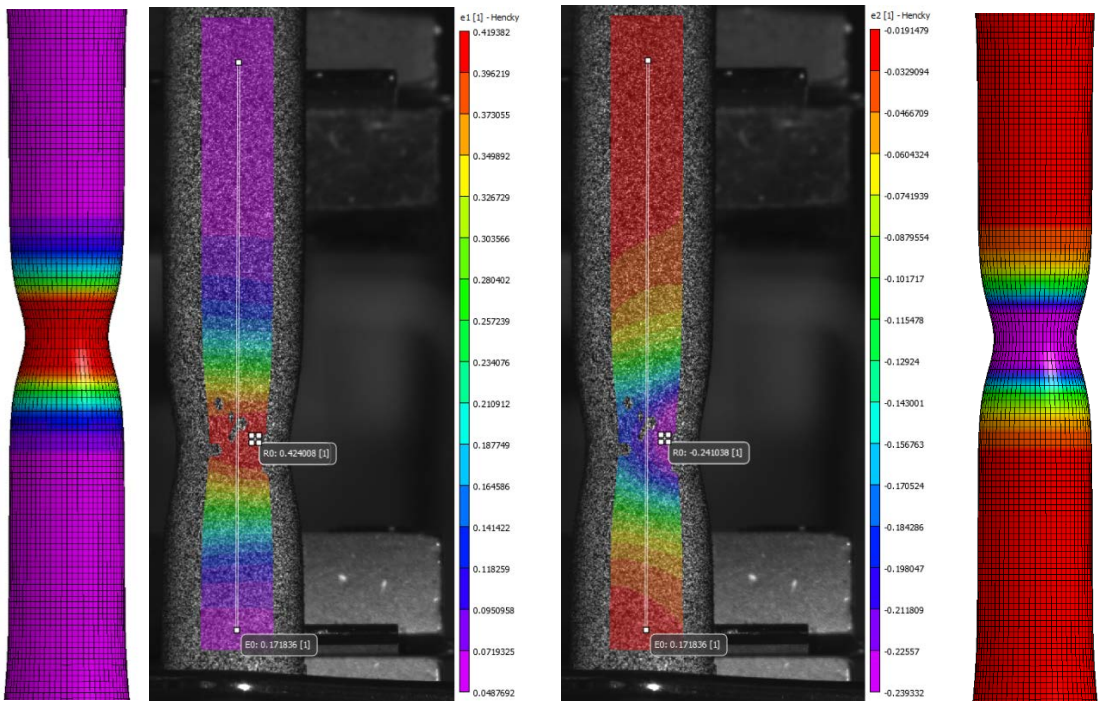

Figure 131: Horizontal, 1E-02 /s Test #27 with Test #26 Material Card Principal Strain Comparison

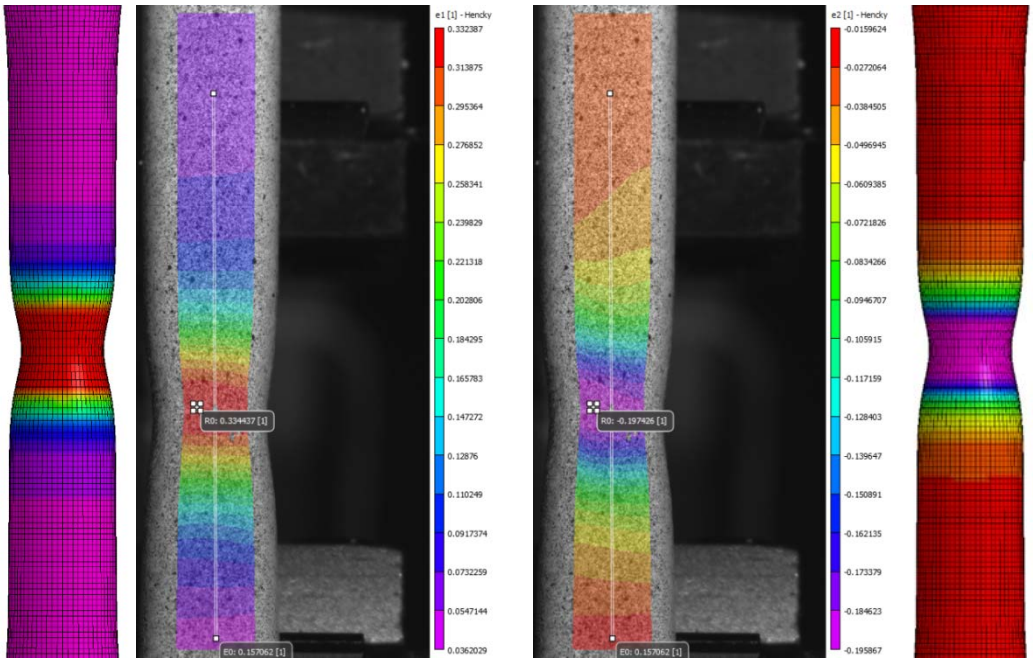

Figure 132: Horizontal, 1E-02 /s Test #28 with Test #26 Material Card Principal Strain Comparison

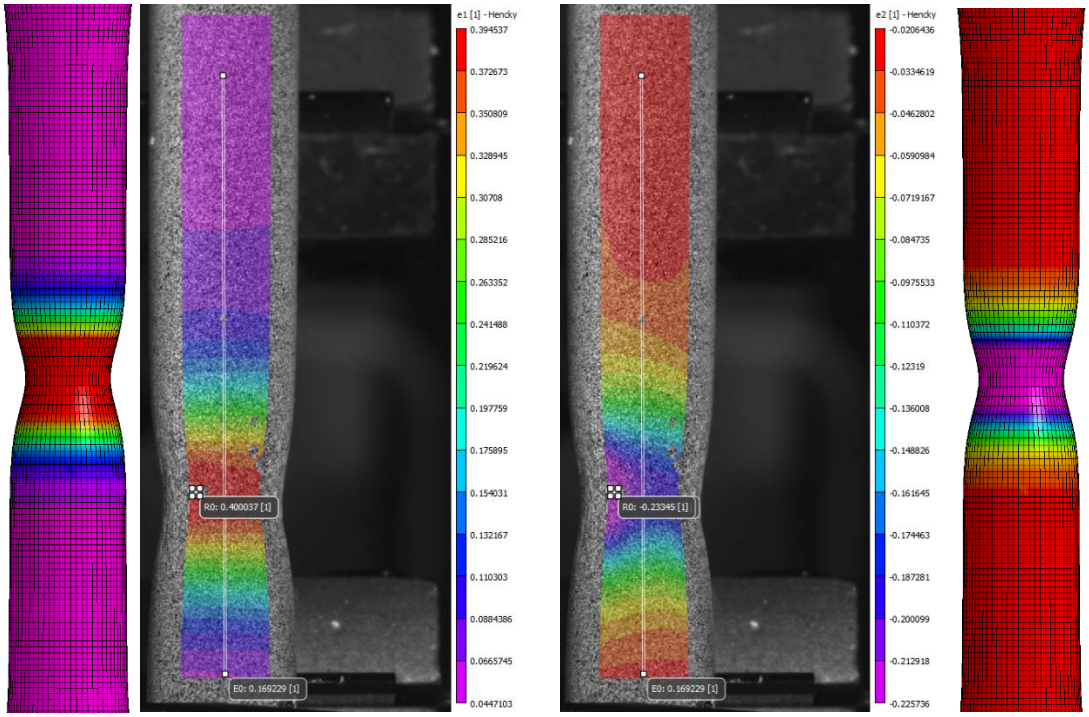

Figure 133: Horizontal, 1E-02 Test #29 with Test #26 Material Card Principal Strain Comparison

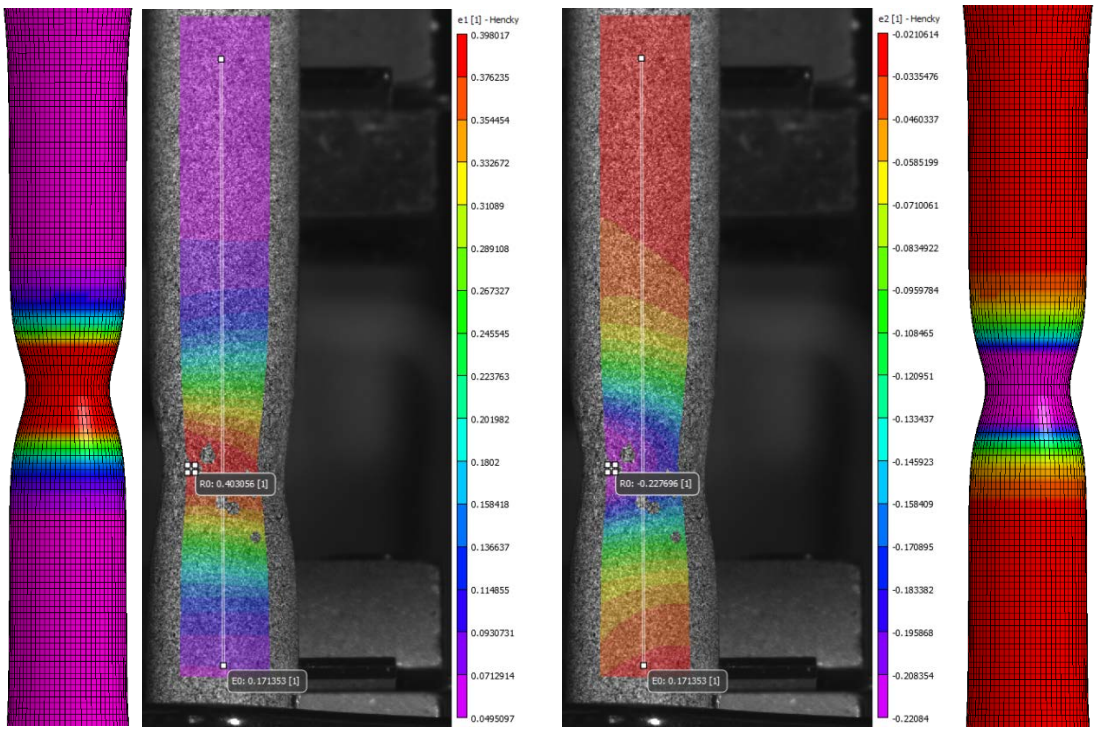

Figure 134: Horizontal, 1E-02 /s Test #30 with Test #26 Material Card Principal Strain Comparison

CHAPTER IV

DISCUSSION, CONCLUSION, AND NEXT STEPS

Perhaps the largest impact on the outcome of this project was the COVID-19 pandemic that had us out of the lab and working in a remote capacity for the greater part of a year. At the end of the day, I am very thankful for the technology that made the completion of this work possible and for everyone that was productively a part of this project when we had to play catchup. Overall, the undertaking of technical actions within the scope of the project continued to go rather smoothly throughout the duration of the project. I definitely owe much of this to the wisdom and advice found in papers, articles, and technical reports across this field of study.

With that being said, the project grinded to a halt when the AM Ti-6Al-4V specimens (spanning multiple build orientations) were delivered in one container. While we were happy to have the specimens in hand after some difficulty earlier in the project, this singular bin of specimens contained a scrambled collection of all three build orientations with no directional labeling system. With quick advice from Dr. Luke Sheridan, a routine was created to identify build orientation from grain patterns. By trimming a cross-sectional puck off of a grip section, polishing, and chemical etching the exposed area, the grain orientation could be revealed and analyzed. We quickly learned that an additional surface, orthogonal to the first cross section, would show additional differences between the three build directions. After etching the specimen and imaging under the microscope, it was evident that, together, the two cross-sectional cuts effectively captured the grain orientation, and thus correlated to three different build orientations.

The original goal of this project was a complete characterization of LPBF AM Ti-6Al-4V with an all-encompassing tabulated plasticity model containing test data assessing yield asymmetry, both quasi-static and high strain rates, and build orientation. It became clear that the planned project outline would likely be too much to complete to a high standard under the circumstances. If more time and resources were available, continued investigation into the plastic

deformation of LPBF AM Ti-6Al-4V under compression and high strain rates would be the next step. With data from these experiments, the tabulated plasticity card gains efficacy and could better predict the behavior of LPBF AM Ti-6Al-4V across a greater landscape of conditions.

Additionally, as the project approached its conclusion, computational time became hard to come by. My immediate next step would be to complete simulations of the AM Ti-6Al-4V test series using the linear interpolation post-necking correction method discussed in Section 2.3.4. This method is quicker, simpler, and effectively predicts the test with error on a similar magnitude as a typical FEMU method with manual fan iteration through a fan.

Further, it would be just as beneficial to spend time developing capability for LS-OPT, a standard optimization software inside the LS-DYNA software suite. With LS-OPT, a cost function could complete FEMU iteration over a continuous range of hardening exponents and converge to the "correct" true stress-strain input curve. While this would take additional time and computational effort (something that the linear interpolation method is able to bypass), it would be appropriate for the research community to have access to a truly converged solution of the material behavior for each test case.

Ultimately, I am very excited about the effectiveness of both of the post-necking methods discussed in the above document (FEMU and linear interpolation). However, it is noticeable that the largest amount of error lies in the comparison of the surface strains between simulation and test. Comparing the wrought metal (Inconel 625, Inconel 718, 17-4 PH stainless steel, and Ti-6Al-4V) series with the AM Ti-6Al-4V series, it is evident that earlier necking contributes to a larger amount of error in surface strain comparisons. In any regard, a short discussion on error possibilities follows.

In [44], an AM Ti-6Al-4V ductile fracture test series was completed and strains were measured using a similar stereo DIC setup on the same load frame in the same research lab. In Negri's setup, however, the stereo camera setup included the two cameras stacked vertically on top of one another. In the AM Ti-6Al-4V plasticity series in the current document, the stereo

setup included cameras on a horizontal test fixture. While both setups would have been calibrated and focused on the gage section of the specimens, the cameras view the 3-dimensional specimens as a 2-dimensional plane. The test series above seems to have additional error specifically in the longitudinal direction (E1) perpendicular to the transverse DIC direction. In [44], there is additional error specific to the transverse direction (E2) perpendicular to the longitudinal DIC direction.

Further, the imaging of data with DIC relies on a calibration and focusing of the camera on a certain portion of the test specimen. Once the test is completed, a VE and VSG are placed inside a correlated window of the gage section. If failure occurred towards the edge or outside of the camera's focal point, the data gathered by the eventually placed VSG could lose its trustworthiness as the specimen displaces, localizes, and necks. Perhaps, these thoughts could explain that a portion of the error can be found in the DIC imaging of the mechanical tests. But, if only the force-displacement matches between simulation and test, is that good enough to assume the input true stress-strain curve accurately captures the material behavior observed in the test?

Also, one has to consider mesh effects. If a cross section (Figure 135) is taken out of the middle of the gage section towards the end of simulation, contour differences can be seen between the core of the cross section and the surface.

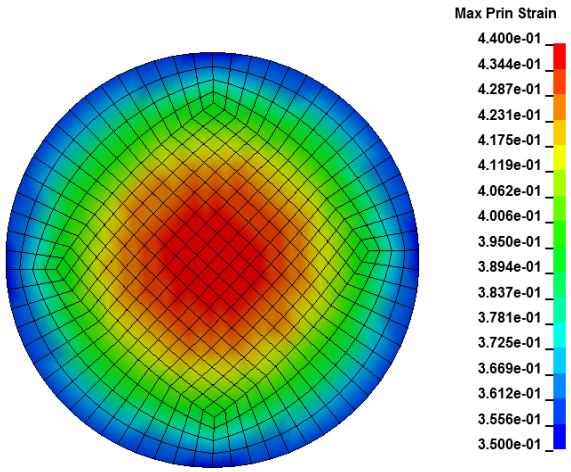

Figure 135: Cross Sectional Cut of AM Ti-6Al-4V Mesh at Final Frame of Simulation

Mesh effects have an additional argument when comparing principal strain vs. displacement plots at both a surface and an internal element. For an axisymmetric cylindrical specimen, E1 (the maximum principal strain), should be very large, while E2 and E3 should be equal and very small. In the test, imaging and data gathering is not perfect; thus, E2 does not equal E3. However, on the surface of the mesh in the simulation, this is also the case. Only when an element in the very middle of the cross section is plotted, do E2 and E3 match as it should in a theoretically ideal axisymmetric simulation. As you move away from the most central element, this discrepancy grows.

Following the above discussion, a consideration of the materials anisotropy is warranted. It is well known that AM Ti-6Al-4V displays slight anisotropy based on the build direction. This has merit considering the discrepancy appears after the onset of necking, where the stress state loses its uniaxial property. In the tensile test experiments, the two lesser principal strains are not equal; which argues against axisymmetric behavior. This is a large indicator of anisotropy in a material and is a likely cause for the small difference between E2 and E3 as the specimen is strained in the test.

REFERENCES

[1] Callister Jr., William D., Materials Science and Engineering an Introduction. (6th Edition) New York, NY: John Wiley and Sons, Inc., 2003.

[2] LS-DYNA. v. SMP d R10.1.0, LSTC, Livermore, CA. 2017.

[3] Johnson, Gordon R. and Cook, William H. “Fracture Characteristics of three metals subjected to various strains, strain rate, temperatures and pressures.” Engineering Fracture Mechanics, Vol. 21, Issue 1, 31-48. 1985.

[4] Gambirasio, Luca and Rizzi, Egidio. “On the calibration strategies of the Johnson–Cook strength model: Discussion and applications to experimental data,” Materials Science and Engineering: A, Vol. 610, 370-413, 2014.

[5] Dixit, U.S., Joshi, S.N., and Davim, J.P. “Incorporation of material behavior in modeling of metal forming and machining processes: A review.” Machine & Design, Vol. 32, Issue 7, 3655-3670. 2011.

[6] Jung-Ho, Cheng and Noboru, Kikuchi. “An analysis of metal forming processes using large deformation elastic-plastic formulations.” Computer Methods in Applied Mechanics and Engineering, Vol. 49, Issue 1, 71-108. 1985.

[7] Smerd, R., et al., “High strain rate tensile testing of automotive aluminum alloy sheet.” International Journal of Impact Engineering, Vol. 32, Issues 1–4, 541-560, 2005.

[8] Dietenberger, Michael, Buyuk, Murat, and Kan, Cing-Dao (Steve). “Development of a High Strain Rate Dependent Vehicle Model.” LS-DYNA Anwenderforum, Bamberg, Germany. 2005.

[9] Carney, K.S., Pereira, J.M., Revilock, D.M., and Matheny, P. “Jet engine fan blade containment using an alternate geometry.” International Journal of Impact Engineering, Vol. 36, Issue 5, Pages 720-728. 2009.

[10] DeMange, Jeffrey J., Prakash, Vikas, and Pereira, J. Michael. “Effects of material microstructure on blunt projectile penetration of a nickel-based super alloy.” International Journal of Impact Engineering, Vol. 36, Issue 8, 1027-1043. 2009

[11] Stamper, E. and Hale, S. “The Use of LS-DYNA Models to Predict Containment of Disk Burst Fragments.” 10th International LS-DYNA Users Conference, Impact Analysis. 2008.

[12] NTSB. Left Engine Failure and Subsequent Depressurization, Southwest Airlines Flight 1380, Boeing 737-7H4, N772SW, Philadelphia, Pennsylvania, April 17, 2018. Aircraft Accident Report AAR-19/03. November 2019.

[13] Dungey, C. and Bowen, P., “The effect of combined cycle fatigue upon the fatigue performance of TI–6AL–4V fan blade material.” Journal of Materials Processing Technology, Vol. 153–154, 374-379. 2004.

[14] FAA. “Parts Manufacturer Approval (PMA).” FAA.gov. United States Department of Transportation. Last Modified on April 15, 2011. Accessed on June 8, 2021.

[15] Bikas, H., Stravropooulos, P., and Chryssolouris, G. “Additive manufacturing methods and modelling approaches: a critical review.” International Journal of Advanced Manufacturing Technology, Vol. 83, 389-405. 2016.

[16] Caffrey, T., Wohlers, T., & Campbell, I. “Executive summary of the Wohlers Report.” 2016.

[17] Wong, K.V. and Hernandez, A. “A review of Additive Manufacturing.” International Scholarly Research Notices. Vol, 2012, 10 pages. 2012.

[18] Bourell, D., et al. “Materials for additive manufacturing.” CIRP Annals, Vol. 66 Issue 2, 659-681. 2017.

[19] Herzog, D., Seyda, V., Wycisk, E., and Emmelmann, C. “Additive manufacturing of metals.” Acta Materialia, Vol. 117, 371-392. 2016.

[20] Thijs, L., et al. “A study of the microstructural evolution during selective laser melting of Ti-6Al-4V.” Acta Materialia, Vol 58, Issue 9, 3303-3312. May 2010.

[21] Arisoy, Y.M., et al. “Influence of scan strategy and process parameters on microstructure and its optimization in additively manufactured nickel alloy 625 via laser powder bed fusion.” The international Journal of Advanced Manufacturing Technology, Vol 90, 1393-1417. 2017.

[22] Salandari-Rabori, A., Wang, P., Dong, Q., and Fallah, V. “Enhancing as-built microstructural integrity and tensile properties in laser powder bed fusion of AlSi10Mg alloy using a comprehensive parameter optimization procedure.” Materials Science and Engineering: A, Vol. 805, 140620. February 2021.

[23] Letenneur, M., Kreitcberg, A., Brailovski, V. “Optimization of Laser Powder Bed Fusion Processing Using a Combination of Melt Pool Modeling and Design of Experiment Approaches: Density Control.” Journal of Manufacturing and Materials Processing, Vol 3(1), 21. 2019

[24] Debroy, T., et al. “Additive manufacturing of metallic components – Process, structure and properties.” Progress in Materials Science, Vol 92, 112-224. March 2018.

[25] ASTM F2924-14. "Standard Specification for Additive Manufacturing Titanium-6Aluminum-4Vanadium with Powder Bed Fusion." ASTM International, West Conshohocken, PA. 2014.

[26] Beese, A.M, Carroll, B.E. “Review of Mechanical Properties of Ti-6Al-4V Made by Laser-Based Additive Manufacturing Using Powder Feedstock.” JOM Vol. 68:3, 724-734. 2016.

[27] Vilaro, T., Colin, C., and Bartout, J.D. “As-fabricated and heat-treated microstructures of the Ti-6Al-4V alloy processed by selective laser melting.” Metallurgical and materials transactions A, 42(10), 3190-3199. 2011.

[28] Lütjering, G. and Williams, J.C. “Titanium.” Springer Science & Business Media, Second Edition. 2007.

[29] Gorji, M.b., Tancogne-Dejean, T., and Mohr, D. “Heterogeneous random medium plasticity and fracture model of additively-manufactured Ti-6Al-4V.” Acta Materialia, Vol. 148, 442-455. April 2018.

[30] Wilson-Heid, A.E., Qin, S., and Beese, A.M. “Anisotropic multiaxial plasticity model for laser powder bed fusion additively manufactured Ti-6Al-4V.” Materials Science and Engineering: A, Vol 738, 90-97. December 2018.

[31] Bridgman, P. W., “Studies in Large Plastic Flow and Fracture.” Harvard University Press. 2nd Printing. 2013.

[32] La Rosa, G., Risitano, A., & Mirone, G. “Postnecking elastoplastic characterization: degree of approximation in the Bridgman method and properties of the flow-stress/true-stress ratio.” Metallurgical and Materials Transactions A, Vol. 34(A), 615-624. 2003.

[33] Yu, J.H., McWilliams, B.A., and Kaste, R.P. “Digital Image Correlation Analysis and Numerical Simulation of Aluminum Alloys under Quasi-static Tension after Necking Using the Bridgman’s Correction Method.” Experimental Techniques Vol. 40, 1359-1367. 2016.

[34] Grédiac, Michel, Pierron, Fabrice. “Applying the Virtual Fields Method to the identification of elasto-plastic constitutive parameters.” International Journal of Plasticity, Vol. 22, Issue 4, 602-627. 2006.

[35] Kim, J. H., Serpantie, A., Barlat, F., Pierron, F., Lee, M. G. Characterization of the post-necking strain hardening behavior using the virtual fields method.” International Journal of Solids and Structures, Vol. 50, 3829-3842. 2013.

[36] Marth, Stefan, Häggblad, Hans-Åke, Oldenburg, Mats, Östlund, Rickard. “Post necking characterisation for sheet metal materials using full field measurement.” Journal of Materials Processing Technology, Vol. 238, 315-324. 2016.

[37] Kajberg, J., Lindkvist, G. “Characterisation of materials subjected to large strains by inverse modelling based on in-plane displacement fields.” International Journal of Solids and Structures, Vol. 41, 3439-3459. 2004.

[38] Fernandes, J.V., Rodrigues, D.M., Menezes, L.F., and Vieira, M.F. “A modified swift law for prestrained materials.” International Journal of Plasticity, Vol 14, Issue 6 537-550. 1998.

[39] Guery, Adrien, Hild, François, Latourte, Félix, Roux, Stéphane. “Identification of crystal plasticity parameters using DIC measurements and weighted FEMU.” Mechanics of Materials, Vol 100, 55-71. 2016.

[40] Mathieu, F., Leclerc, H., Roux, S., “Estimation of Elastoplastic Parameters via Weighted FEMU and Integrated-DIC.” Experimental Mechanics, Vol 55, 105-119. 2015.

[41] Zhang, K. S., Li, Z. H., “Numerical analysis of the stress-strain curve and fracture initiation for ductile material.” Engineering Fracture Mechanics, Vol 49, Issue 2, 235-241. 1994.

[42] ASTM E606. " Standard Test Method for Strain-Controlled Fatigue Testing." ASTM International, West Conshohocken, PA. 2019.

[43] Haight, S., Wang L., Du Bois, P., Carney, K., Kan, C-D. “Development of Titanium Alloy Ti- 6Al-4V. U.S. Department of Transportation Federal Aviation Administration Air Traffic Organization Operations Planning Office of Aviation Research and Development, DOT/FAA/TC- 15/23, May 2016.’

[44] C.A. Negri, "Ductile Fracture of Laser Powder Bed Fusion Additively Manufactured Ti-6Al-4V," MS Thesis, University of Dayton, 2021.